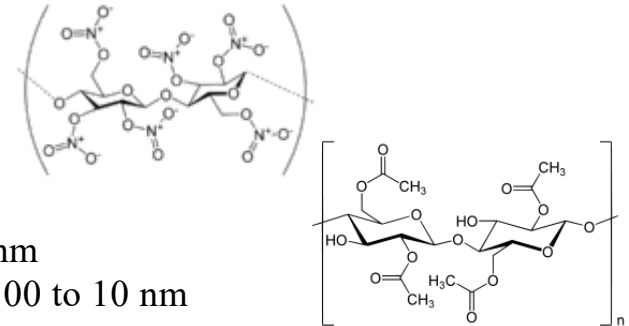


Polymer Membranes



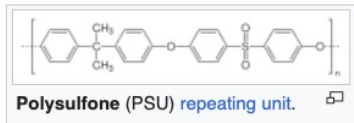
Microfiltration: filtering particles in the range of 10 μm to 100 μm

Ultrafiltration: filtering particles and molecules in the range of 100 to 10 nm

Porous Membranes

Derivatized cellulose: Nitrocellulose or cellulose acetate

Chemical and thermal stability polysulfones, polyacrylonitrile, or poly(vinylidene fluoride)



Dense Membranes

Desalination of seawater by reverse osmosis and separation of gases

oxygen enrichment in air,

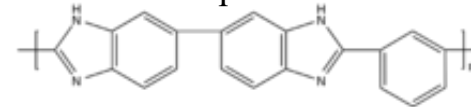
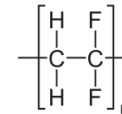
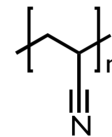
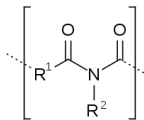
purification of natural gas,

separation of carbon dioxide or hydrogen from various gas streams

Separation of olefins from paraffins (cryogenic separation by distillation of ethylene from ethane)

Separation of biomacromolecules, such as mixtures of similar-sized proteins

polyimides, polybenzimidazoles, and polysulfones



Problems with porous membranes: fouling and scaling aging (densification with time), or compaction (densification caused by large transmembrane pressure)

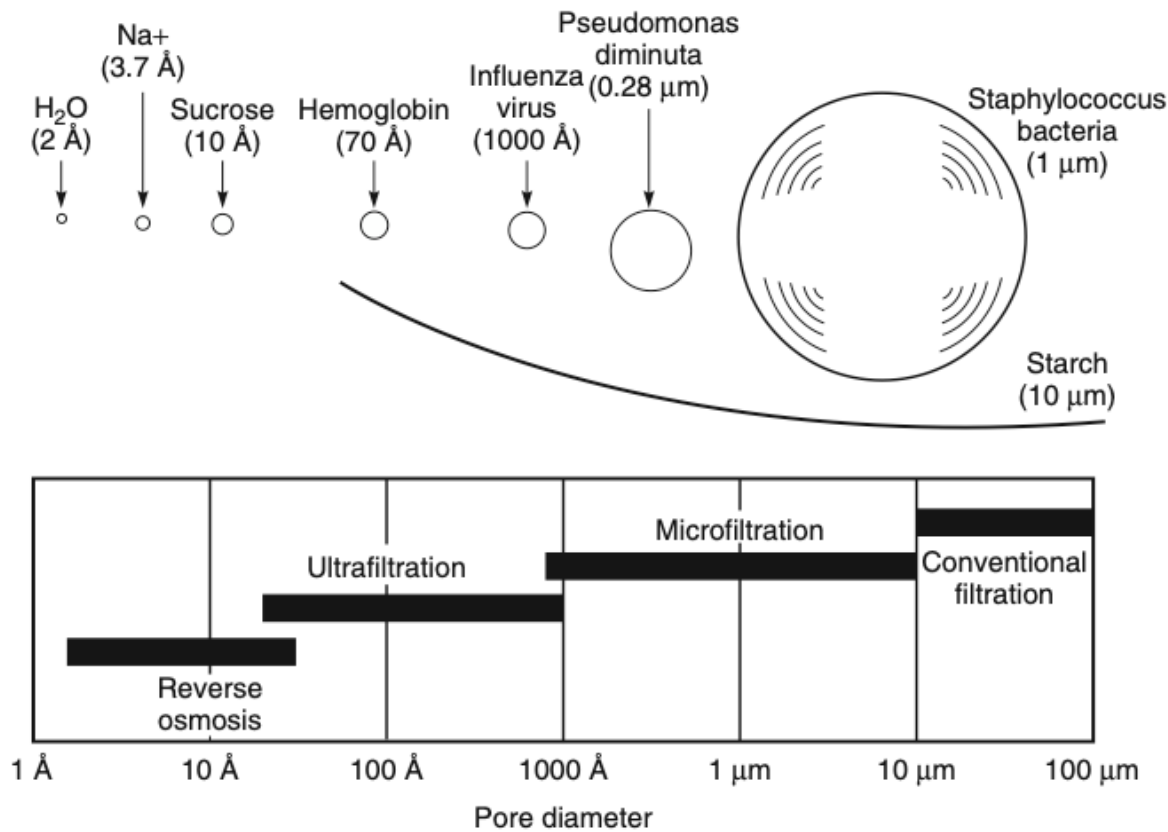


Figure 1.3 Reverse osmosis, ultrafiltration, microfiltration, and conventional filtration are related processes differing principally in the average pore diameter of the membrane filter. Reverse osmosis membranes are so dense that discrete pores do not exist; transport occurs via statistically distributed free volume areas. The relative size of different solutes removed by each class of membrane is illustrated in this schematic

Polymer Membranes

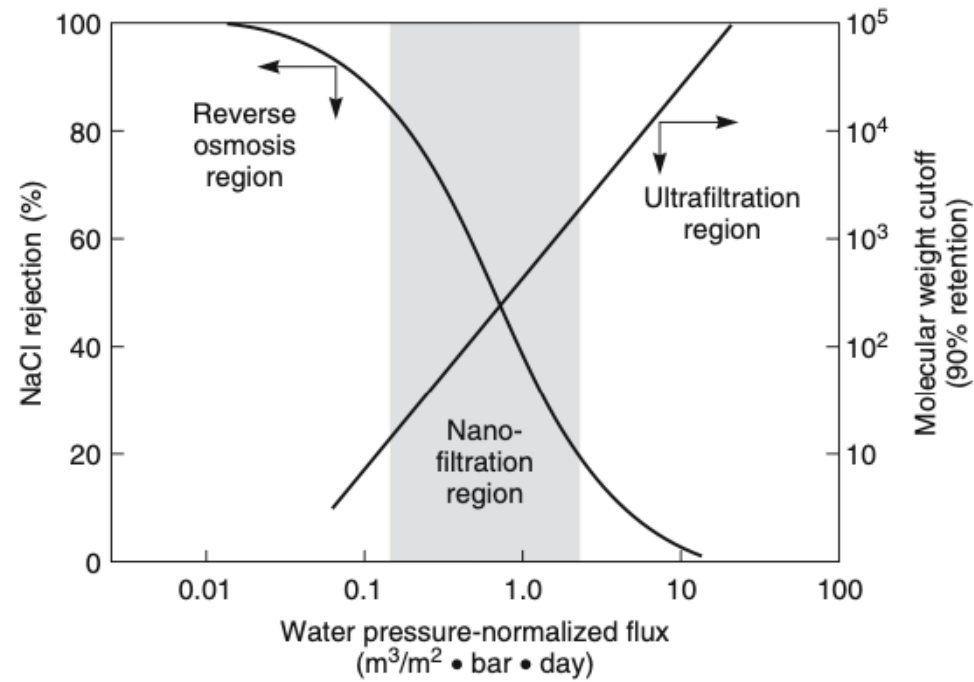
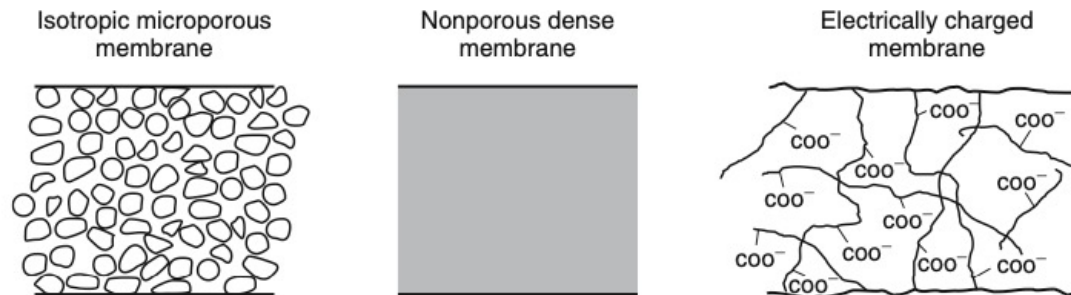


Figure 2.47 Diagram of the region of nanofiltration membrane performance relative to reverse osmosis and ultrafiltration membranes [81]

Polymer Membranes

Symmetrical Membranes



Anisotropic Membranes

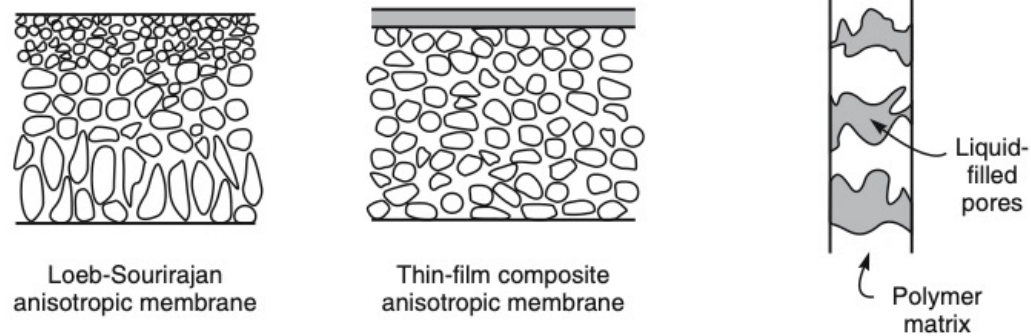


Figure 1.2 Schematic diagrams of the principal types of membranes

Gas Separation Polymer Membranes

Membrane Flux

$$Q_a = P_a A \Delta p_a / l$$

Q_a steady-state flux

P_a permeability coefficient for gas "a"

$$P_a = S_a D_a$$

S_a Solubility Coefficient (at high pressure and/or concentration interface)

D_a Diffusion Coefficient

(desorption at low pressure and/or concentration interface)

A surface area

Δp_a differential partial pressure

l membrane thickness

Assumption of Fickian diffusion of dissolved gas

Isotropic dense polymer membrane

Membrane Selectivity

$$\alpha_b^a = \frac{P_a}{P_b}$$

Goal: high flux of gas "a" with low flux of gas "b"

Gas Separation Polymer Membranes

Membrane Flux

$$Q_a = P_a A \Delta p_a / l$$

Membrane Selectivity

$$\alpha_b^a = \frac{P_a}{P_b}$$

Table 1. Hydrogen permeabilities and H₂/N₂ selectivities for various classes of polymers. See (4) for detailed values. The values given here are approximate and are intended to reflect general trends. Significant variations within classes can be found, and exceptions to the general trends exist.

Polymer	$P_{H_2} (\times 10^9 \text{ cm}^3 \text{ STP} / \text{cm}^2 \text{-sec-cmHg})$	$\alpha_{N_2}^{H_2}$
Silicone rubbers	100 to 500	1.5 to 3.0
Hydrocarbon rubbers	50 to 300	2.0 to 4.0
Polyphenylene oxides	50 to 100	10 to 20
Substituted polysulfones	20 to 70	15 to 25
Polycarbonates, polysulfones	0.5 to 20	25 to 75
Polyesters, nylons	0.5 to 3.0	50 to 150
Acrylonitrile copolymers (high concentration acrylonitrile)	0.1 to 1.0	100 to > 1000

Gas Separation Polymer Membranes

Membrane Flux

$$Q_a = P_a A \Delta p_a / l$$

Membrane Selectivity

$$\alpha_b^a = \frac{P_a}{P_b}$$

There are engineering limits to increasing A and Δp_a

Technical solutions involve reduction of l to $\ll 1 \mu\text{m}$ for high α_b^a materials

Gas Separation Polymer Membranes

Membrane Flux

$$Q_a = P_a A \Delta p_a / l$$

Membrane Selectivity

$$\alpha_b^a = \frac{P_a}{P_b}$$

Technical solutions involve reduction of l to $\ll 1 \mu\text{m}$ for high α_b^a materials

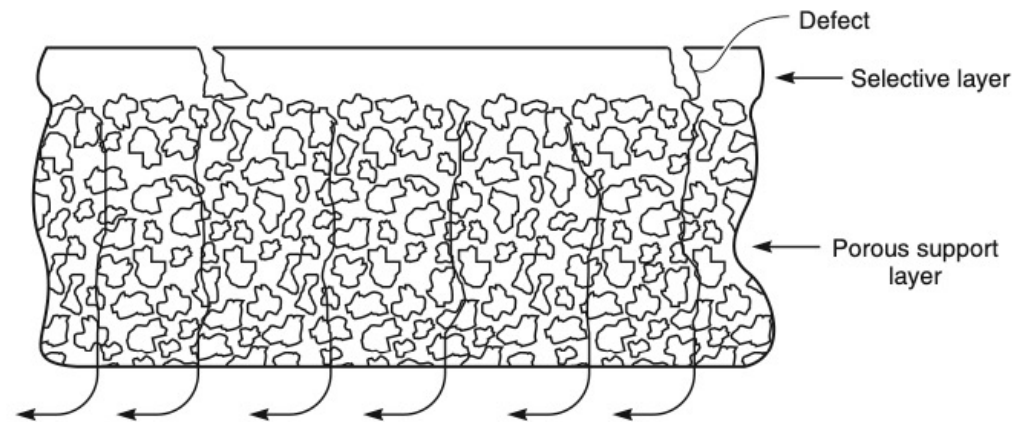
Porosity of separation layer can be solved in Resistance Model (RM) Membranes

High flux non-selective coating (PDMS)

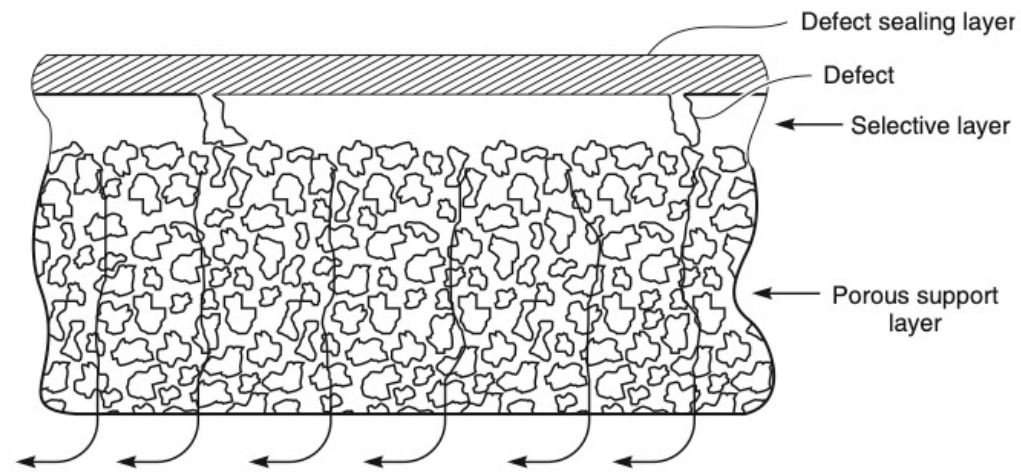
Dense Separation layer (acrylonitrile copolymer)

Porous support layer (polysulfone)

Coating layer is thicker in pores and can have lower transport than separation layer



(a) Defective Loeb-Sourirajan anisotropic membrane



(b) Henis and Tripodi silicone rubber-coated membrane

Figure 3.31 Schematic of (a) Loeb–Sourirajan and (b) Henis and Tripodi gas separation membranes [77]

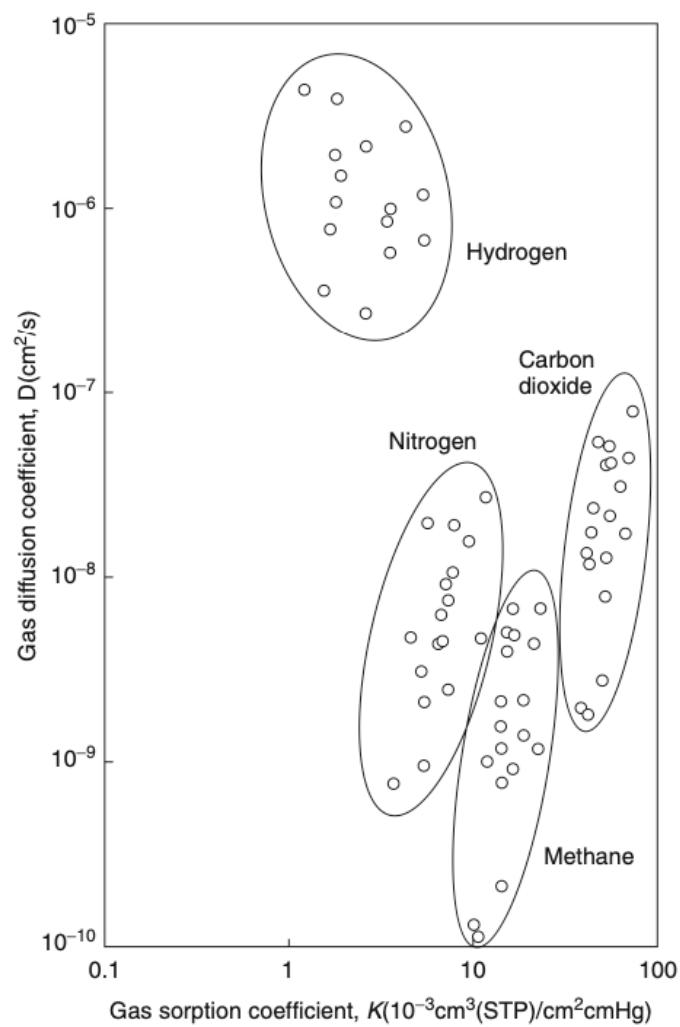


Figure 2.20 Diffusion and sorption coefficients plotted for gases in a family of 18 related polyimides. (Data of Tanaka et al. [29].)

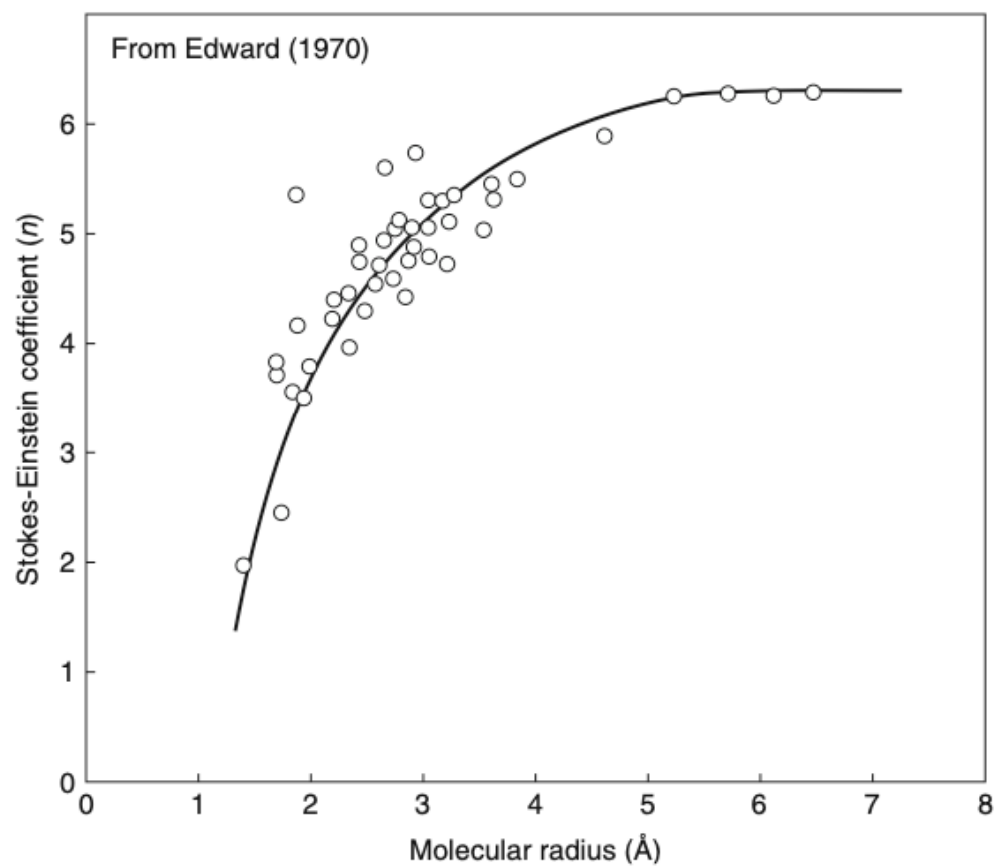


Figure 2.21 Value of the coefficient n in the Stokes-Einstein equation (Equation 2.98) required to achieve agreement between calculation and experimental solute diffusion coefficients in water. Reprinted with permission from [35]. Copyright (1970) American Chemical Society.

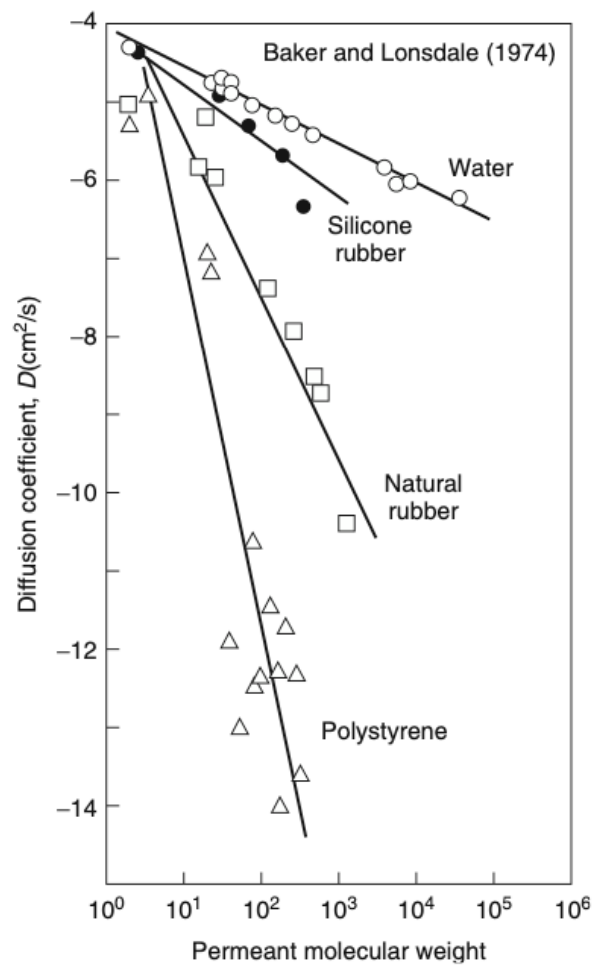


Figure 2.22 Permeant diffusion coefficient as a function of permeant molecular weight in water, natural rubber, silicone rubber, and polystyrene. Diffusion coefficients of solutes in polymers usually lie between the value in silicone rubber, an extremely permeable polymer, and the value in polystyrene, an extremely impermeable material [36]

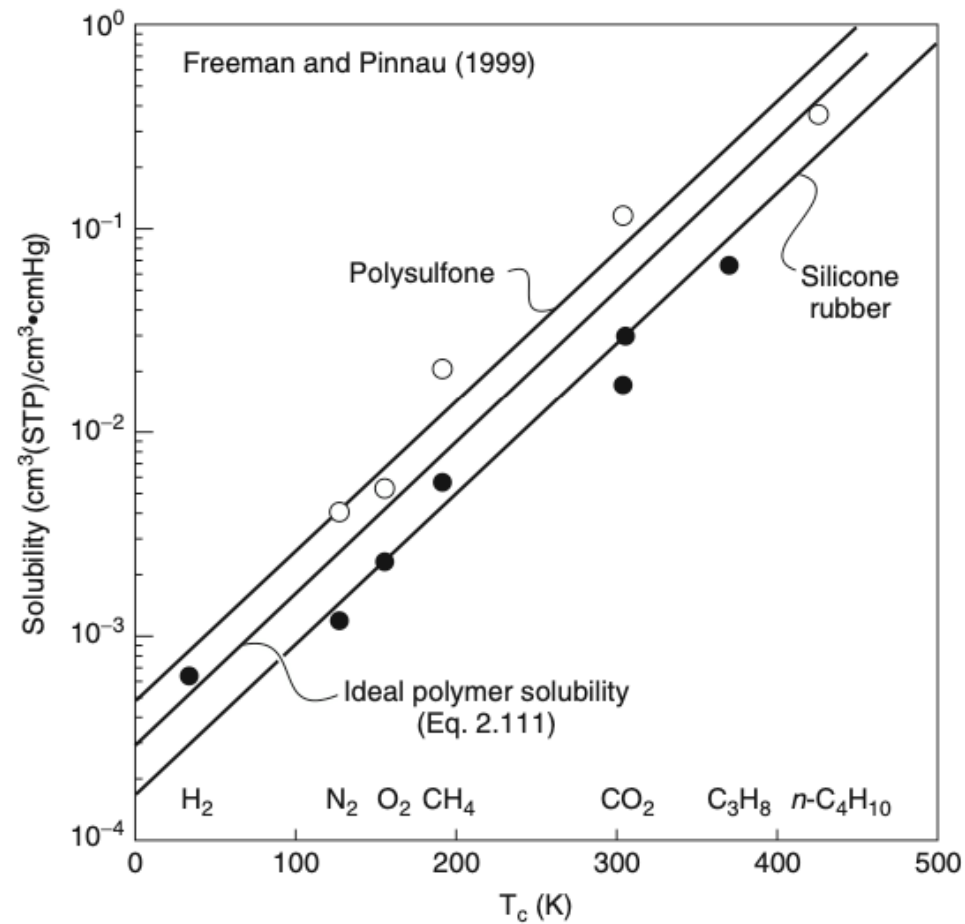


Figure 2.29 Solubilities as a function of critical temperature (T_c) for a typical glassy polymer (polysulfone) and a typical rubbery polymer (silicone rubber) compared with values for the ideal solubility calculated from Equation 2.111 [53]

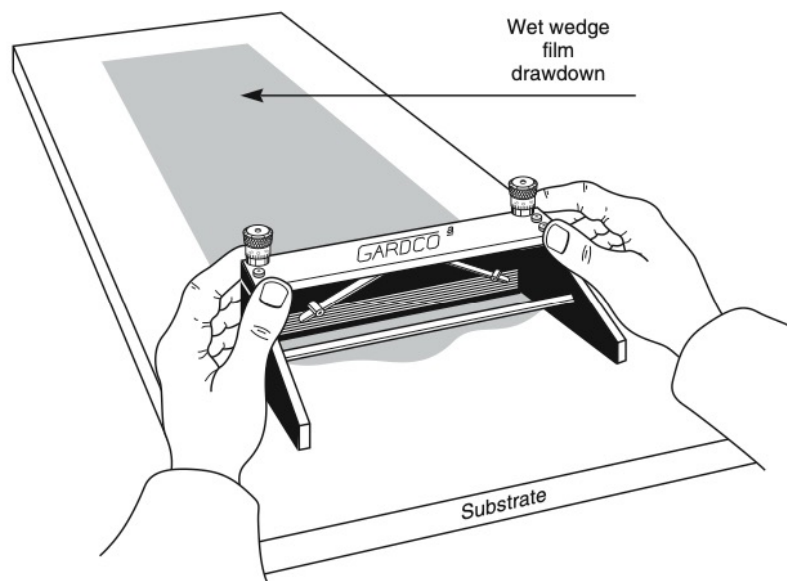


Figure 3.1 A typical hand-casting knife. (Courtesy of Paul N. Gardner Company, Inc., Pompano Beach, FL.)

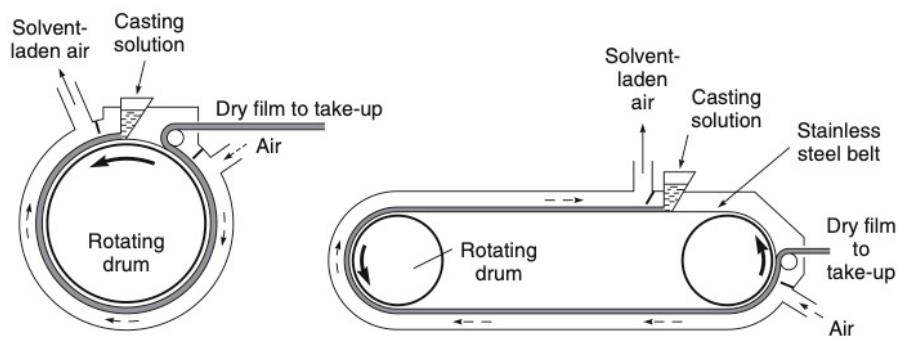
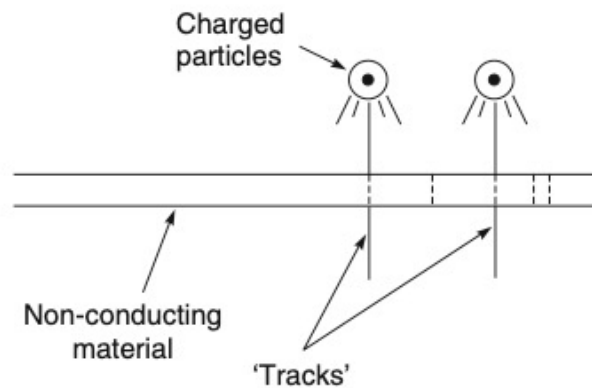


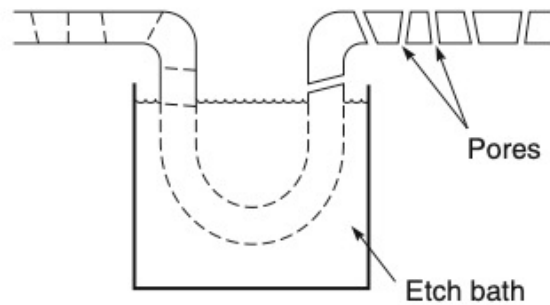
Figure 3.2 Machinery used to make solution-cast film on a commercial scale



Figure 3.3 A typical laboratory press used to form melt-pressed membranes. (Courtesy of Carver, Inc., Wabash, IN.)



Step 1: Polycarbonate film is exposed to charged particles in a nuclear reactor



Step 2: The tracks left by the particles are preferentially etched into uniform, cylindrical pores

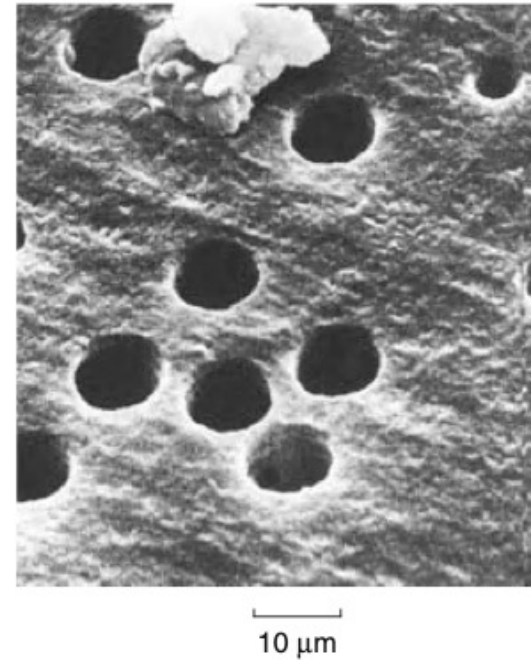


Figure 3.4 Diagram of the two-step process to manufacture nucleation track membranes [4] and photograph of resulting structure. Reprinted with permission from Whatman Ltd. Copyright (2012) Whatman Ltd, part of GE Healthcare.

Microfiltration

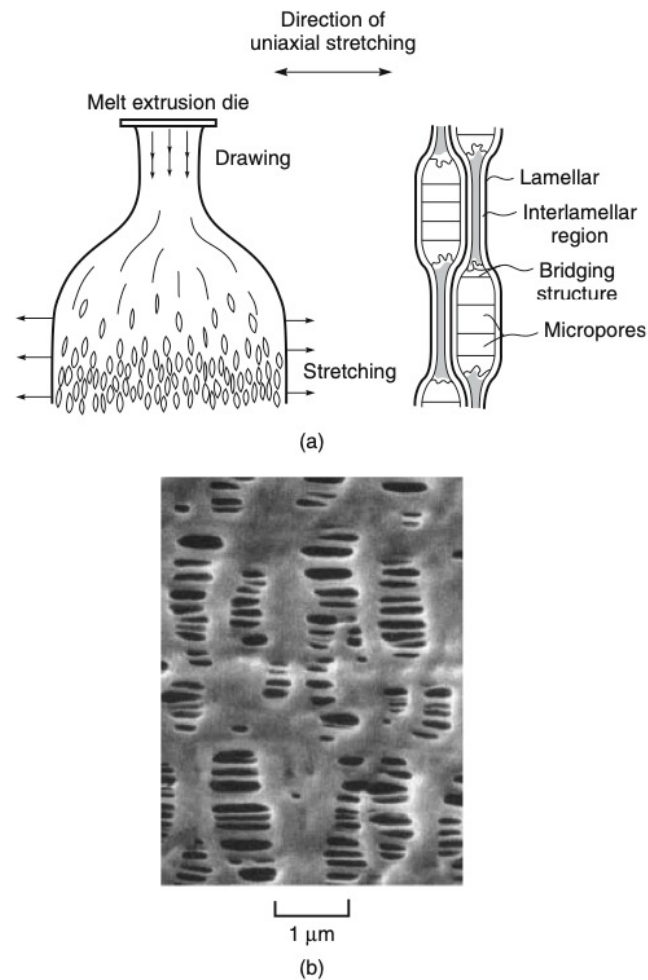


Figure 3.5 (a) Preparation method of a typical expanded polypropylene film membrane, in this case Celgard[®]. (b) Scanning electron micrograph of the microdefects formed on uniaxial stretching of films. Reprinted with permission from [6]. Copyright (1974) American Chemical Society.

Vapor barrier in construction, separator membrane in Li⁺ batteries, biological filtration membrane

Microfiltration

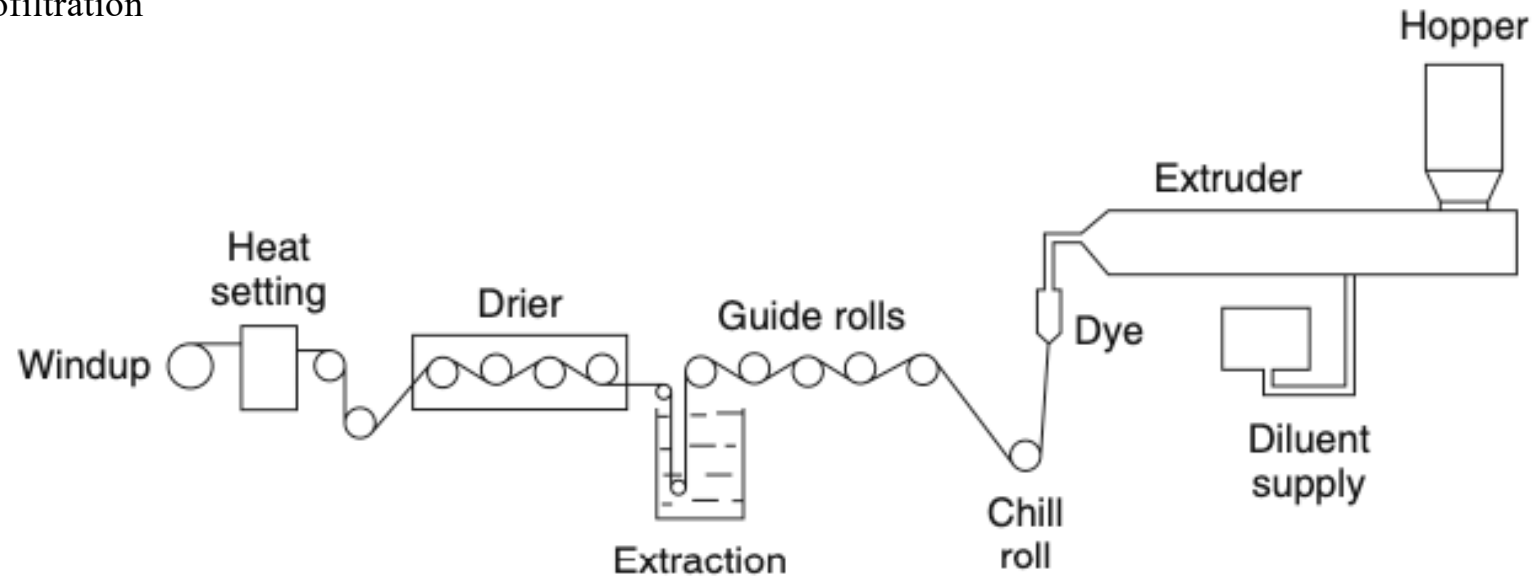


Figure 3.6 Flow schematic of a melt extruder system used to make polypropylene membranes by template leaching [14]

Vapor barrier in construction, separator membrane in Li⁺ batteries,
biological filtration membrane

Anisotropic Membrane Preparation Methods

- **Phase separation membranes:** This category includes membranes made by the Loeb–Sourirajan technique involving precipitation of a casting solution by immersion in a nonsolvent (water) bath. Also covered are a variety of related techniques such as precipitation by solvent evaporation, precipitation by absorption of water from the vapor phase, and precipitation by cooling.
- **Interfacial composite membranes:** This type of anisotropic membrane is made by polymerizing an extremely thin layer of polymer at the surface of a microporous support polymer.
- **Solution-coated composite membranes:** To prepare these membranes, one or more thin, dense polymer layers are solution coated onto the surface of a microporous support.
- **Other anisotropic membranes:** This category covers membranes made by a variety of specialized processes, such as plasma deposition, in the laboratory or on a small industrial scale, to prepare anisotropic membranes for specific applications.

NIPS Non-solvent induced phase separation

Nylon rope trick (water/cyclohexane)

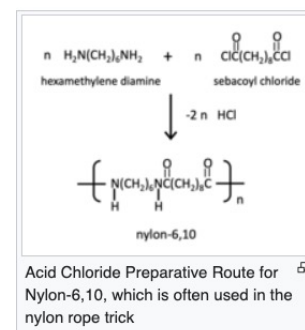


Table 3.1 Phase separation membrane preparation procedures

Procedure	Process
Water precipitation (the Loeb–Sourirajan process)	The cast polymer solution is immersed in a nonsolvent bath (typically water). Absorption of water and loss of solvent cause the film to rapidly precipitate from the top surface down
Water vapor absorption	The cast polymer solution is placed in a humid atmosphere. Water vapor absorption causes the film to precipitate
Thermal gelation	The polymeric solution is cast hot. Cooling causes precipitation
Solvent evaporation	A mixture of solvents is used to form the polymer casting solution. Evaporation of one of the solvents after casting changes the solution composition and causes precipitation

NIPS Non-solvent induced phase separation

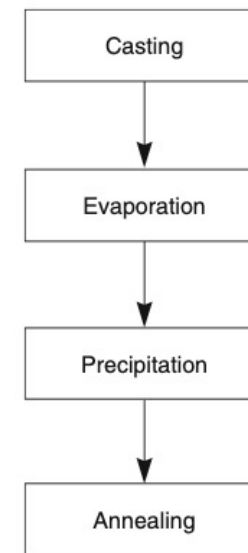


Figure 3.7 Process scheme used to form Loeb–Sourirajan water precipitation phase separation membranes [15]

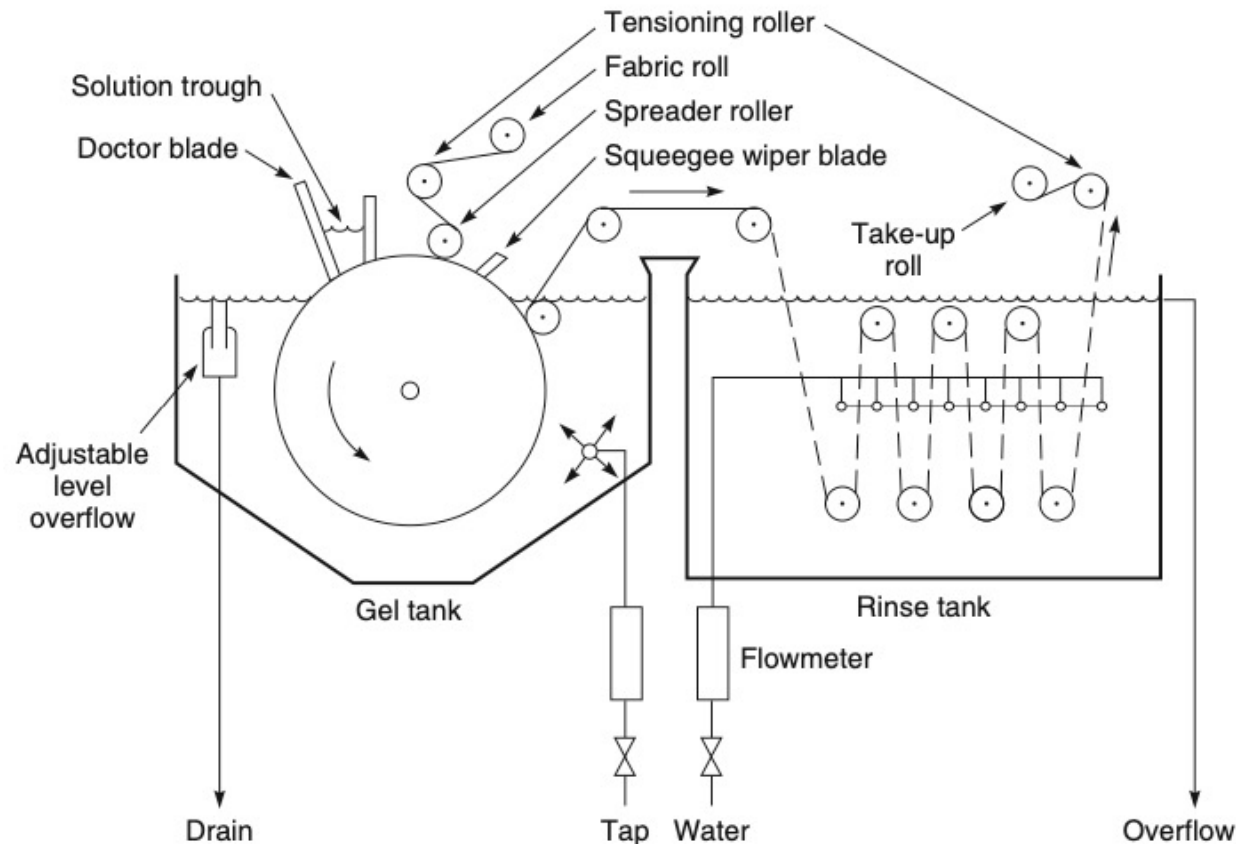


Figure 3.9 Schematic of Loeb–Sourirajan membrane casting machine used to prepare reverse osmosis or ultrafiltration membranes. A knife and trough are used to coat the casting solution onto a nonwoven paper web. The coated web then enters the water-filled gel tank, where the casting solution precipitates. After the membrane has formed, it is washed thoroughly to remove residual solvent before being wound up on the take-up roll

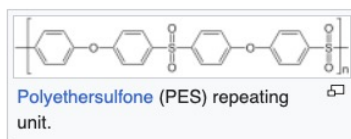
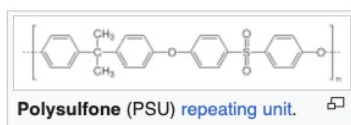
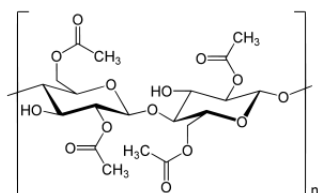


Table 3.2 Historically important examples of conditions for preparation of solution-precipitation (Loeb–Sourirajan) membranes

Casting solution composition	Precipitation conditions	Application and comments
22.2 wt% cellulose acetate (39.8 wt% acetyl polymer) 66.7 wt% acetone 10.0 wt% water 1.1 wt% magnesium perchlorate	3 min evaporation, precipitate into 0°C water, anneal for 5 min at 65–85°C	The first Loeb–Sourirajan reverse osmosis membrane [15]
25 wt% cellulose acetate (39.8 wt% acetyl polymer) 45 wt% acetone 30 wt% formamide	0.5–2 min evaporation, cast into 0°C water, anneal for 5 min at 65–85°C	The Manjikian formulation widely used in early 1970s for reverse osmosis membranes [21]
8.2 wt% cellulose acetate (39.8 wt% acetyl polymer) 8.2 wt% cellulose triacetate (43.2 wt% acetyl polymer) 45.1 wt% dioxane 28.7 wt% acetone 7.4 wt% methanol 2.5 wt% maleic acid	Up to 3 min evaporation at 10°C, precipitation into an ice bath, anneal at 85–90°C for 3 min	A high-performance reverse osmosis cellulose acetate blend membrane [22]
15 wt% polysulfone (Udell P 1700) 85 wt% <i>N</i> -methyl-2- pyrrolidone	Cast into 25°C water bath. No evaporation or annealing step necessary	An early ultrafiltration membrane formulation [23]. Similar polysulfone-based casting solutions are still widely used
20.9 wt% polysulfone 33.2 wt% dimethyl formamide 33.2 wt% tetrahydrofuran 12.6 wt% ethanol	Forced evaporation with humid air 10–15 s. Precipitate into 20°C water	A high-performance gas separation membrane with a completely dense nonporous skin ~1000 Å thick [24]

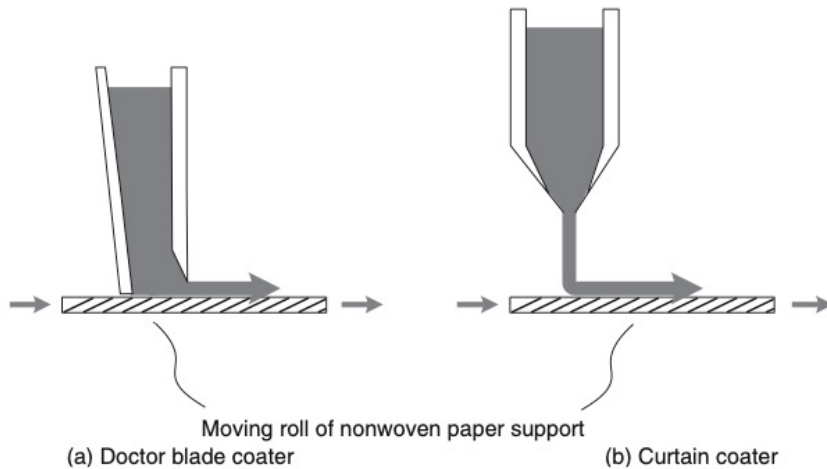
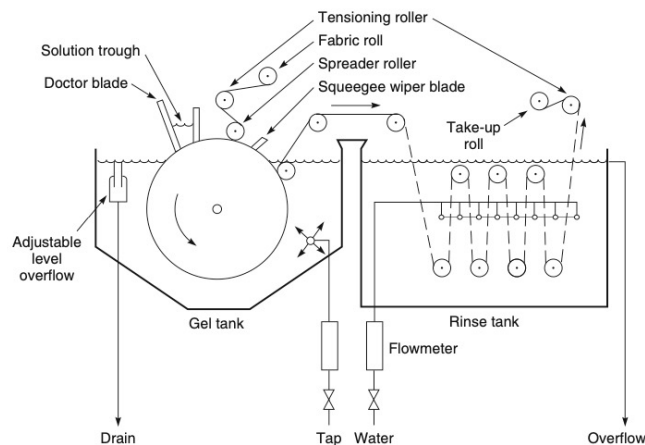


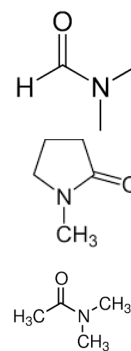
Figure 3.10 Doctor blade coating of casting solution onto a moving paper web is simple and easy, but curtain coaters give a better product with large scale production equipment



Water Precipitation

Polymer: Cellulose acetate, polysulfone, PVDF, polyetherimide, aromatic polyamides
 Tough, amorphous, thermoplastic, $T_g > T_{use} + 50^\circ\text{C}$, high MW (injection molding 30-50kDa, solution ppt. > 100kDa), soluble in water-miscible solvent but not water.

DMF



Casting Solution: aprotic solvents DMF, NMP, dimethyl acetamide. High solubility solvents for fast precipitation. Low d solvents, acetone, dioxane, THF, ethyl formate can be added as modifiers.

Higher concentration reduces porosity and flux.
 Ultrafiltration 15-20wt% polymer. 25 wt% reverse osmosis. 35 wt% for hollow fiber membranes spun hot 60-80°C

Precipitation Medium: Water

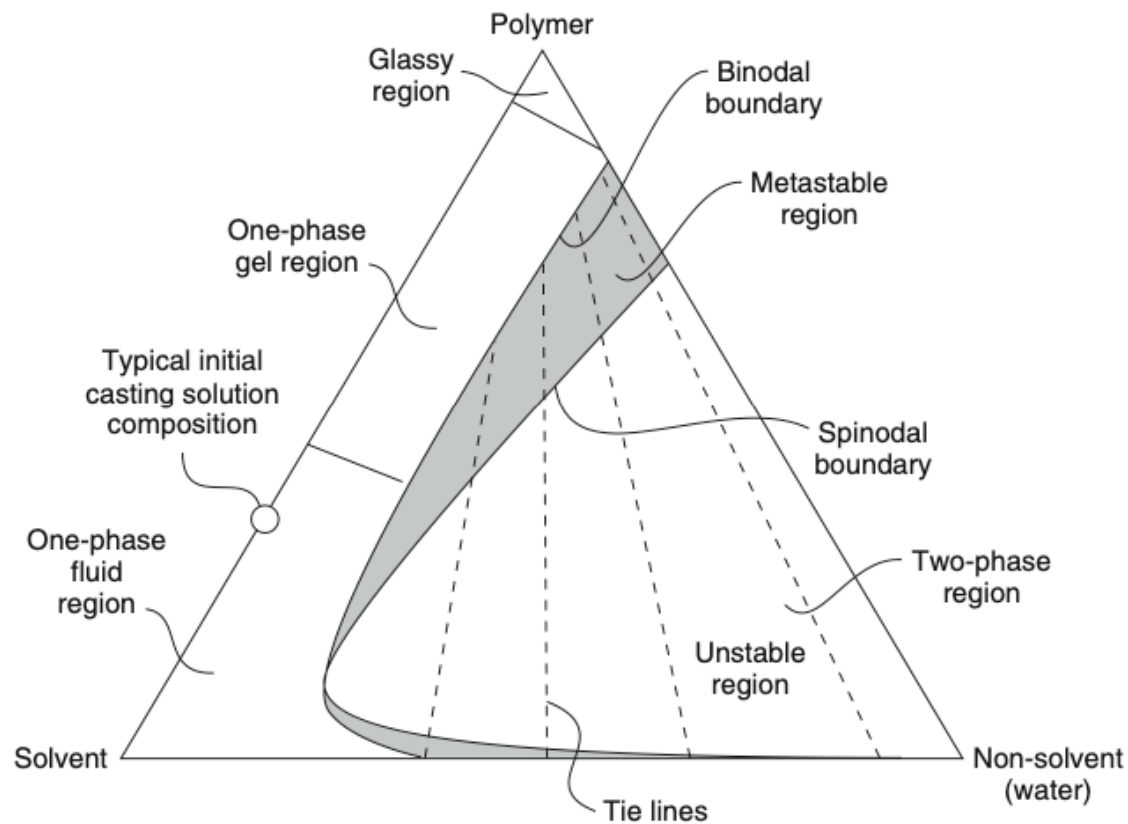


Figure 3.12 Schematic of the three-component phase diagram often used to rationalize the formation of water-precipitation phase separation membranes. In the two-phase region of the diagram, tie lines link the precipitated polymer-rich phase with its equilibrium polymer-poor phase

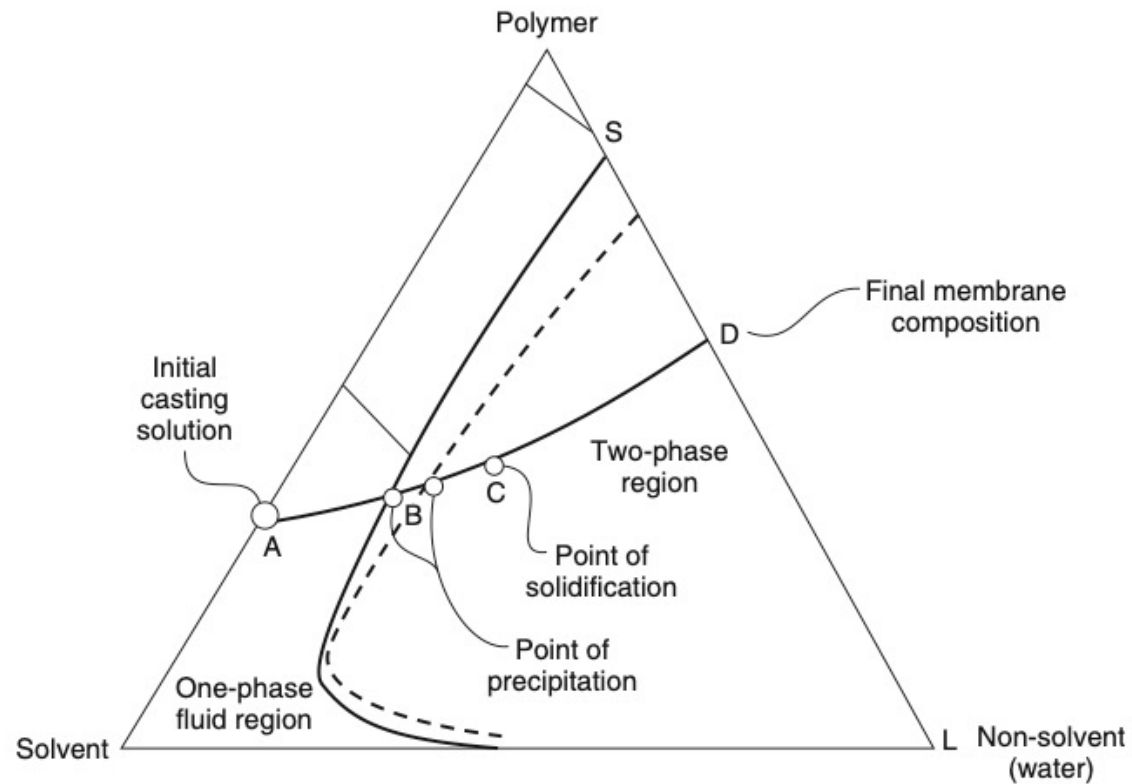


Figure 3.13 Membrane formation in water-precipitation membranes was first rationalized as a path through the three-component phase diagram from the initial polymer casting solution (A) to the final membrane (D) [25]

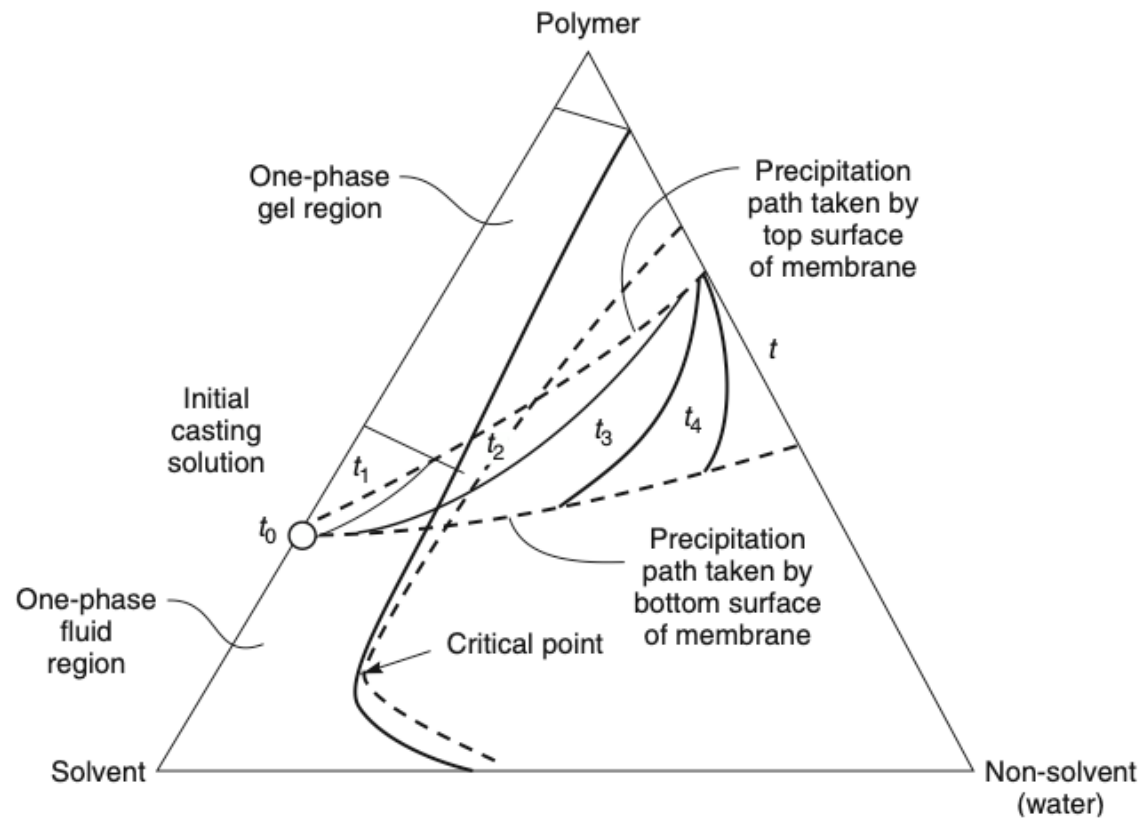
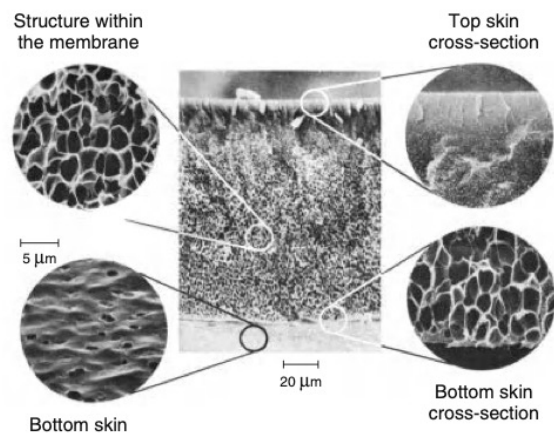
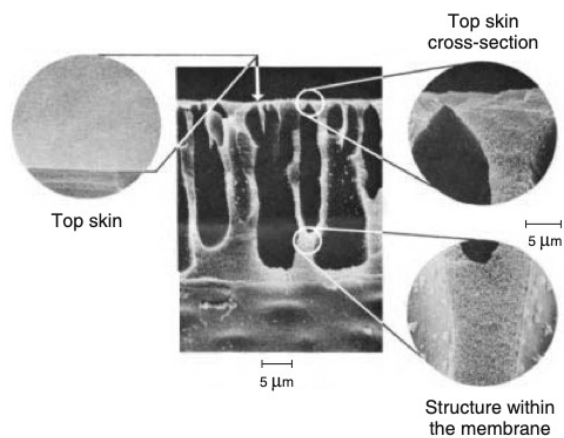
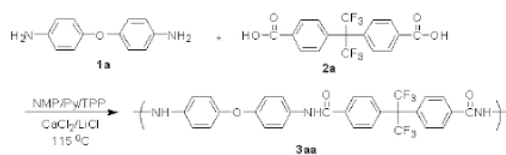


Figure 3.14 The surface layer of water-precipitation membranes precipitates faster than the underlying substrate. The precipitation pathway is best represented by the movement of a line through the three-component phase diagram [28]



(a) Sponge structure cast from 22 wt% Nomex in dimethylacetamide



(b) Finger structure cast from 18 wt% Nomex in dimethylacetamide

Figure 3.8 Scanning electron micrographs of aromatic polyamide (Nomex[®], Du Pont) Loeb–Sourirajan membranes cast from 22 and 18 wt% polymer in dimethylacetamide. Reprinted from Desalination, **16**, H. Strathmann, K. Kock, P. Amar and R.W. Baker, The formation mechanism of anisotropic membranes, p. 179, Copyright 1975. Reprinted from [20]. Copyright (1975) Elsevier.

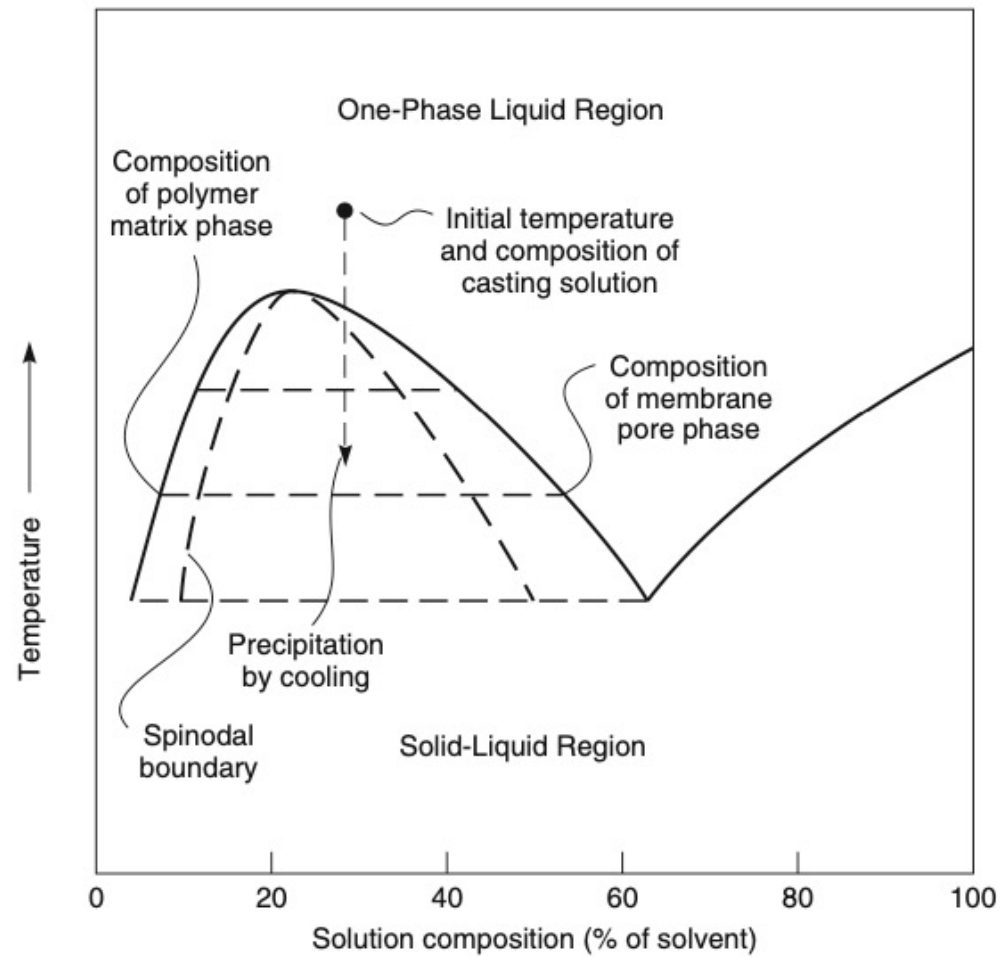
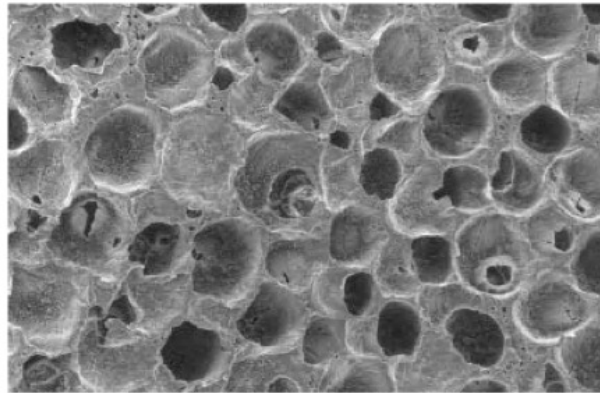
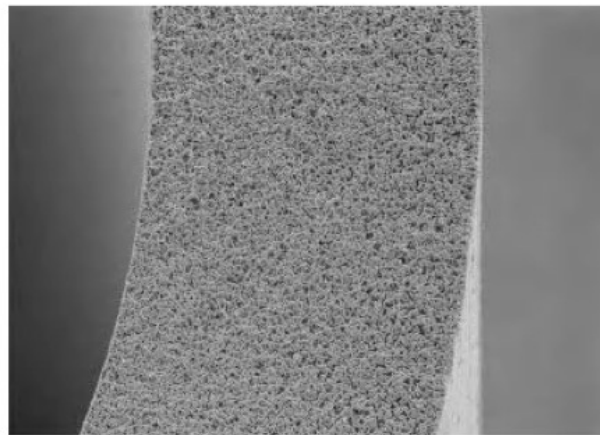


Figure 3.15 Phase diagram showing the composition pathway traveled by the casting solution during precipitation by cooling (thermal gelation)



(a)

50 μm



(b)

20 μm

Figure 3.16 Polypropylene structures (a) type I: open cell structure formed at low cooling rates and (b) type II: fine structure formed at high cooling rates. Reprinted with permission from [40]. Copyright (1985) American Chemical Society.

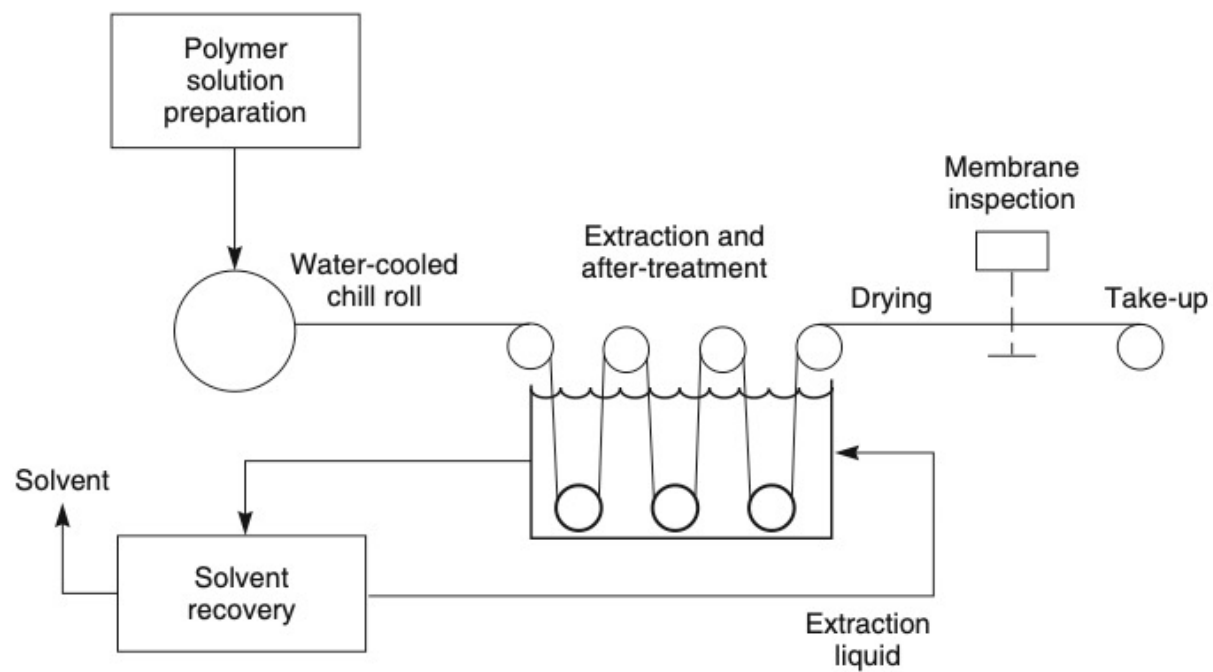


Figure 3.17 Equipment to prepare microporous membranes using the polymer precipitation by cooling technique. Reprinted with permission from [40]. Copyright (1985) American Chemical Society.

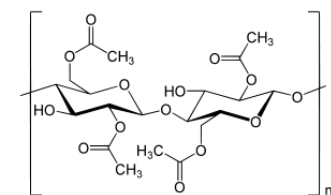
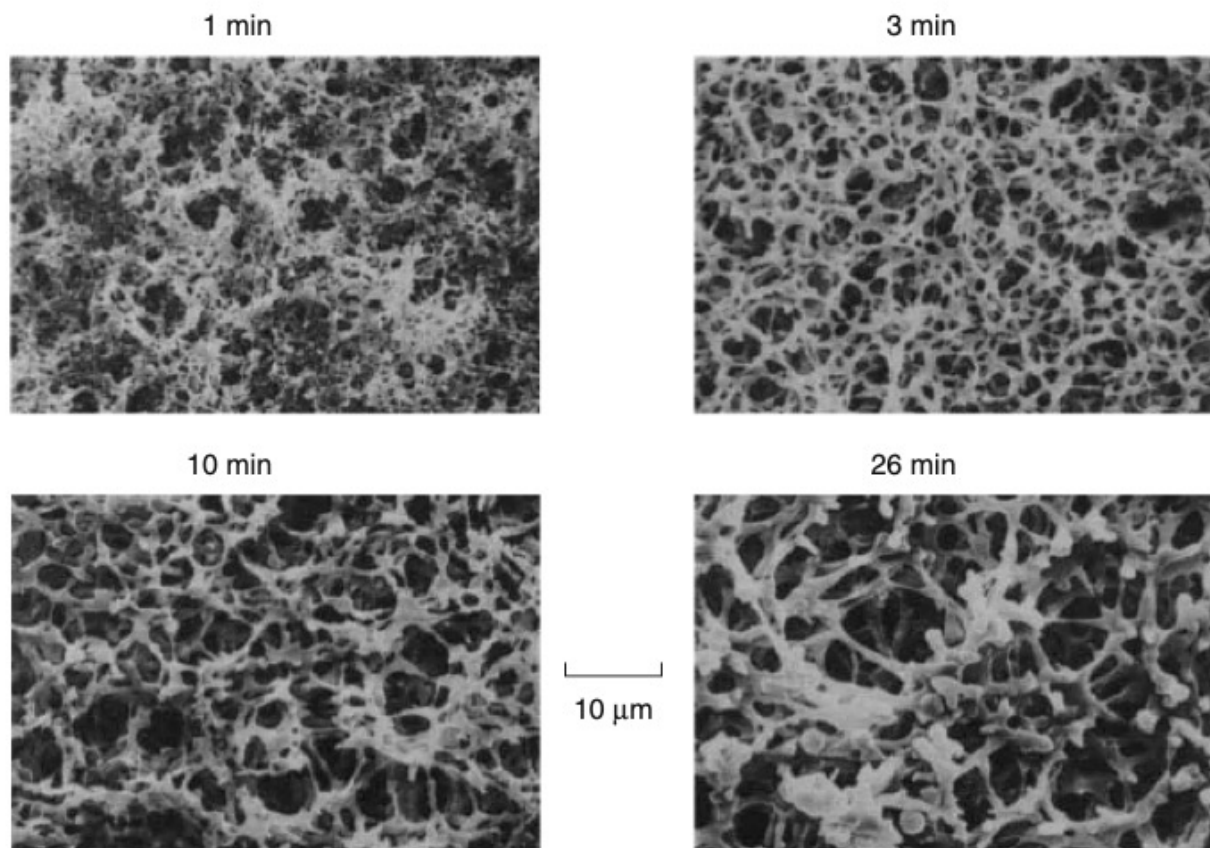


Figure 3.18 SEM photomicrographs of the bottom surface of cellulose acetate membranes cast from a solution of acetone (volatile solvent) and 2-methyl-2,4-pentanediol (nonvolatile nonsolvent). The evaporation time before the structure is fixed by immersion in water is shown. Reprinted with permission from [47]. Copyright (1994) Elsevier.

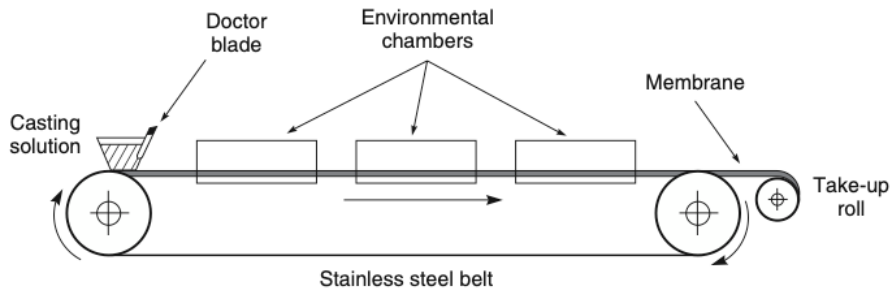


Figure 3.19 Schematic of casting machine used to make microporous membranes by water vapor absorption. A casting solution is deposited as a thin film on a moving stainless steel belt moving at about 0.3 m/min. The film passes through a series of humid and dry chambers, where the solvent evaporates from the solution, and water vapor is absorbed. This precipitates the polymer, forming a microporous membrane that is taken up on a collection roll. Reprinted with permission from [48]. Copyright (1969) Office of Saline Water Research and Development

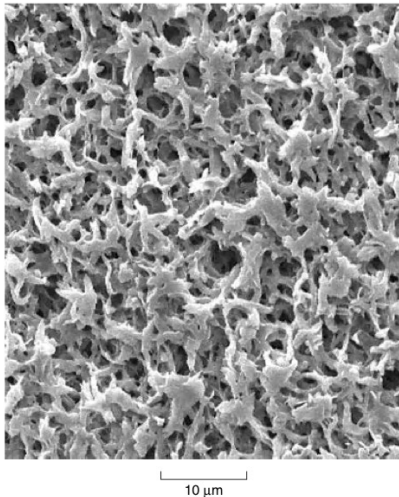


Figure 3.20 Characteristic structure of a phase-separation membrane made by water vapor absorption and solvent evaporation. Reprinted with permission of Millipore Corporation, Billerica, MA

Combination of solvent evaporation and absorption of water vapor:

5-10 component casting solution:

8.1wt% cellulose nitrate,

1.3% cellulose acetate,

49.5% acetone (volatile good solvent),

22.3% ethanol,

14.7% n-butanol (nonvolatile poor solvents)

2.6% water (nonsolvent)

0.5% Triton X-100 (non-ionic surfactant

PEO based),

1.2% glycerine (plasticizer)

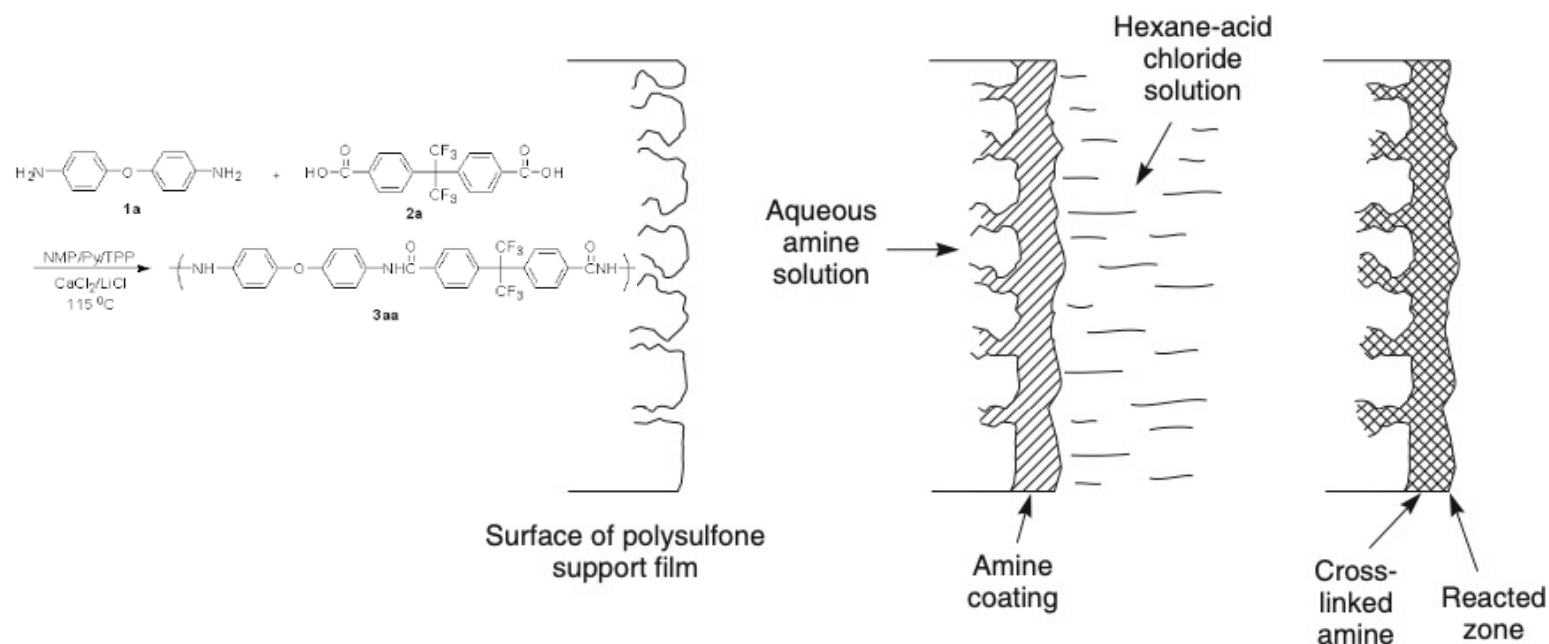
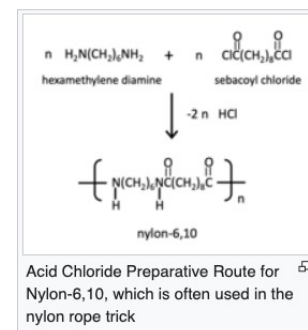


Figure 3.21 Schematic of the interfacial polymerization process. The microporous film is first impregnated with an aqueous amine solution. The film is then treated with a multivalent crosslinking agent dissolved in a water-immiscible organic fluid, such as hexane or Freon-113. An extremely thin polymer film forms at the interface of the two solutions [50]. Reprinted from L.T. Rozelle, J.E. Cadotte, K.E. Cobian, and C.V. Knopp, Jr., *Nonpolysaccharide Membranes for Reverse Osmosis: NS-100 Membranes*, in *Reverse Osmosis and Synthetic Membranes*, S. Sourirajan, (ed.), National Research Council Canada, Ottawa, Canada (1977) by permission from NRC Research Press

Nylon rope trick (water/cyclohexane)



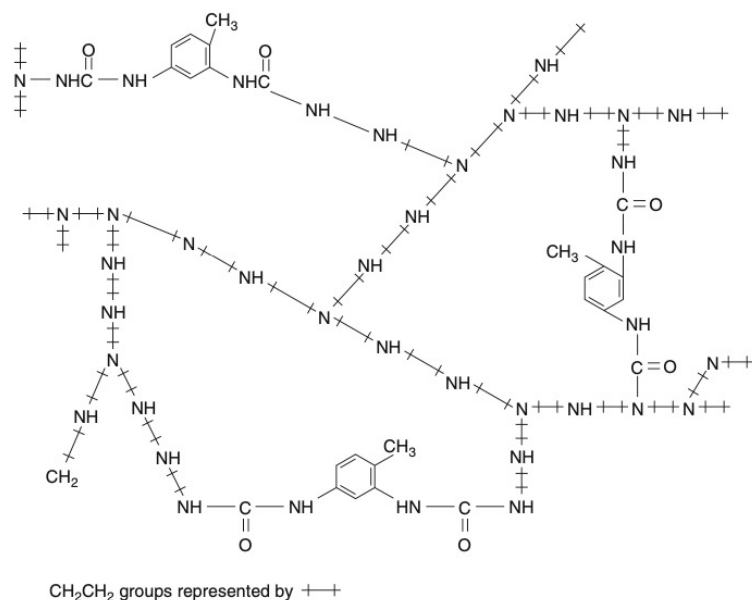


Figure 3.22 Idealized structure of polyethylenimine crosslinked with toluene 2,4-diisocyanate. This was called the NS-100 membrane. The chemistry was first developed by Cadotte to make interfacial reverse osmosis membranes with almost twice the water flux and 1/5th the salt leakage of the best reverse osmosis membranes then available. Even better membranes have since been developed by Cadotte and others [50]. Reprinted from L.T. Rozelle, J.E. Cadotte, K.E. Cobian, and C.V. Knopp, Jr., *Nonpolysaccharide Membranes for Reverse Osmosis: NS-100 Membranes*, in *Reverse Osmosis and Synthetic Membranes*, S. Sourirajan, (ed.), National Research Council Canada, Ottawa, Canada (1977) by permission from NRC Research Press

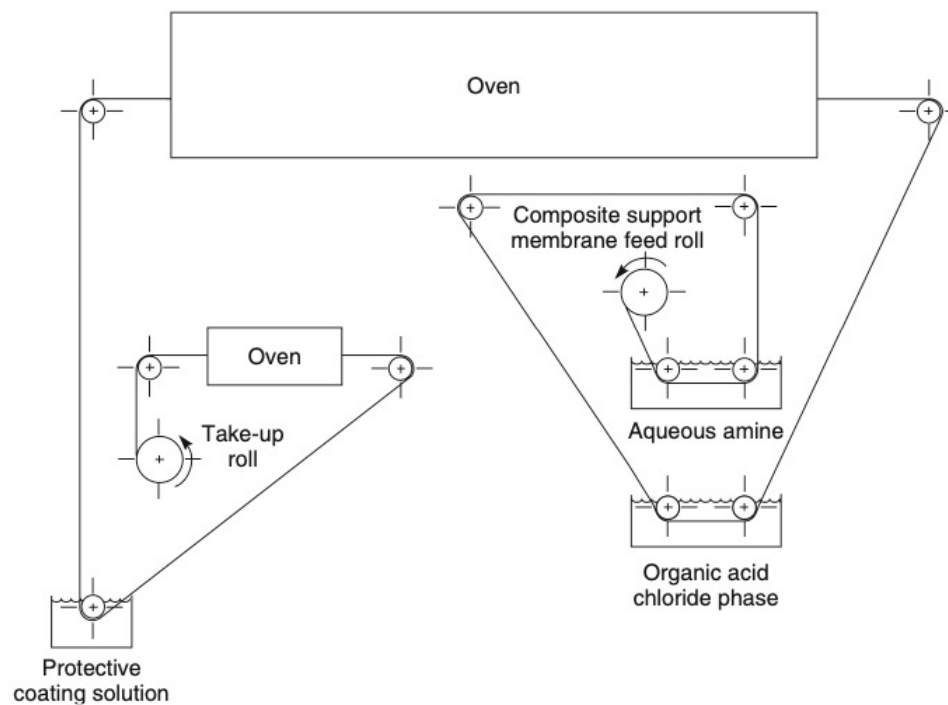


Figure 3.23 Schematic of the type of machinery used to make interfacial composite membranes

Solution-Coated Composite Membranes:

Langmuir Trough Method:

0.5-2.0 μm selective layer

Use Langmuir trough

Dilute polymer solution in volatile water-insoluble solvent on a water trough between Teflon[®] rods

Move rods apart to make thin film

Pickup the film on a microporous support

200Å films can be made

Riley method (meniscus technique):

Coat polymer solution on clean defect-free microporous support

50-100 μm liquid film dries to 0.5 – 2 μm layer

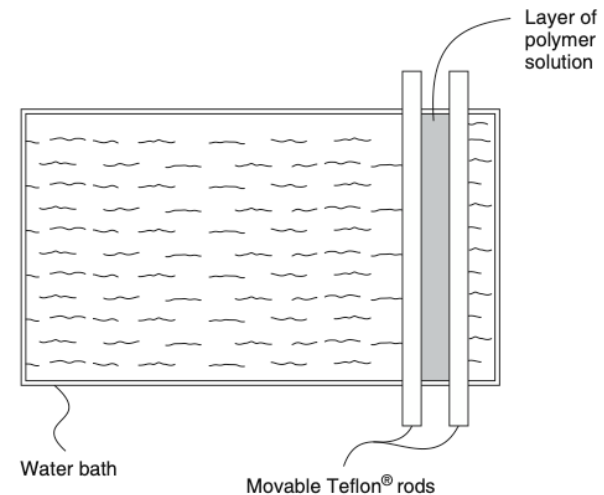


Figure 3.24 Schematic of the apparatus developed by Ward et al. to prepare water-cast composite membranes. Reprinted with permission from [17]. Copyright (1976) Elsevier.

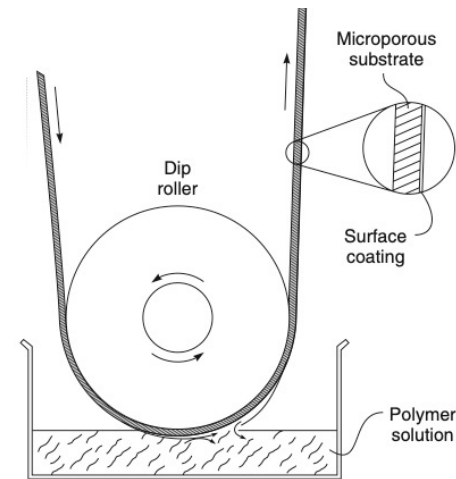


Figure 3.25 Schematic diagram of a film coating apparatus [59]

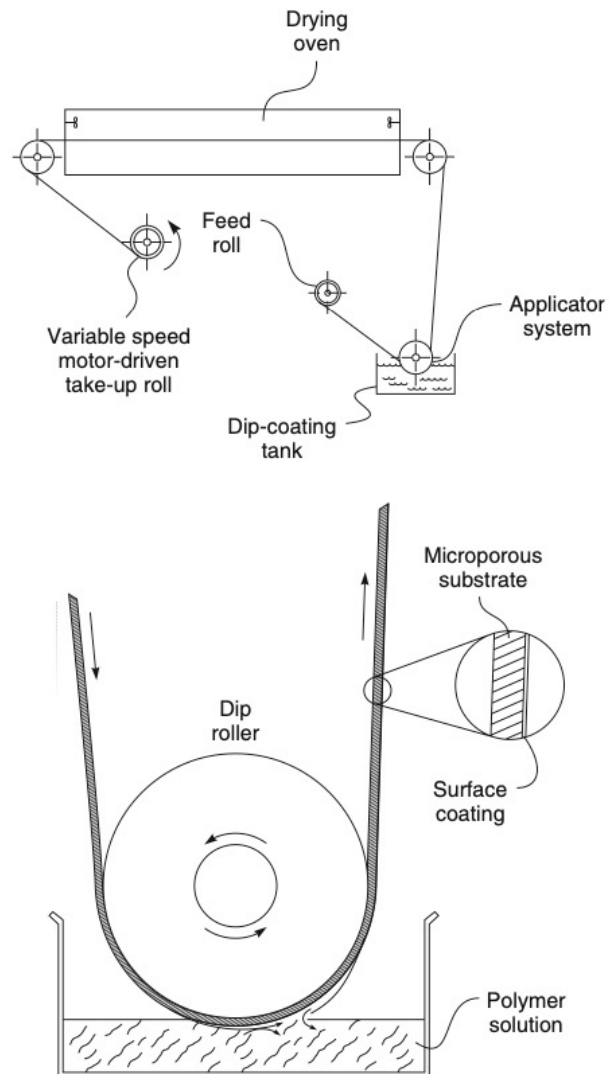


Figure 3.25 Schematic diagram of a film coating apparatus [59]

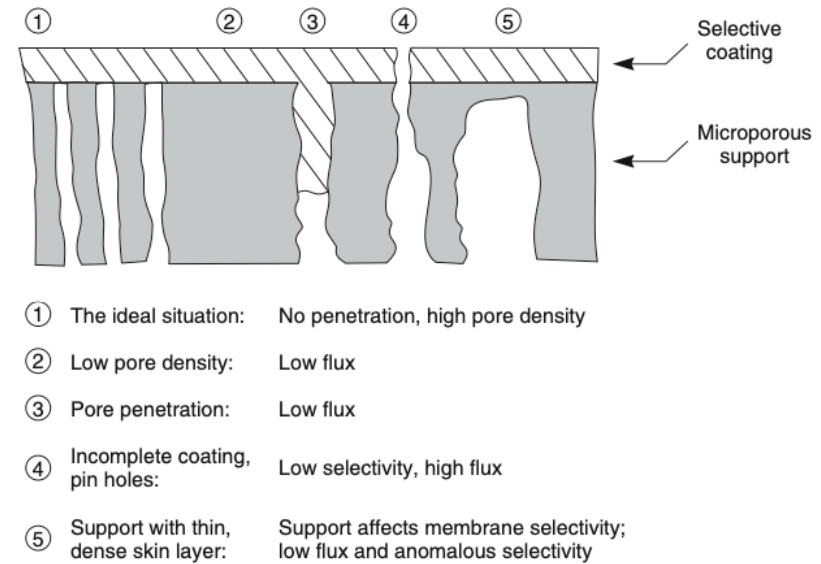
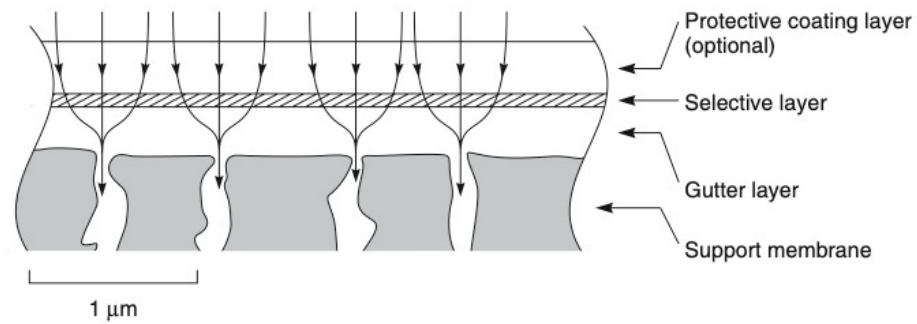
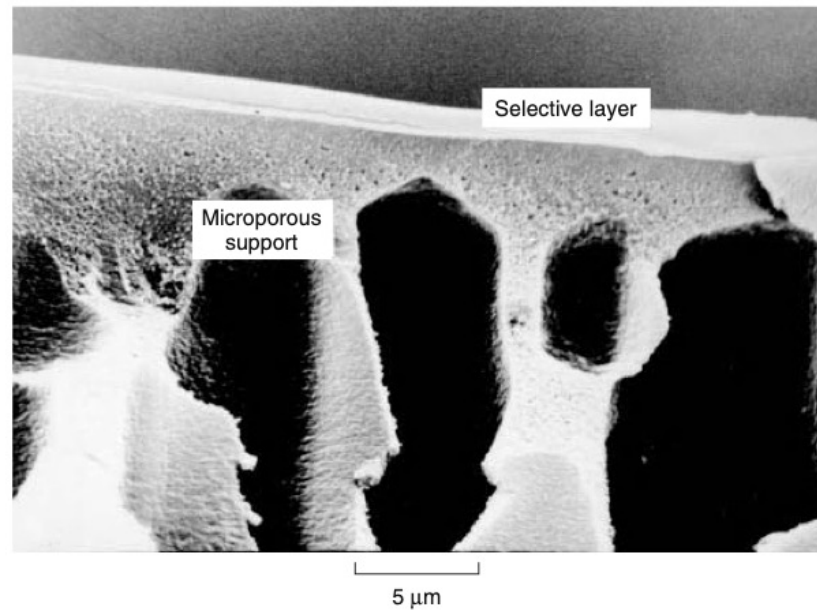


Figure 3.26 Support membrane properties that affect composite membrane performance. Reprinted with permission from [60]. Copyright (1991) Bakish Materials Corporation.



(a)



(b)

Figure 3.27 Schematic and scanning electron micrograph of a multilayer composite membrane on a microporous support. Reprinted with permission from Membrane Technology and Research, Inc. Copyright (2012) MTR.

Plasma Polymerized Membranes

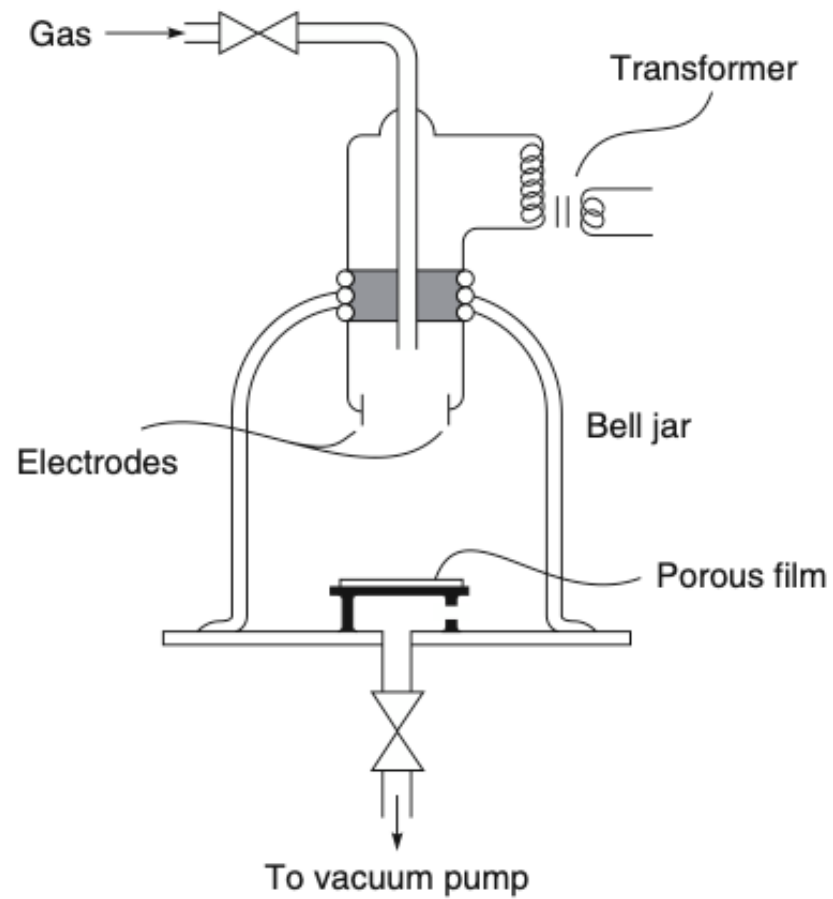


Figure 3.28 Simple bell jar plasma coating apparatus

Spin Coating Membranes

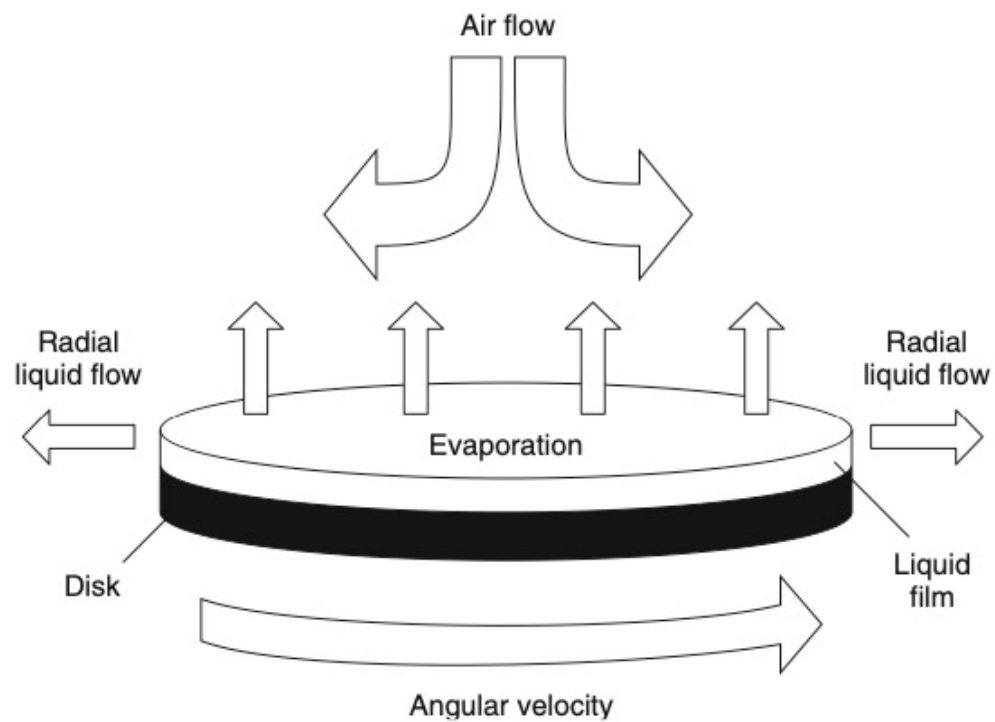


Figure 3.29 Schematic of a spin-coating process. Reprinted with permission from [66]. Copyright (2005) Royal Society of Chemistry.

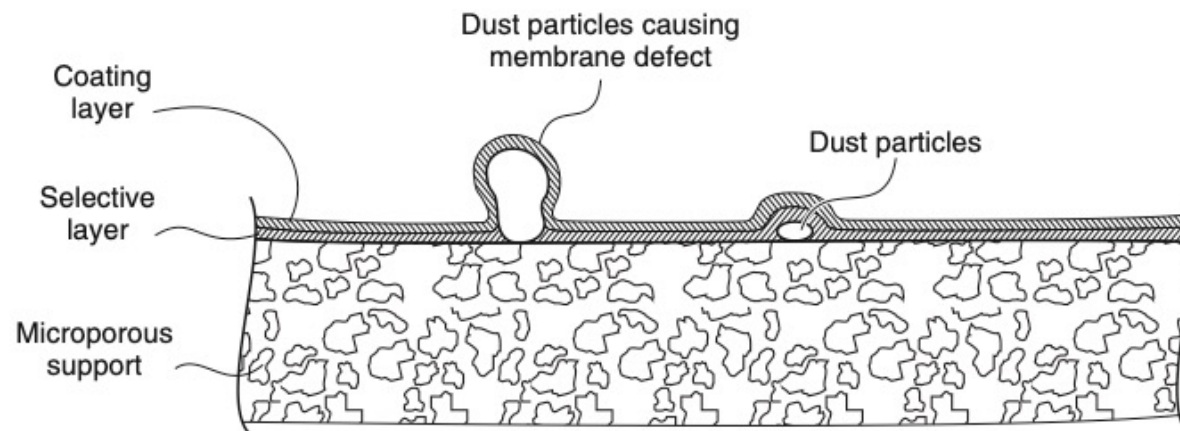


Figure 3.30 Method developed by Ward, Browell, and others at General Electric to seal membrane defects in composite membranes made by the water coating technique [76]

Poly dimethyl siloxane (PDMS) protective layer

Table 1. Hydrogen permeabilities and H₂/N₂ selectivities for various classes of polymers. See (4) for detailed values. The values given here are approximate and are intended to reflect general trends. Significant variations within classes can be found, and exceptions to the general trends exist.

Polymer	$P_{H_2} (\times 10^9 \text{ cm}^3 \text{ STP} / \text{cm}^2 \text{-sec-cmHg})$	$\alpha_{N_2}^{H_2}$
Silicone rubbers	100 to 500	1.5 to 3.0
Hydrocarbon rubbers	50 to 300	2.0 to 4.0
Polyphenylene oxides	50 to 100	10 to 20
Substituted polysulfones	20 to 70	15 to 25
Polycarbonates, polysulfones	0.5 to 20	25 to 75
Polyesters, nylons	0.5 to 3.0	50 to 150
Acrylonitrile copolymers (high concentration acrylonitrile)	0.1 to 1.0	100 to > 1000

1 April 1983, Volume 220, Number 4592

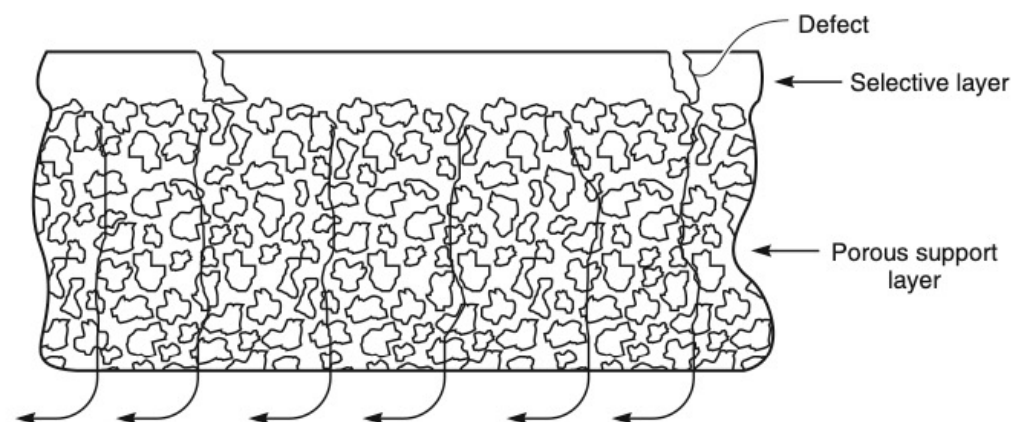
SCIENCE

Gas Separation Membranes

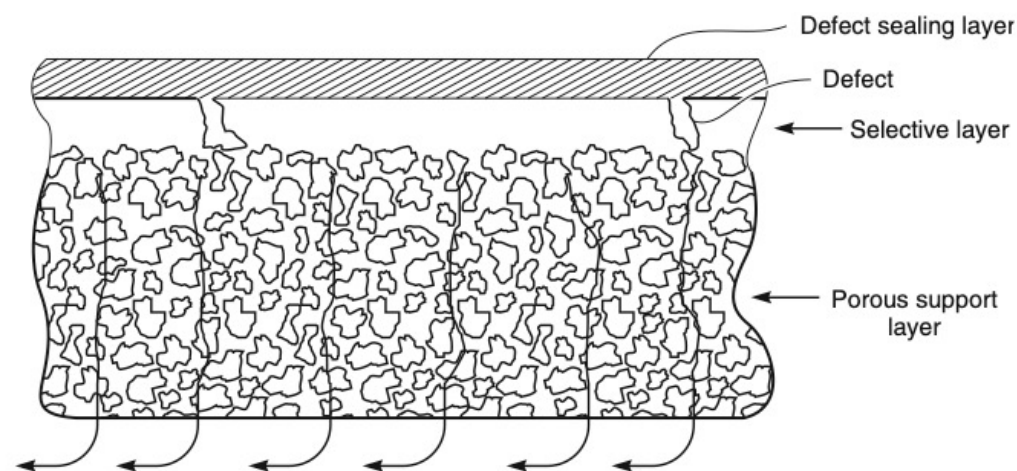
As applied to separations the term membrane generally refers to a thin polymer barrier, or occasional metal or liquid interface, between substances. While they can be used in many different ways (2, 3), most practical membrane-based separation systems utilize polymer membranes in the form of flat sheets or hollow fibers that are nonuniform in structure.

The Developing Technology of Gas Separating Membranes

Jay M. S. Henis and Mary K. Tripodi



(a) Defective Loeb-Sourirajan anisotropic membrane



(b) Henis and Tripodi silicone rubber-coated membrane

Figure 3.31 Schematic of (a) Loeb-Sourirajan and (b) Henis and Tripodi gas separation membranes [77]

For high pressure use thin fibers
Force = A x P on surface is lower

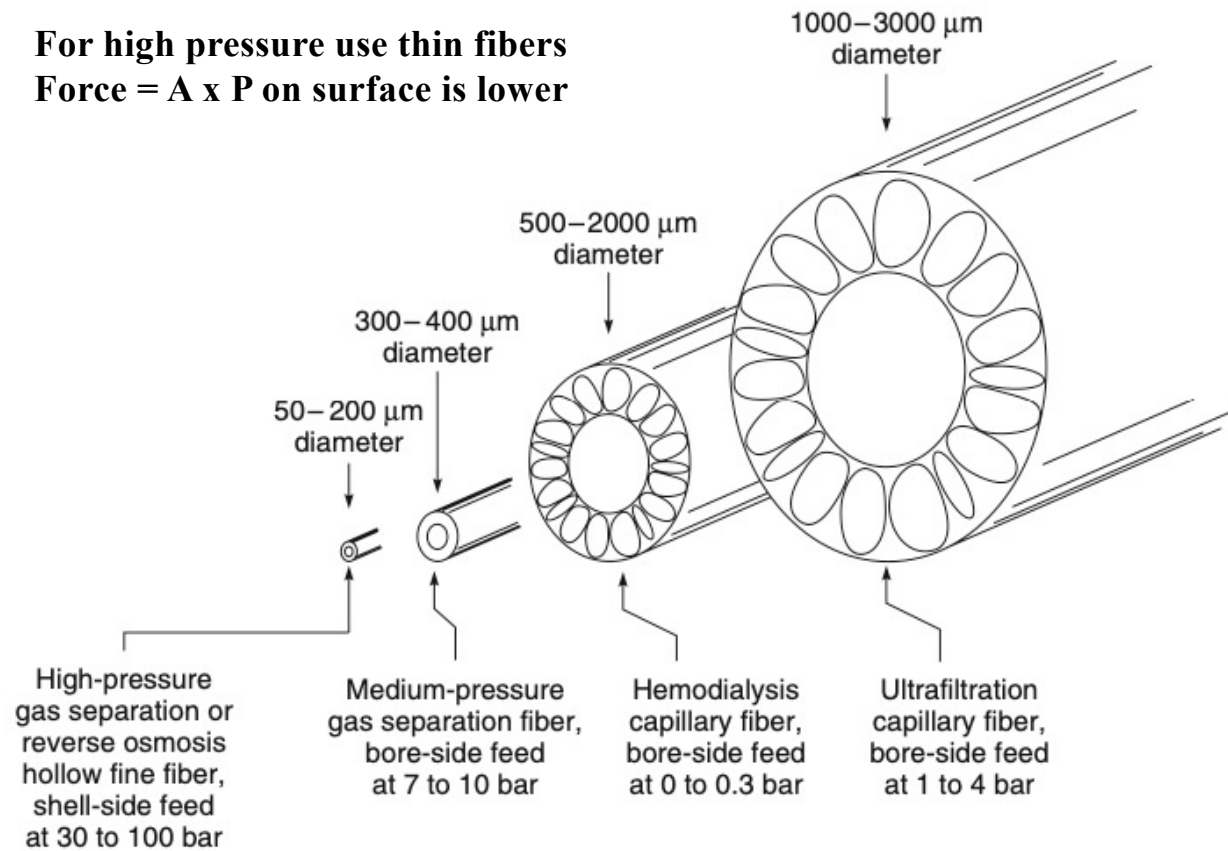


Figure 3.45 Schematic of the principal types of hollow fiber membranes

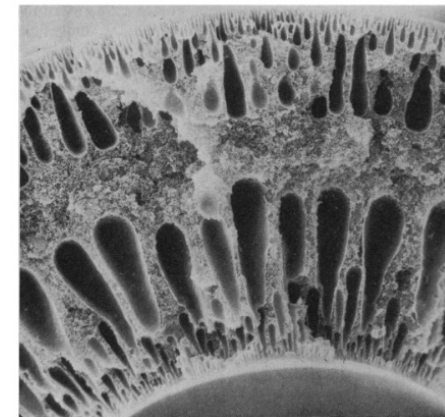


Fig. 1. Asymmetric hollow fiber. Fibers are typically spun from a water-miscible solvent into water.

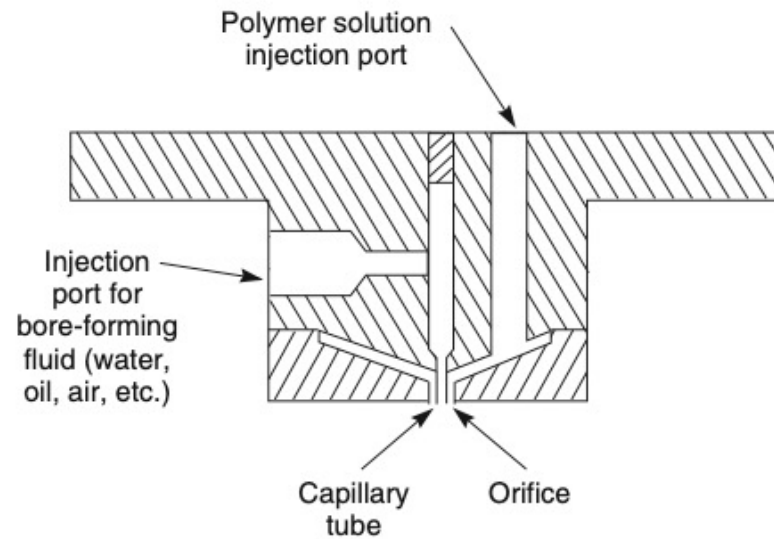


Figure 3.46 *Twin-orifice spinneret design used in solution-spinning of hollow fiber membranes. Polymer solution is forced through the outer orifice, while bore-forming fluid is forced through the inner capillary*

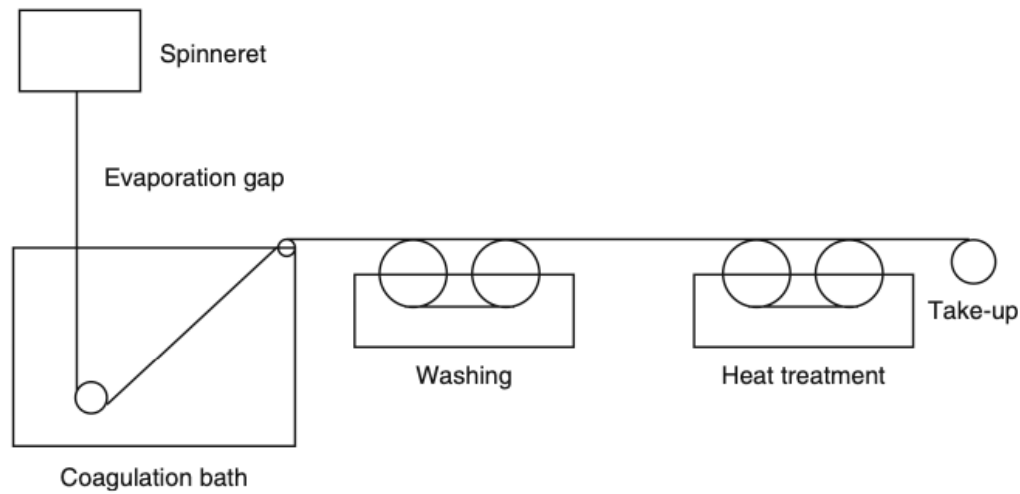


Figure 3.47 A complete hollow fiber solution-spinning system. The fiber is spun into a coagulation bath, where the polymer spinning solution precipitates forming the fiber. The fiber is then washed, dried, and taken up on a roll

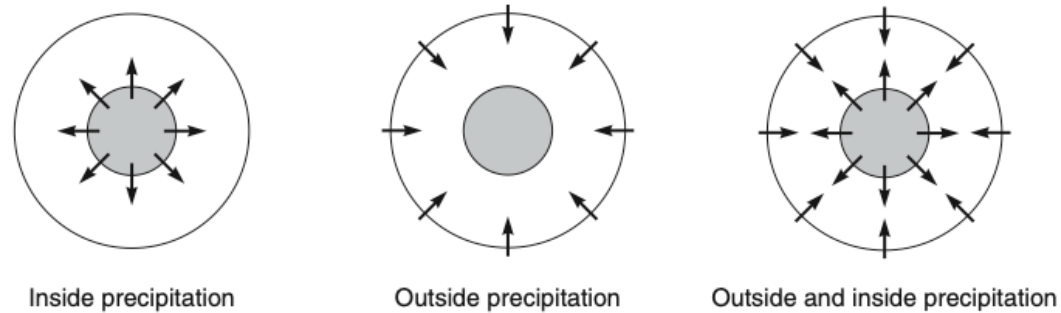
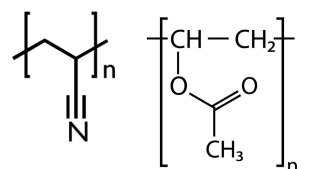
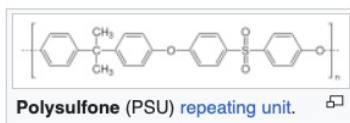


Figure 3.48 Depending on the bore fluid and the composition of the coagulation bath, the selective skin layer can be formed on the inside, the outside or both sides of the hollow fiber membrane. Reprinted with permission from [138]. Copyright (2007) Elsevier.



Polyvinyl Acetate
(C₄H₆O₂)_n

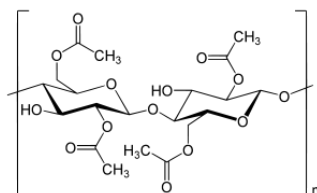


Table 3.4 Preparation parameters for various hollow fiber membranes

Casting dope	Bore fluid	Precipitation bath	Membrane type
37 wt% polysulfone (Udel P3500)	Water	Water 25–50°C	Gas separation fiber O ₂ /N ₂ selectivity = 5.2, ~50 μm diameter, anisotropic outside-skinned fibers, finely microporous substrate [132]
36 wt% N-methyl pyrrolidone 27 wt% propionic acid (spun at 15–100°C)			
25 wt% polyacrylonitrile-vinyl acetate copolymer 68 wt% dimethyl formamide	10 wt% dimethyl formamide in water	40 wt% dimethyl formamide in water 4°C	Ultrafiltration capillary membrane, inside skin, 98% rejection to 110 000 MW dextran [133]
7 wt% formamide (spun at 65°C)			
69 wt% cellulose triacetate (spun at 200°C)	Air	No precipitation bath used; fiber forms on cooling. Solvents removed in later extraction step	Early (Dow) 80-μm-diameter fine fiber reverse osmosis membrane [127]
17.2 wt% sulfolane 13.8 wt% polyethylene glycol (MW 400)			

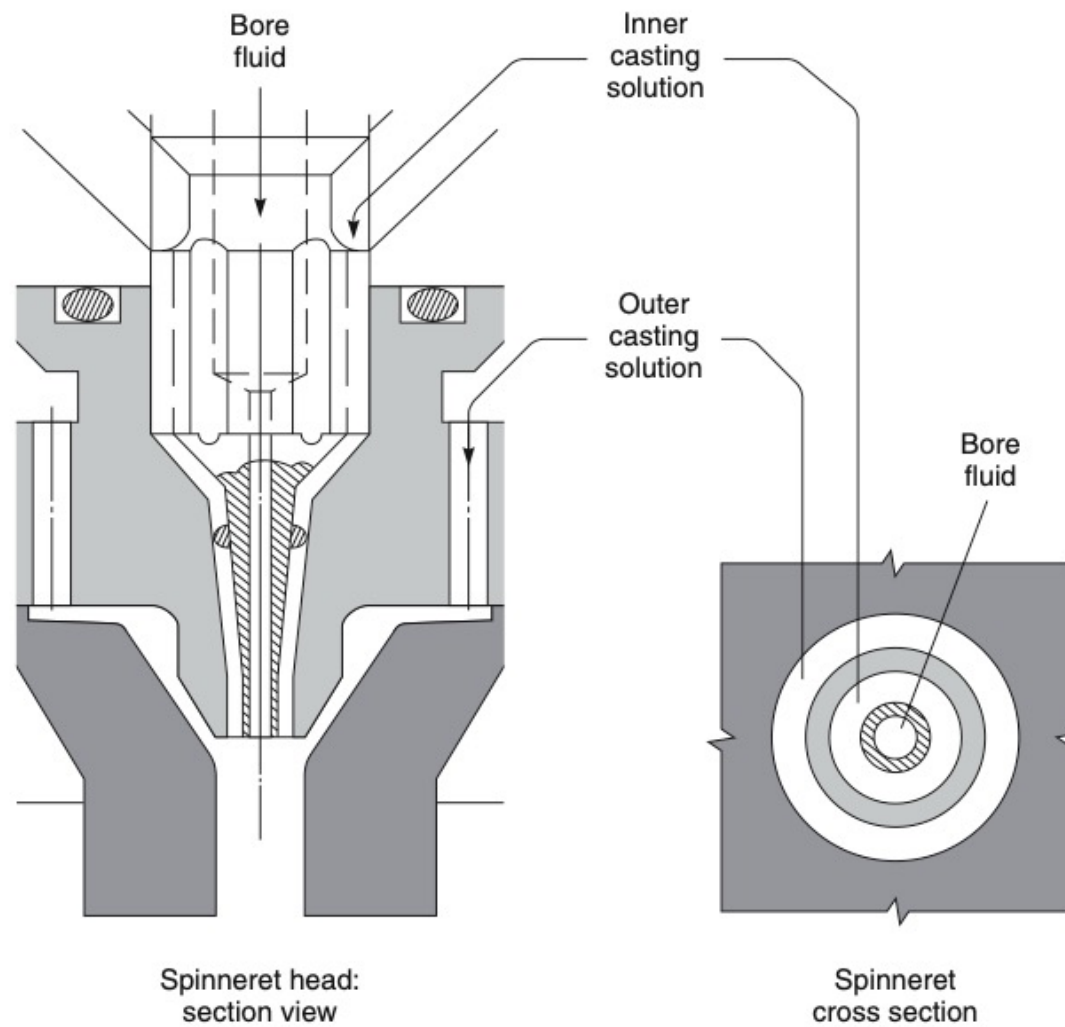
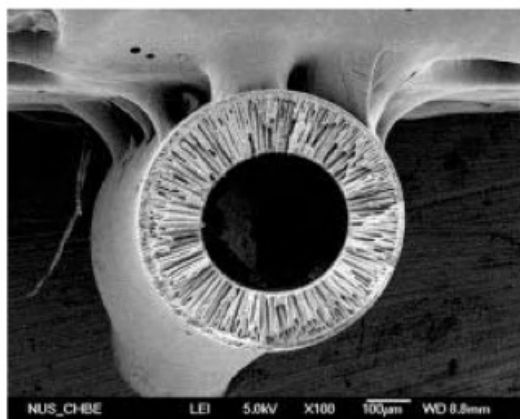
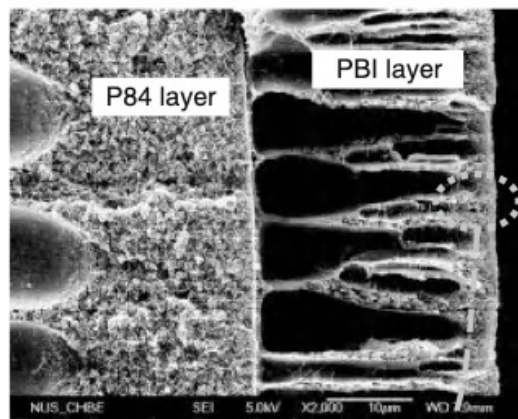


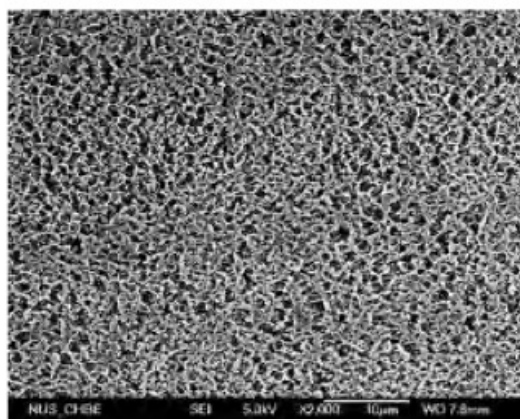
Figure 3.49 A double capillary spinneret sometimes used to produce two-layer hollow fibers. (After Kopp et al. [138].)



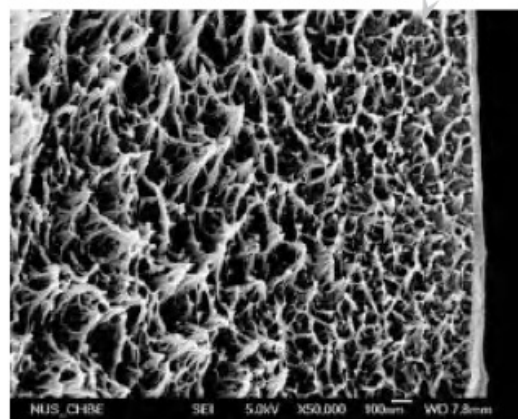
Cross-section



Enlarged outer layer



Inner porous surface



Cross-section near the outer skin

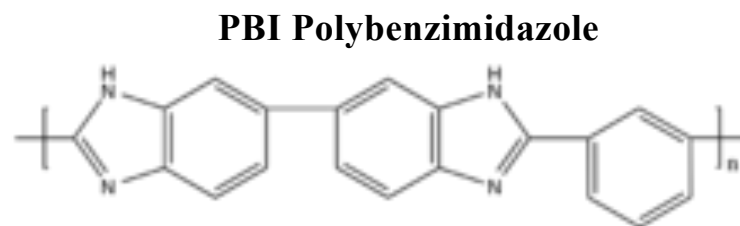
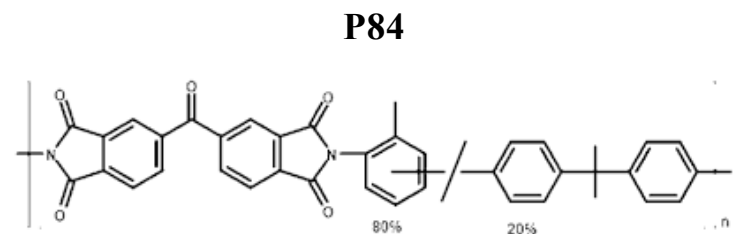


Figure 3.50 Scanning electron micrographs of dual-layer hollow fiber membranes made from an inner core of P84 polyimide and an outer shell of PBI. Reprinted with permission from [142]. Copyright (1965) American Chemical Society.

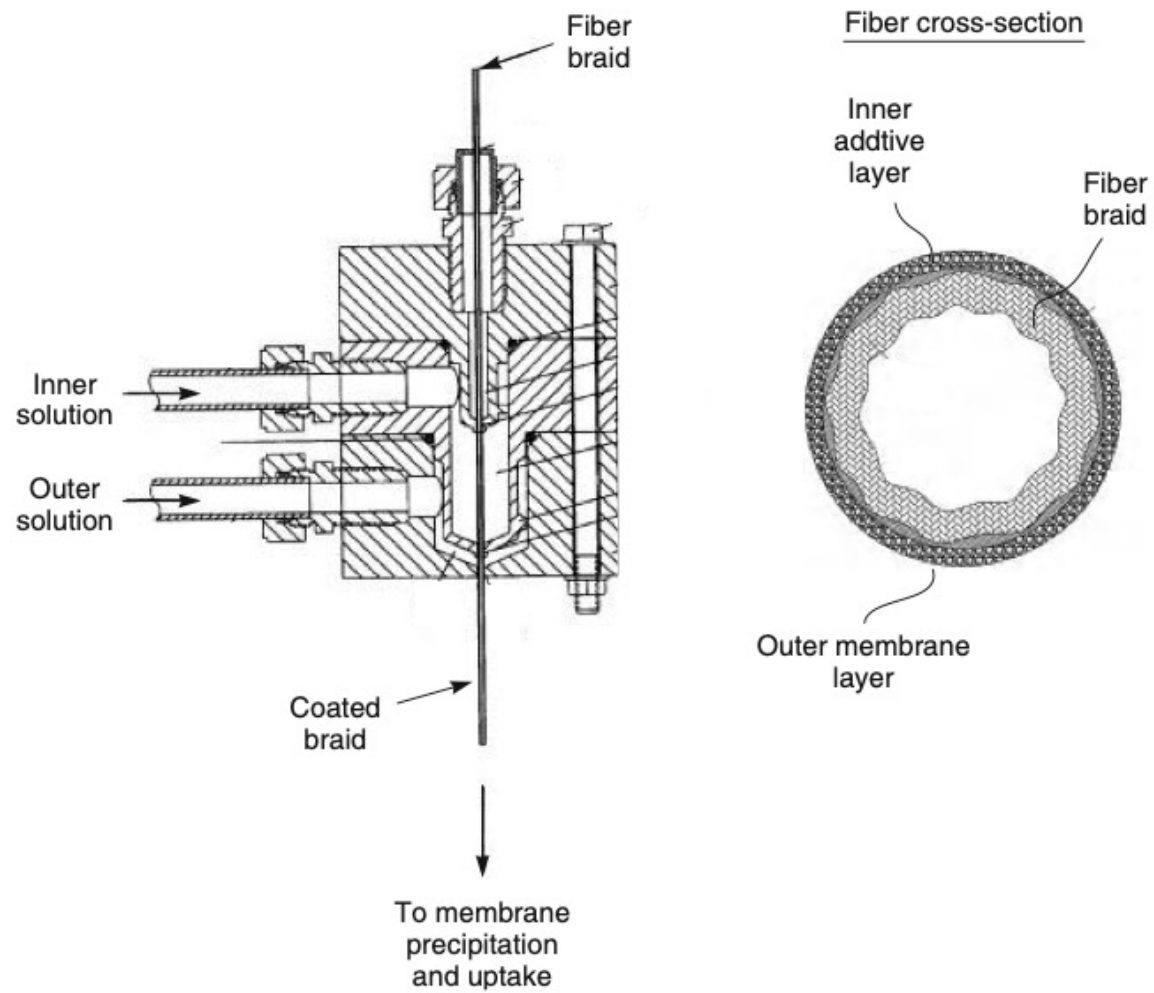


Figure 3.51 Dual-layer spinneret used to make braid-reinforced hollow fiber membranes [142]

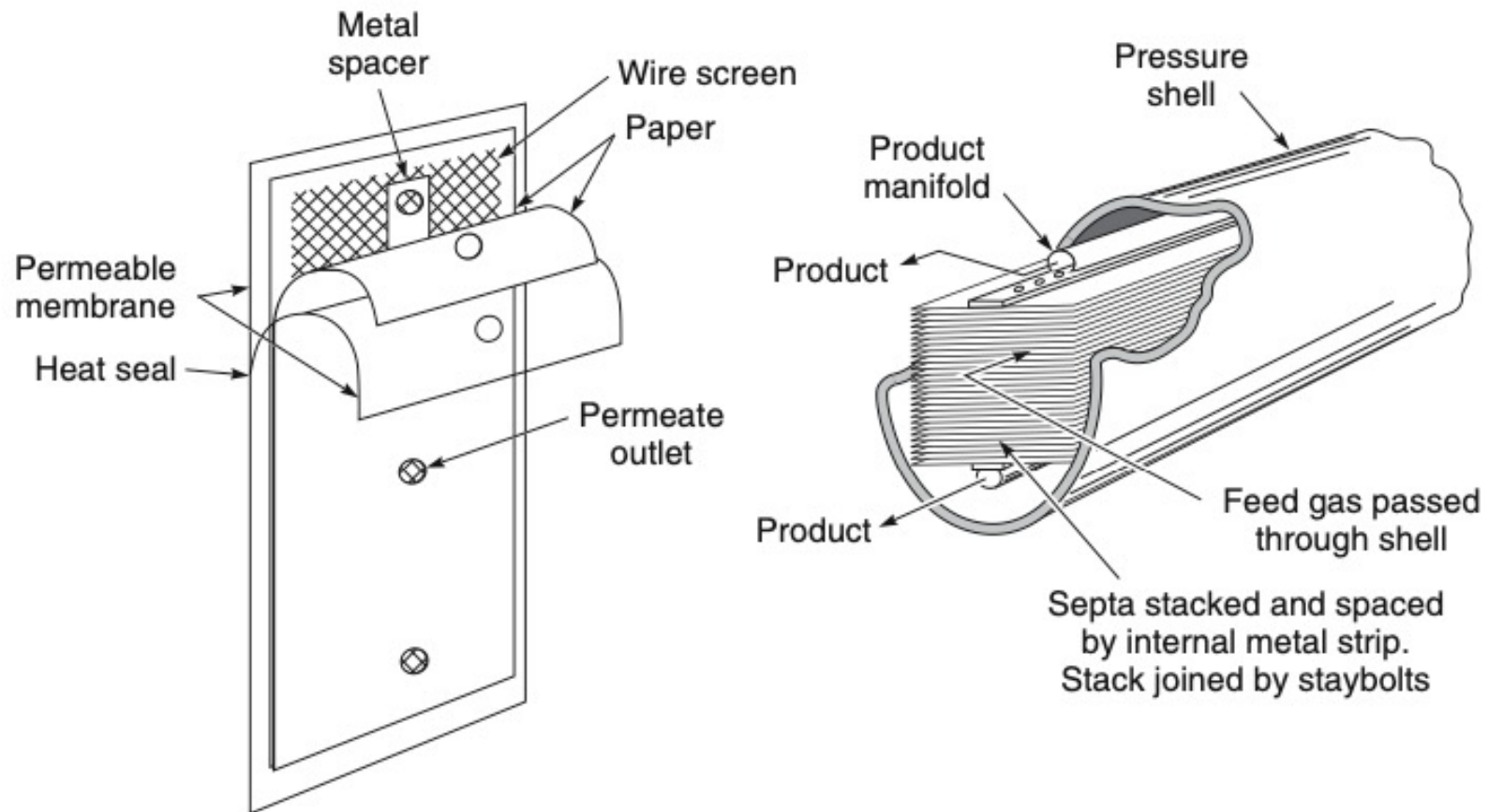


Figure 3.52 Early plate-and-frame design developed by Stern et al. [145] for the separation of helium from natural gas. Reprinted with permission from Koch Membrane Systems Inc. Copyright (2011) Koch Membrane Systems Inc.

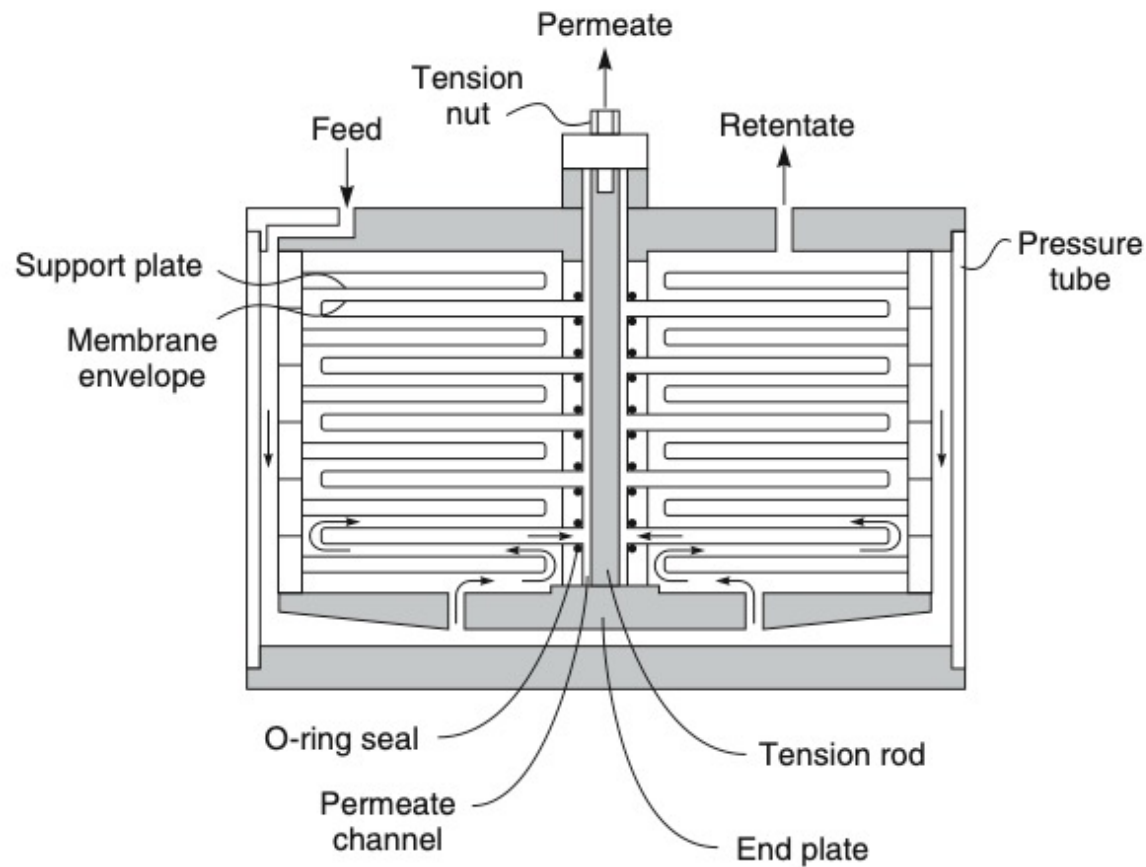


Figure 3.53 Schematic of a plate-and-frame module. Plate-and-frame modules provide good flow control on both the permeate and feed side of the membrane, but the large number of spacer plates and seals lead to high module costs. The feed solution is directed across each plate in series. Permeate enters the membrane envelope and is collected through the central permeate collection channel [146]



Figure 3.54 Typical tubular ultrafiltration module design. The membrane is usually cast on a porous fiberglass or paper support, which is then nested inside a plastic or steel support tube. In the past, each plastic housing contained a single 2–3 cm-diameter tube. More recently, several 0.5–1.0 cm-diameter tubes, nested inside single housings, have been introduced. (Courtesy of Koch Membrane Systems.)

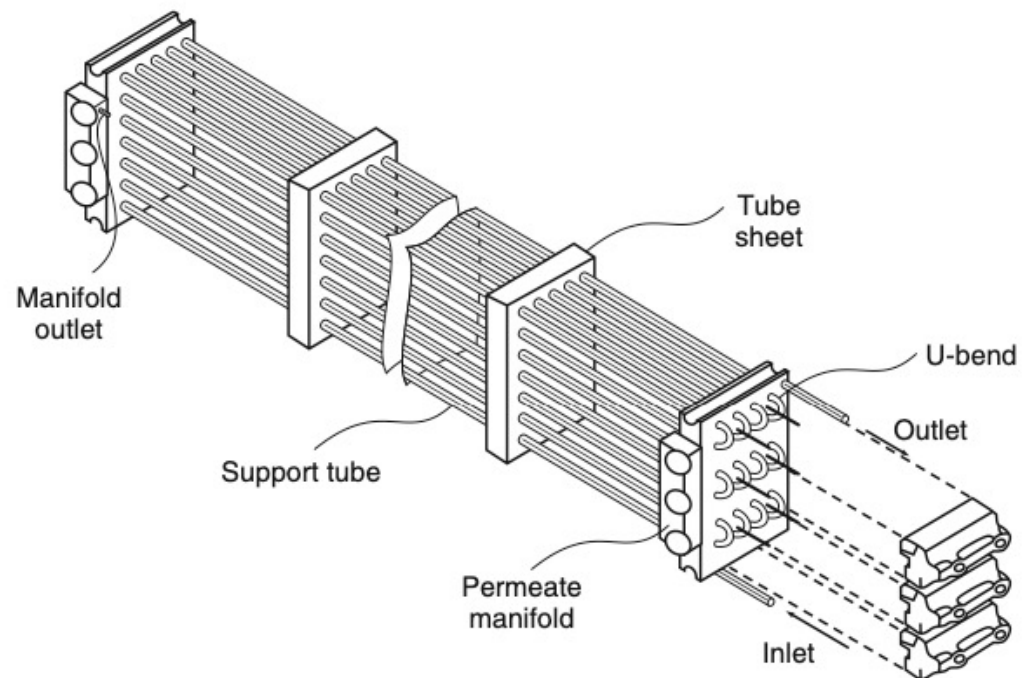


Figure 3.55 Exploded view of a tubular ultrafiltration system in which 30 tubes are connected in series. Permeate from each tube is collected in the permeate manifold

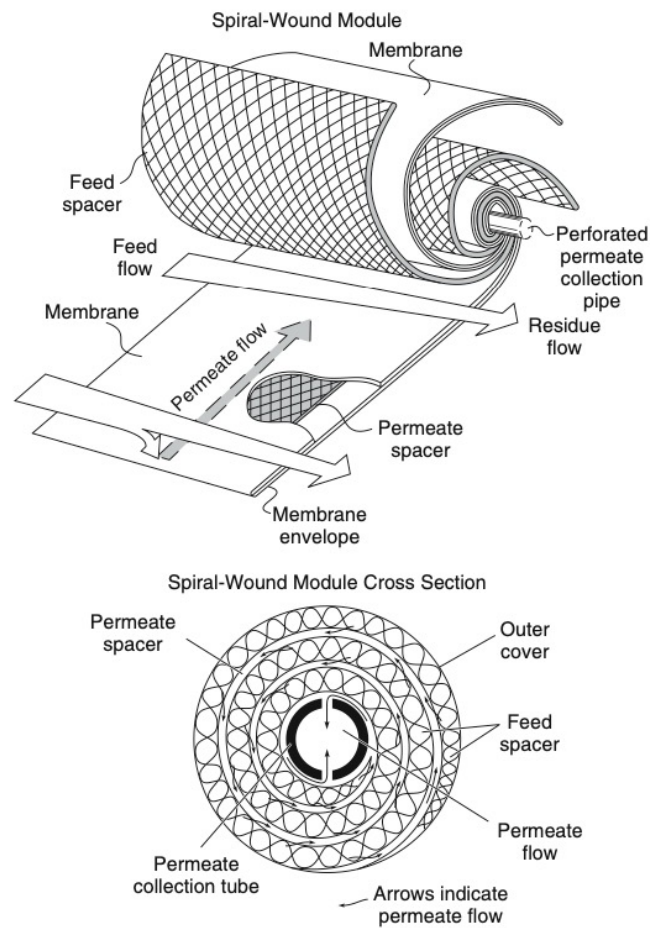


Figure 3.56 Exploded view and cross-section drawings of a spiral-wound module. Feed solution passes across the membrane surface. A portion passes through the membrane and enters the membrane envelope where it spirals inward to the central perforated collection pipe. One solution enters the module (the feed) and two solutions leave (the residue and the permeate). Spiral-wound modules are the most common module design for reverse osmosis and ultrafiltration as well as for high-pressure gas separation applications in the natural gas industry. Reprinted with permission from [147]. Copyright (1988) Taylor and Francis.

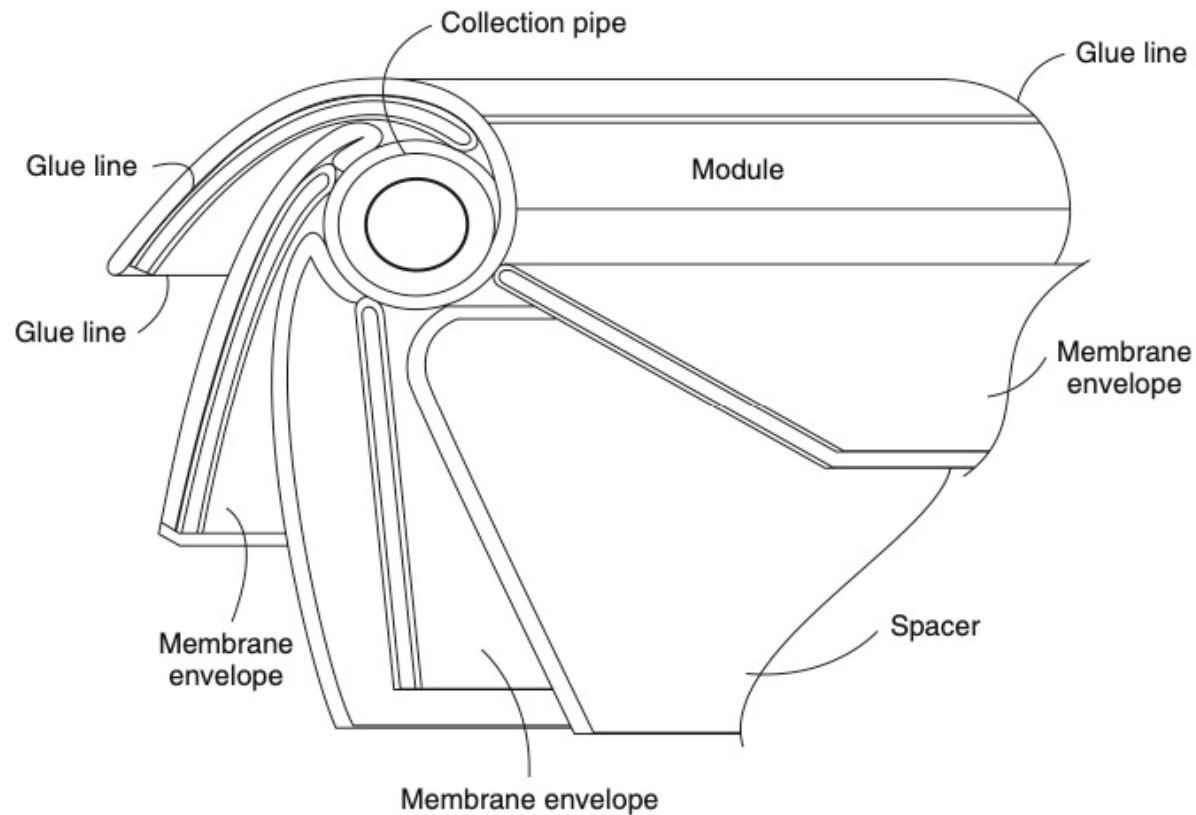


Figure 3.57 Multi-envelope spiral-wound module, used to avoid excessive pressure drops on the permeate side of the membrane. Large-diameter modules may have as many as 50 membrane envelopes, each with a membrane area of 1–2 m². Reprinted with permission from [147]. Copyright (1988) Taylor and Francis.

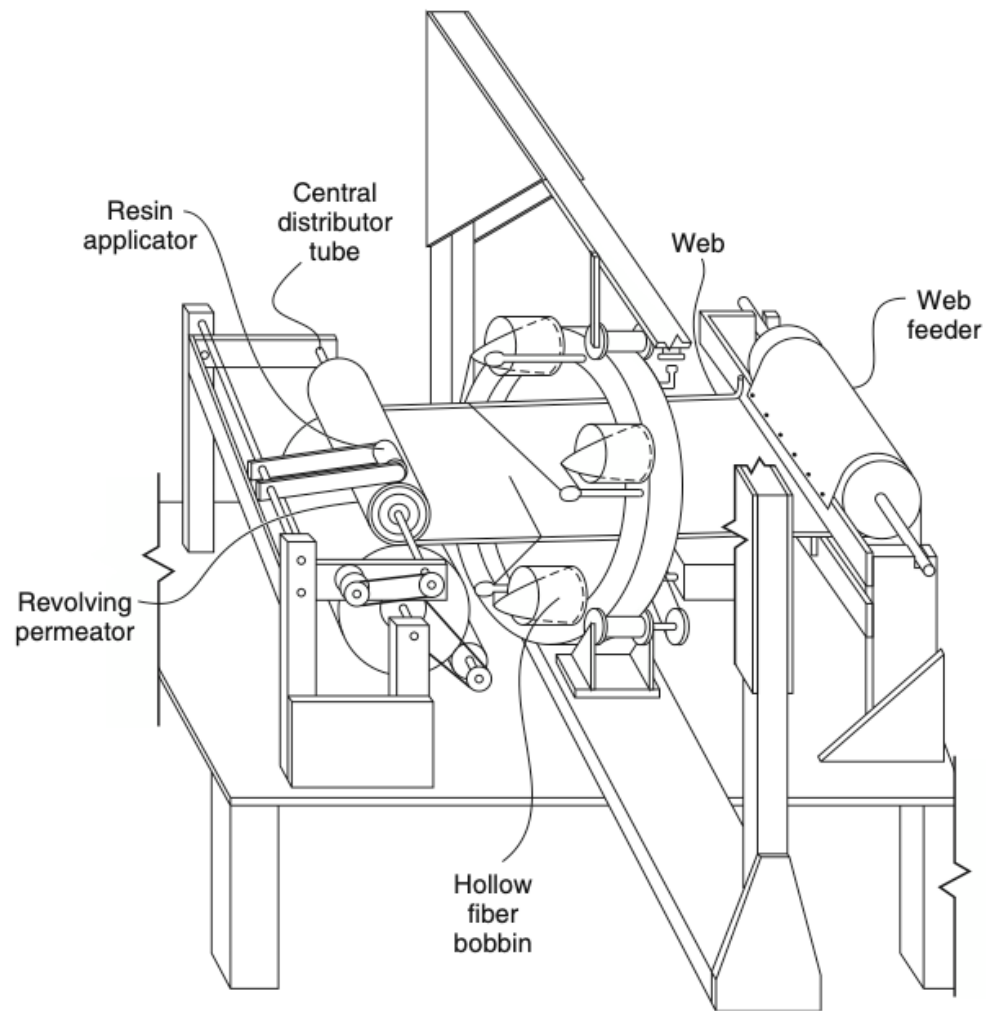


Figure 3.62 *Hollow fiber module winding apparatus from a 1972 Du Pont patent [159]. Machines of this general type are still used to produce hollow fiber modules*

Table 3.7 *Parameters for membrane module design*

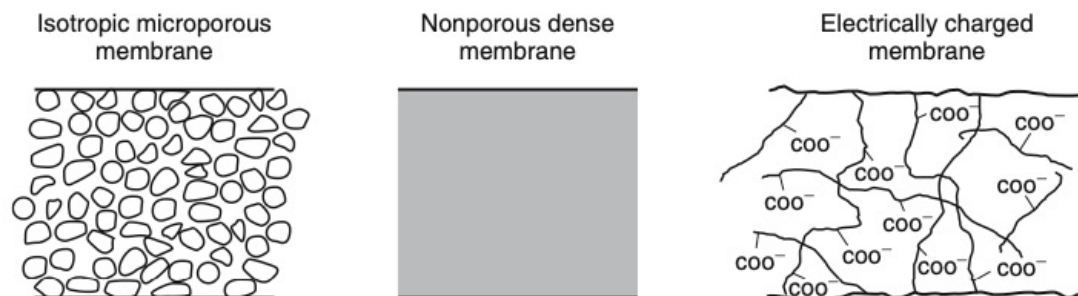
Parameter	Hollow fine fibers	Capillary fibers	Spiral-wound	Plate-and-frame	Tubular
Manufacturing cost (US\$/m ²)	5–20	10–50	5–100	50–200	50–200
Concentration polarization fouling control	Poor	Good	Moderate	Good	Very good
Permeate-side pressure drop	High	Moderate	Moderate	Low	Low
Suitability for high-pressure operation	Yes	No	Yes	Yes	Marginal
Limited to specific types of membrane material	Yes	Yes	No	No	No

Table 3.8 *Module designs most commonly used in the major membrane separation processes*

Application	Module type
Reverse osmosis: seawater	Spiral-wound modules dominate. Only one hollow fiber producer remains
Reverse osmosis: industrial and brackish water	Spiral-wound modules used almost exclusively; fine fibers too susceptible to scaling and fouling
Ultrafiltration	Tubular, capillary, and spiral-wound modules all used. Tubular generally limited to highly fouling feeds (automotive paint), spiral-wound to clean feeds (ultrapure water)
Gas separation	Hollow fibers for high volume applications with low flux, low selectivity membranes in which concentration polarization is easily controlled (nitrogen from air) Spiral-wound when fluxes are higher, feed gases more contaminated, and concentration polarization a problem (natural gas separations, vapor permeation)
Pervaporation	Most pervaporation systems are small so plate-and-frame systems were used in the first systems. Spiral-wound and capillary modules being introduced

Polymer Membranes

Symmetrical Membranes



Anisotropic Membranes

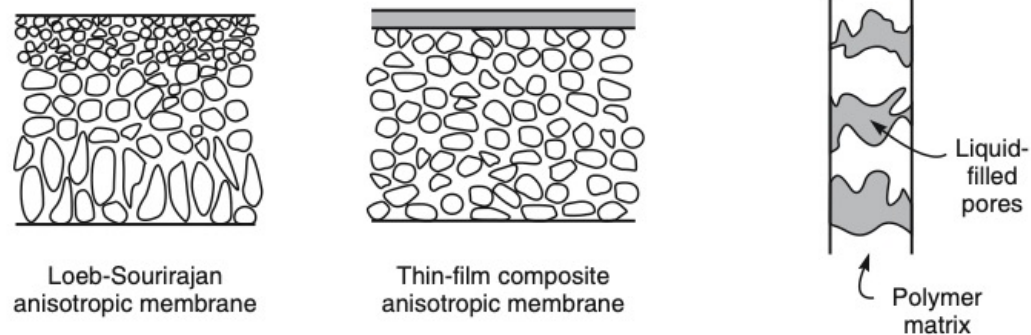


Figure 1.2 Schematic diagrams of the principal types of membranes

Porous Membranes

- high density of similar-sized short pores
- mechanical stability
- high size selectivity and a high flux

Integral-asymmetric isoporous membranes with a rather thin selective layer, supported by an open porous substructure

nonsolvent-induced phase separation (NIPS), also known as “phase-inversion process”

Loeb-Sourirajan cellulosic membranes

- pore sizes from a few nanometers up to a few tens of nanometers,
- self-assembling block copolymers

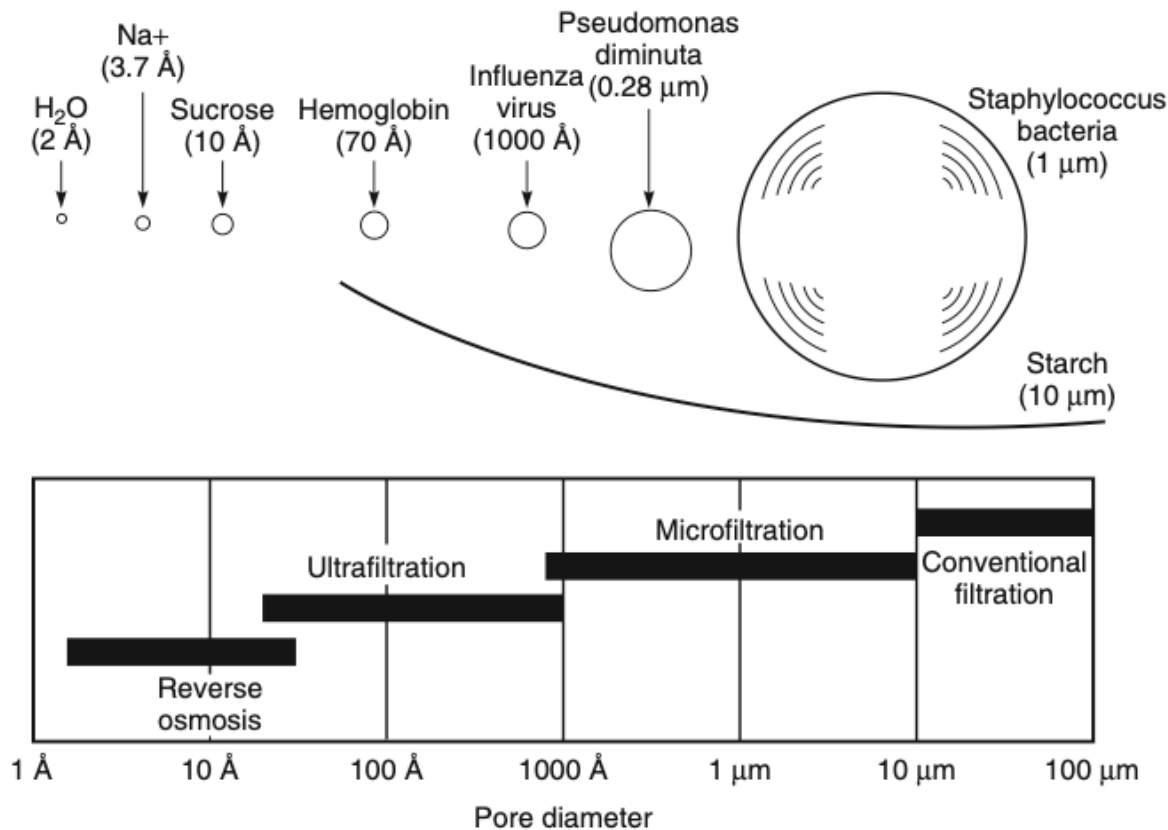


Figure 1.3 Reverse osmosis, ultrafiltration, microfiltration, and conventional filtration are related processes differing principally in the average pore diameter of the membrane filter. Reverse osmosis membranes are so dense that discrete pores do not exist; transport occurs via statistically distributed free volume areas. The relative size of different solutes removed by each class of membrane is illustrated in this schematic

Polymer Membranes

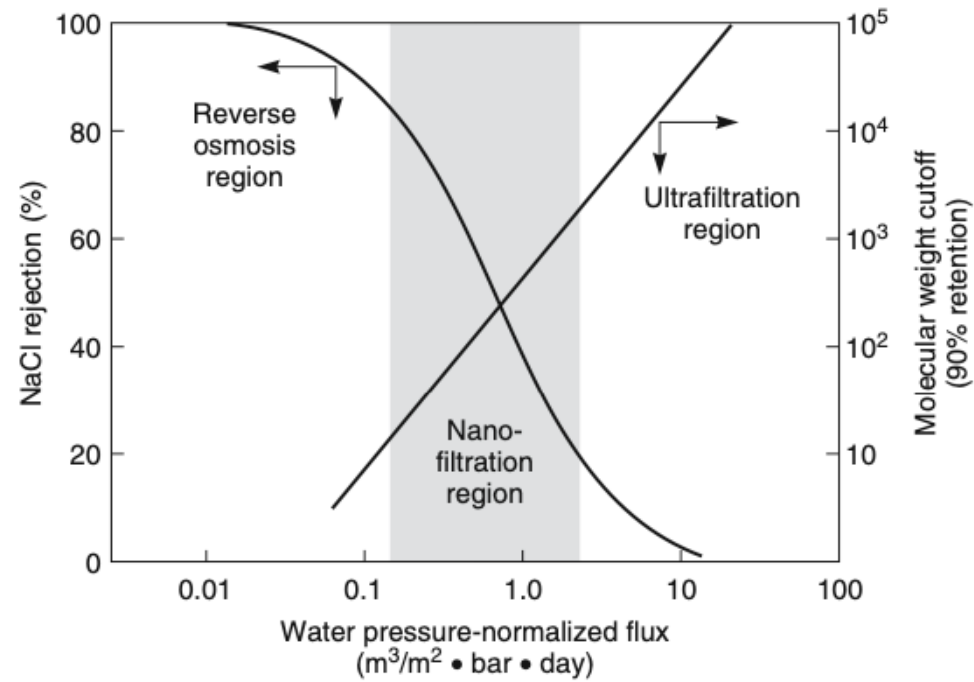


Figure 2.47 Diagram of the region of nanofiltration membrane performance relative to reverse osmosis and ultrafiltration membranes [81]

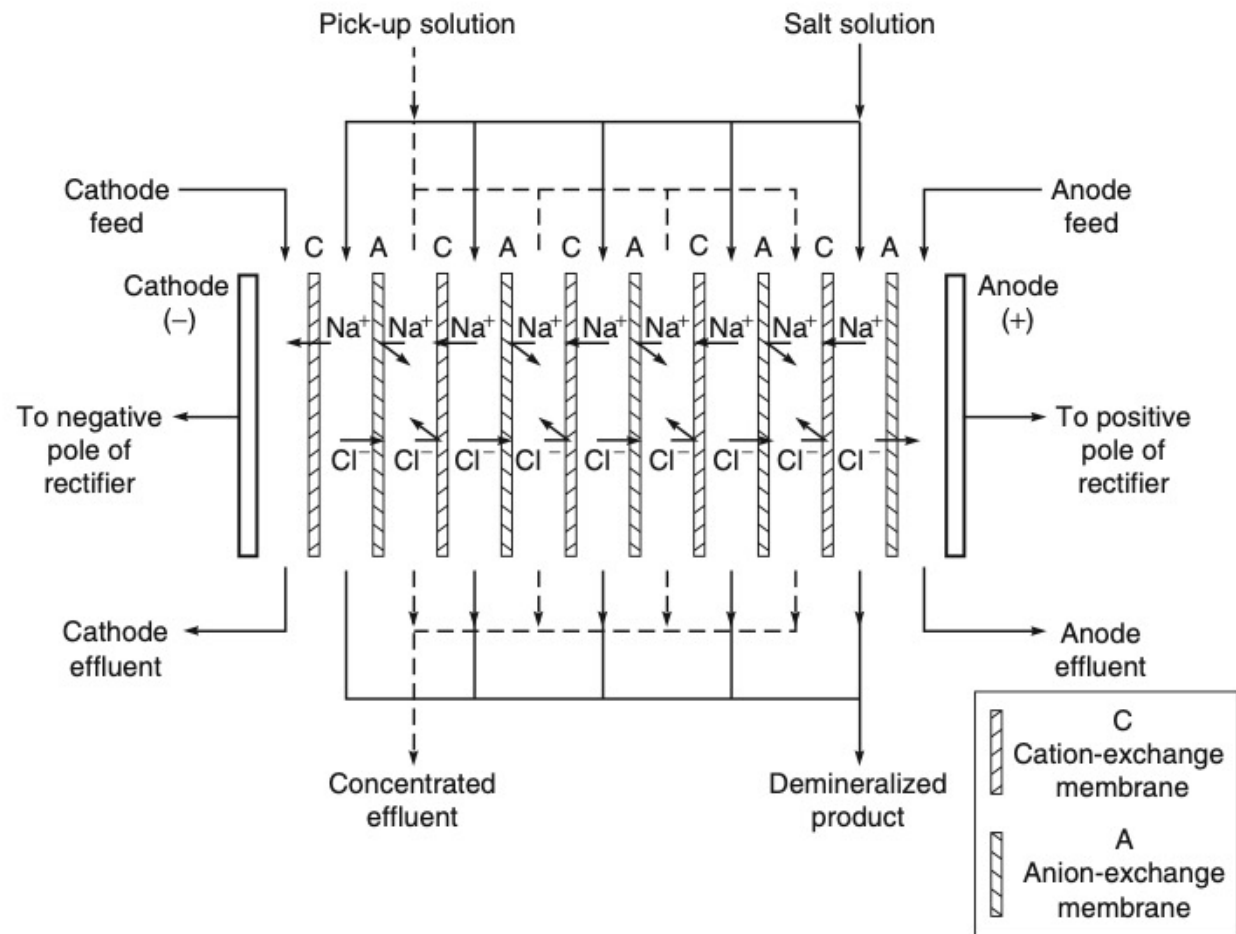


Figure 1.4 Schematic diagram of an electrodialysis process

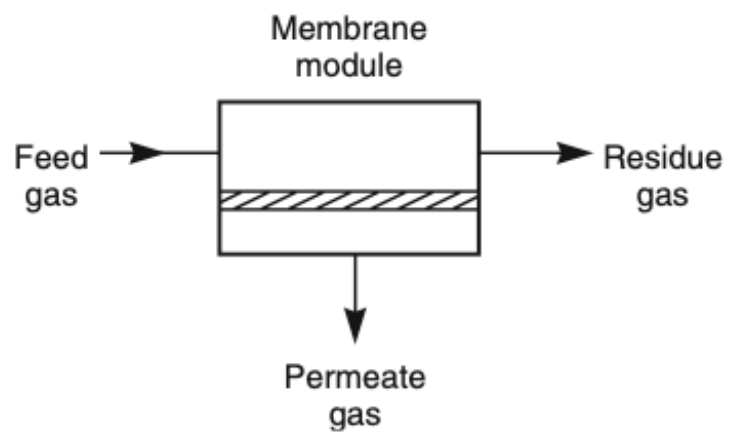
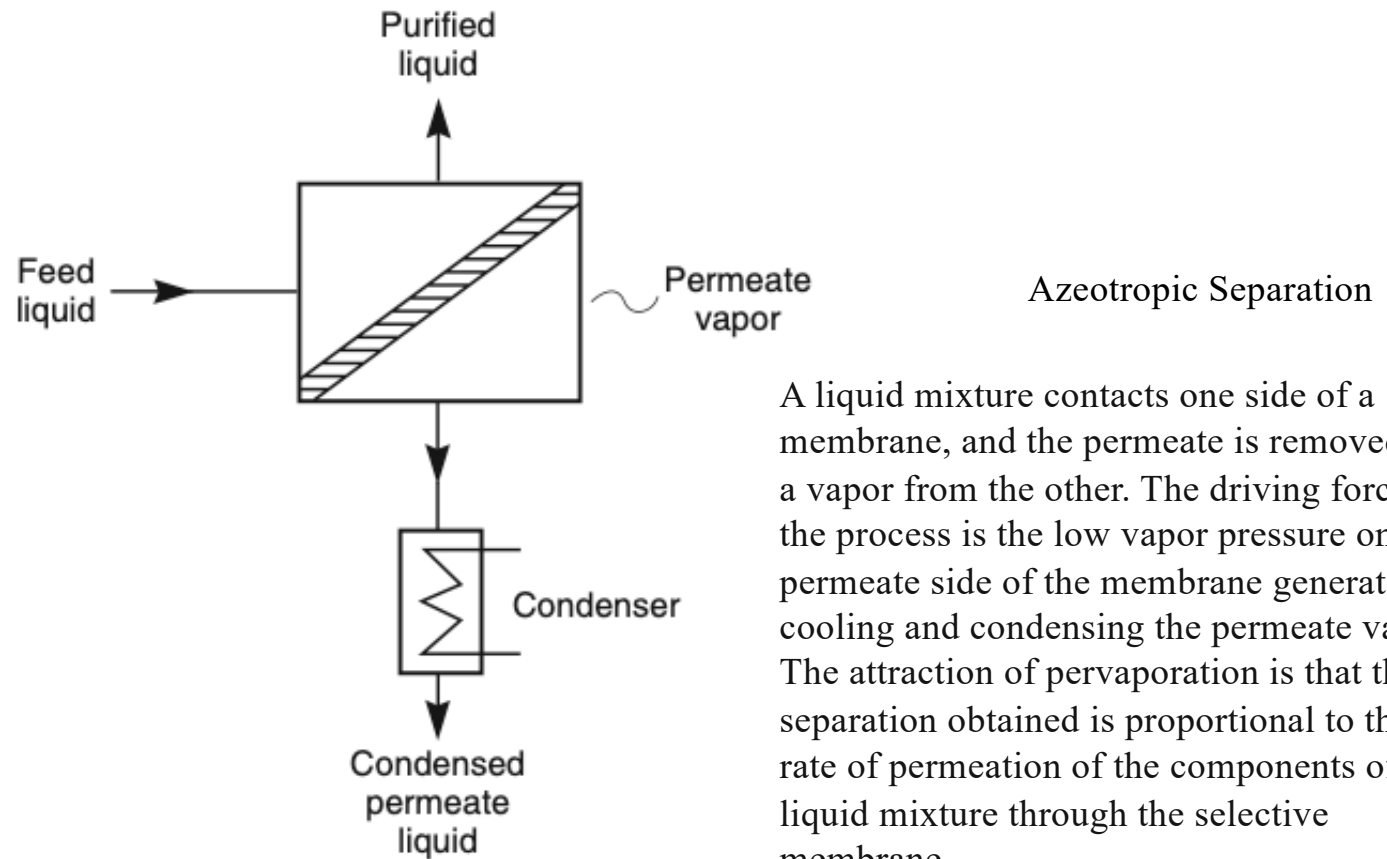


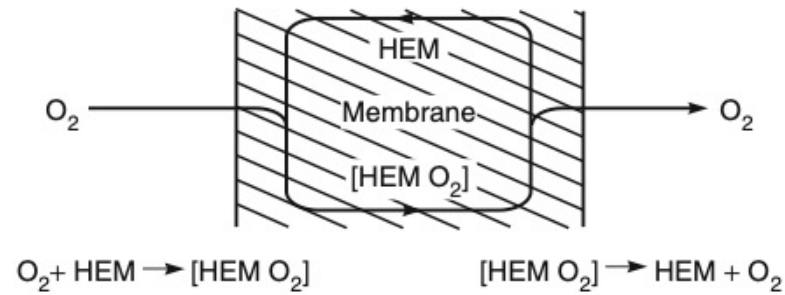
Figure 1.5 *Schematic diagram of the basic membrane gas separation process*



A liquid mixture contacts one side of a membrane, and the permeate is removed as a vapor from the other. The driving force for the process is the low vapor pressure on the permeate side of the membrane generated by cooling and condensing the permeate vapor. The attraction of pervaporation is that the separation obtained is proportional to the rate of permeation of the components of the liquid mixture through the selective membrane.

Figure 1.6 Schematic diagram of the basic pervaporation process

Facilitated transport



Coupled transport

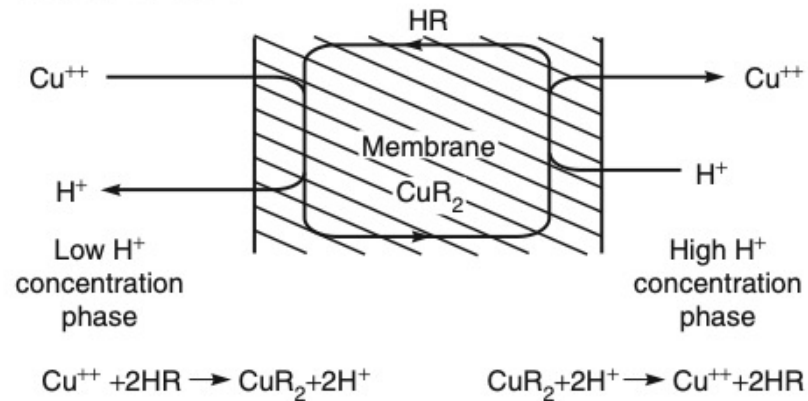


Figure 1.7 Schematic examples of carrier facilitated transport of gas and ions. The gas transport example shows the transport of oxygen across a membrane using hemoglobin dissolved in water as the carrier agent. The ion transport example shows the transport of copper ions across a membrane using a liquid ion exchange reagent dissolved in a water immiscible solvent as the carrier agent

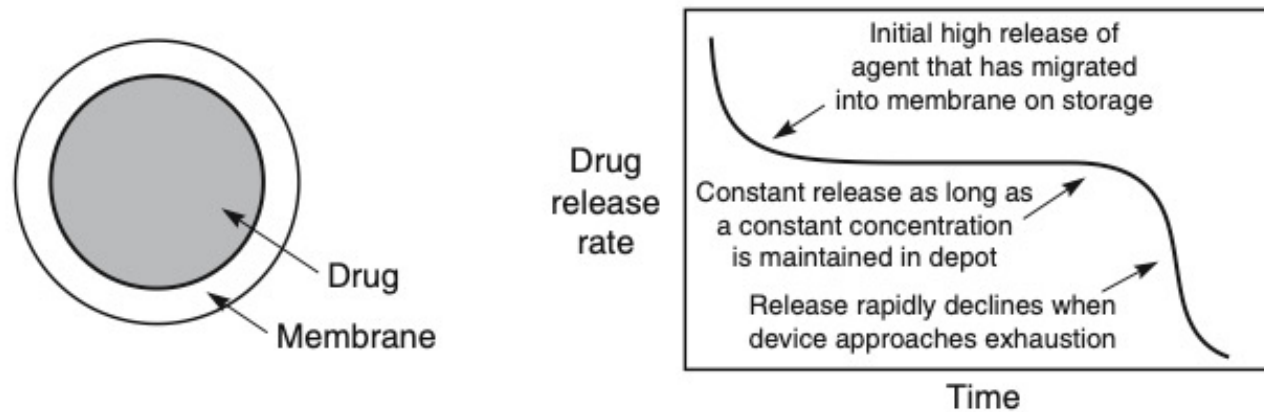


Diagram and release curve for a simple reservoir system

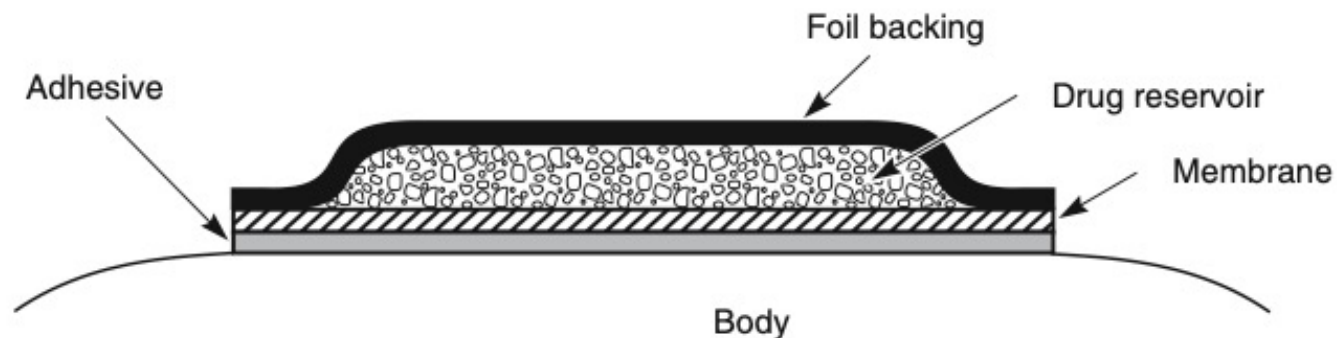


Figure 1.9 Schematic of transdermal patch in which the rate of delivery of drug to the body is controlled by a polymer membrane. Such patches are used to deliver many drugs including nitroglycerine, estradiol, nicotine, and scopolamine

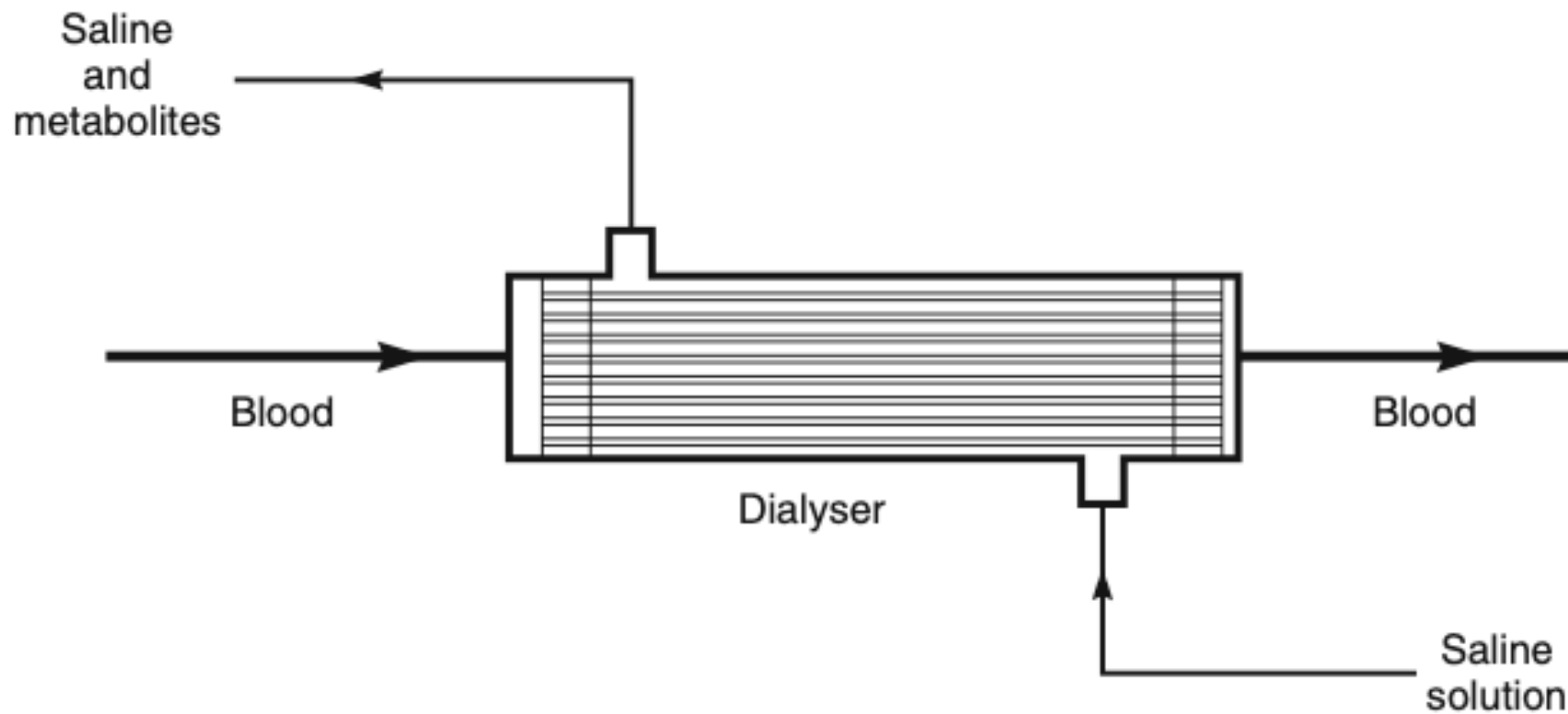


Figure 1.8 Schematic of a hollow fiber artificial kidney dialyzer used to remove urea and other toxic metabolites from blood. About 100 million of these devices are used every year

Types of Membranes:

polymer, ceramic, metal, or combinations

flat sheet or also spiral wound, as well as tubular, hollow fiber, nanofibrous membranes

structure of their cross-section, which can be symmetric or asymmetric. separation properties.

separation layer can be dense or porous on different length scales.

nanometer-sized pores are categorized into micropores (<2 nm), mesopores ($\sim 2\text{--}50$ nm), and macropores (>50 nm).

Nanofiltration, ultrafiltration, and microfiltration membranes are characterized by pore-size ranges, which are approximately 1–10 nm, 1–100 nm, and 0.1–10 μm

Reverse-osmosis membranes for desalination and dense membranes for gas separation have “pore” sizes below ~ 1 nm

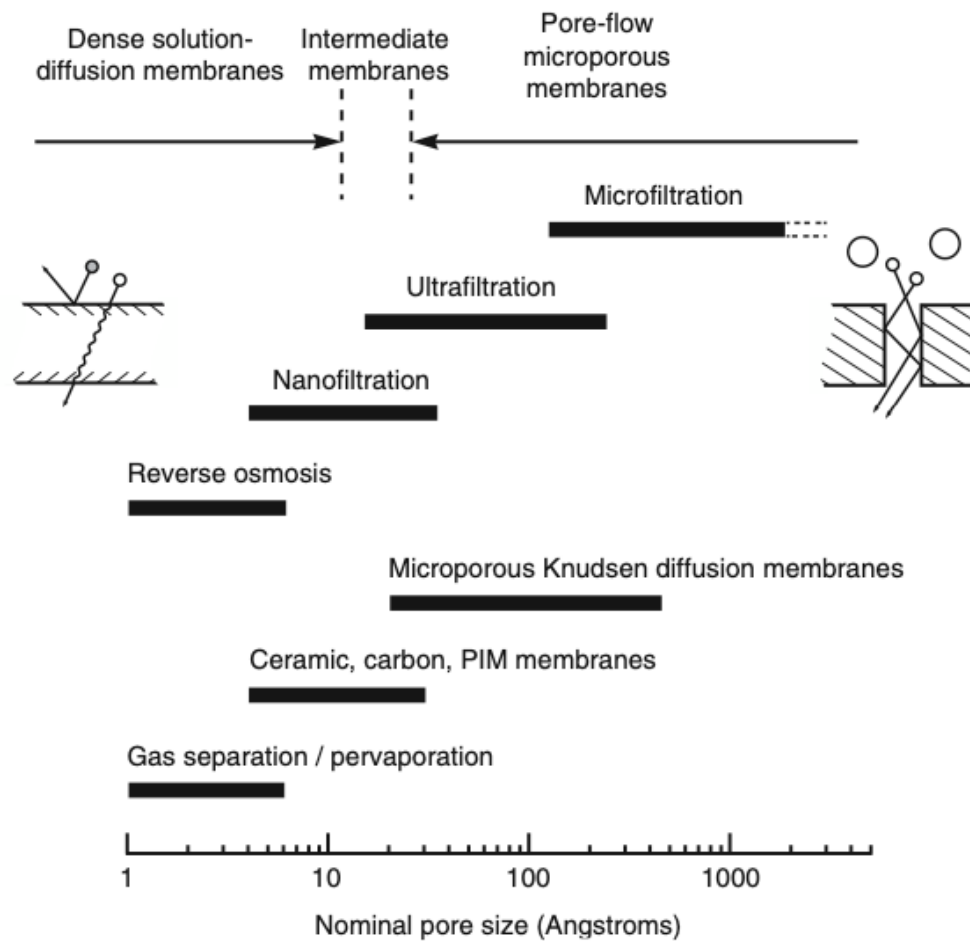
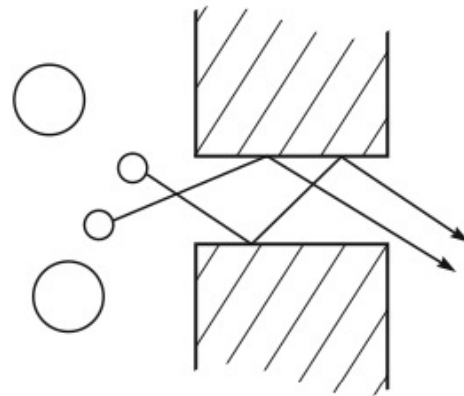
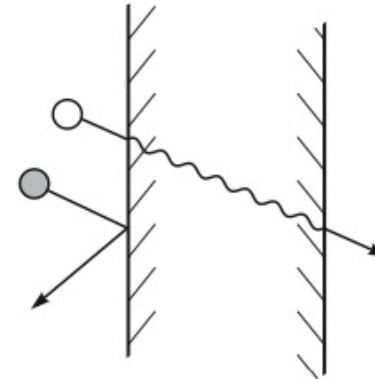


Figure 2.2 Schematic representation of the nominal pore size and best theoretical model for the principal membrane separation processes



Microporous membranes separate by molecular filtration



Dense solution-diffusion membranes separate because of differences in the solubility and mobility of permeants dissolved in the membrane material

Figure 2.1 Molecular transport through membranes can be described by a flow through permanent pores or by the solution-diffusion mechanism

Darcy's Law
Flow through sand

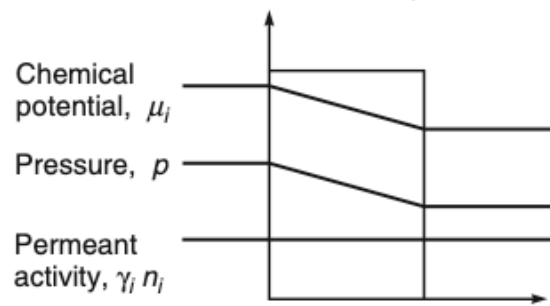
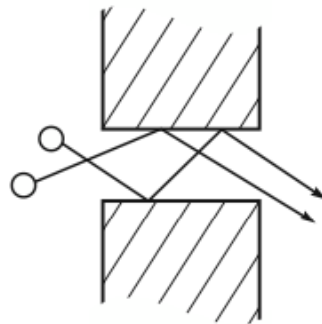
$$J_i = K' c_i \frac{dp}{dx}$$

$$Q = \frac{kA}{\mu L} \Delta p$$

$$J_i = -D_i \frac{dc_i}{dx}$$

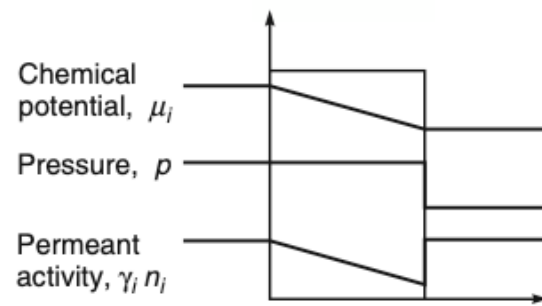
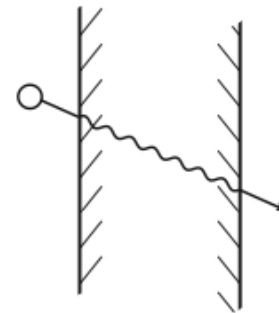
Fick's Law
Brownian diffusion

Microporous membranes
separate by molecular
filtration



(a)

Dense solution-diffusion
membranes separate because
of differences in the solubility
and mobility of permeants
in the membrane material



(b)

Figure 2.6 A comparison of the driving force gradients acting on a one-component solution permeating (a) a pore-flow and (b) a solution-diffusion membrane

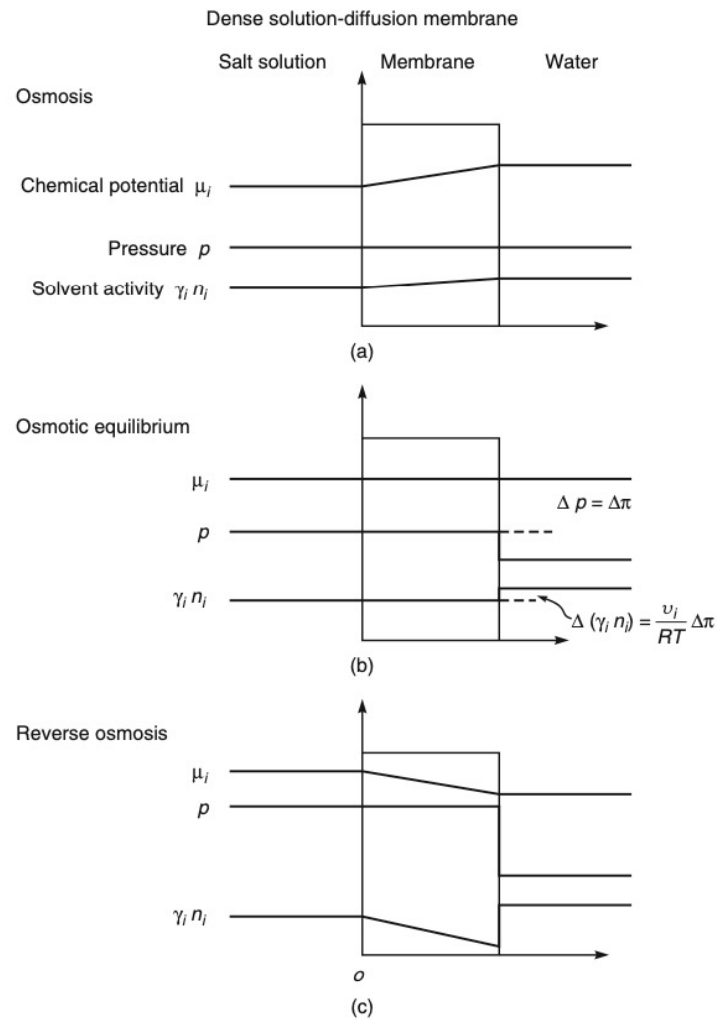


Figure 2.7 Chemical potential, pressure, and solvent gradients in an osmotic membrane following the solution-diffusion model for (a) osmosis, (b) osmotic equilibrium and (c) reverse osmosis. The pressure in the membrane is uniform and equal to the high-pressure value, so the chemical potential gradient within the membrane is expressed as a concentration gradient

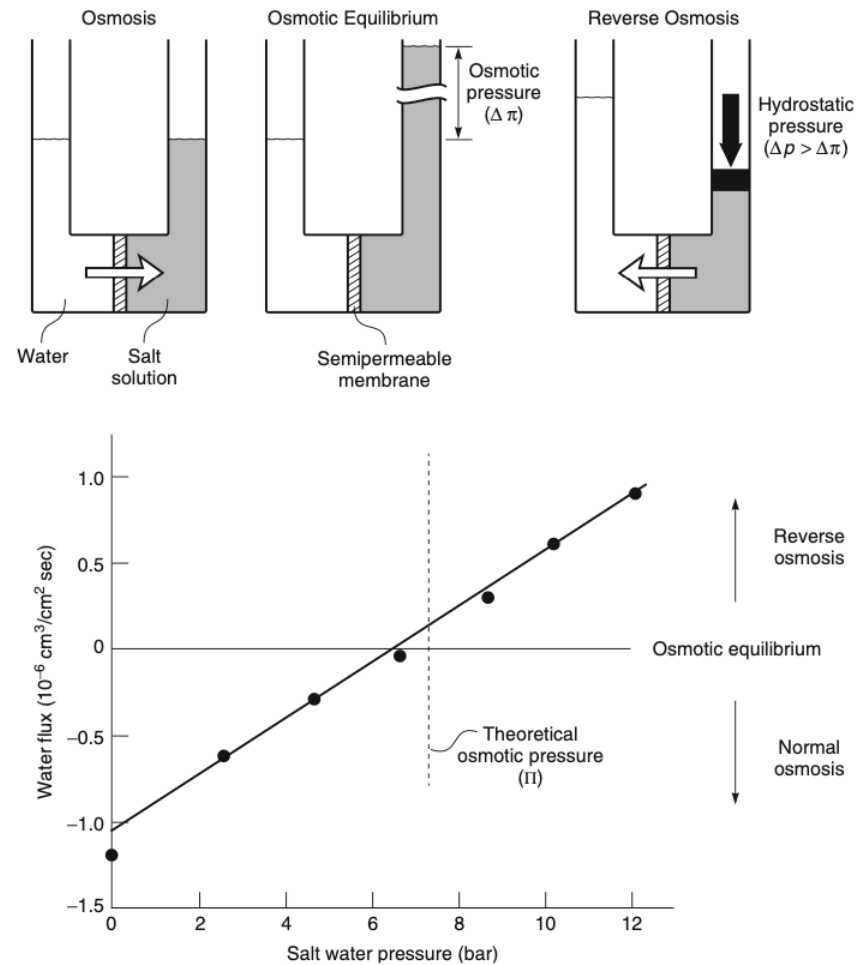


Figure 2.9 An illustration of the relationship between osmosis, osmotic equilibrium, and reverse osmosis. The data shown are from a paper by Thorsen and Holt [17] using a cellulose acetate membrane. Because the membrane is not perfectly selective for salt, the point of osmotic equilibrium (no flow across the membrane) is slightly below the theoretical osmotic pressure

- Ultrafiltration, microfiltration, and microporous Knudsen diffusion gas separation membranes are all clearly microporous. They all contain pores larger than 10–15 Å in diameter and transport occurs by pore flow.
- Reverse osmosis, pervaporation, and polymeric gas separation membranes contain a dense selective polymer layer with no visible pores. These membranes show different transport rates for molecules as small as 2–5 Å in diameter. The fluxes of permeants through these membranes are also much lower than through microporous membranes. Transport in these membranes is best described by the solution-diffusion model. The spaces between polymer chains in these membranes are less than 5–10 Å in diameter and so are within the normal range of thermal motion of the polymer chains that make up the membrane matrix. Molecules permeate the membrane through free volume elements between polymer chains that are transient on the time scale of the diffusion processes occurring.
- Membranes in the third group contain pores with diameters between 5 and 15 Å and are intermediate between truly microporous and truly solution-diffusion membranes. For example, nanofiltration membranes are intermediate between ultrafiltration membranes – clearly microporous – and reverse osmosis membranes – clearly dense films. Nanofiltration membranes have high rejections for the di- and trisaccharides, sucrose and raffinose, with molecular diameters of 10–13 Å, but freely pass the monosaccharide fructose with a molecular diameter of about 5–6 Å. Some gas separation membranes also fall into this intermediate category. If gas separation membranes are made from polymers with extremely stiff polymer chains, the molecular motion of the polymer can be so restricted that semi-permanent microcavities form. These cavities or free volume elements have diameters of 5–15 Å and appear to be connected, forming relatively long continuous pathways through the membranes. These polymers are called polymers with intrinsic microporosity (PIM) [8–10]. Some finely porous ceramic membranes or carbonized polymer membranes also fall into this intermediate range.

Jump Diffusion Model

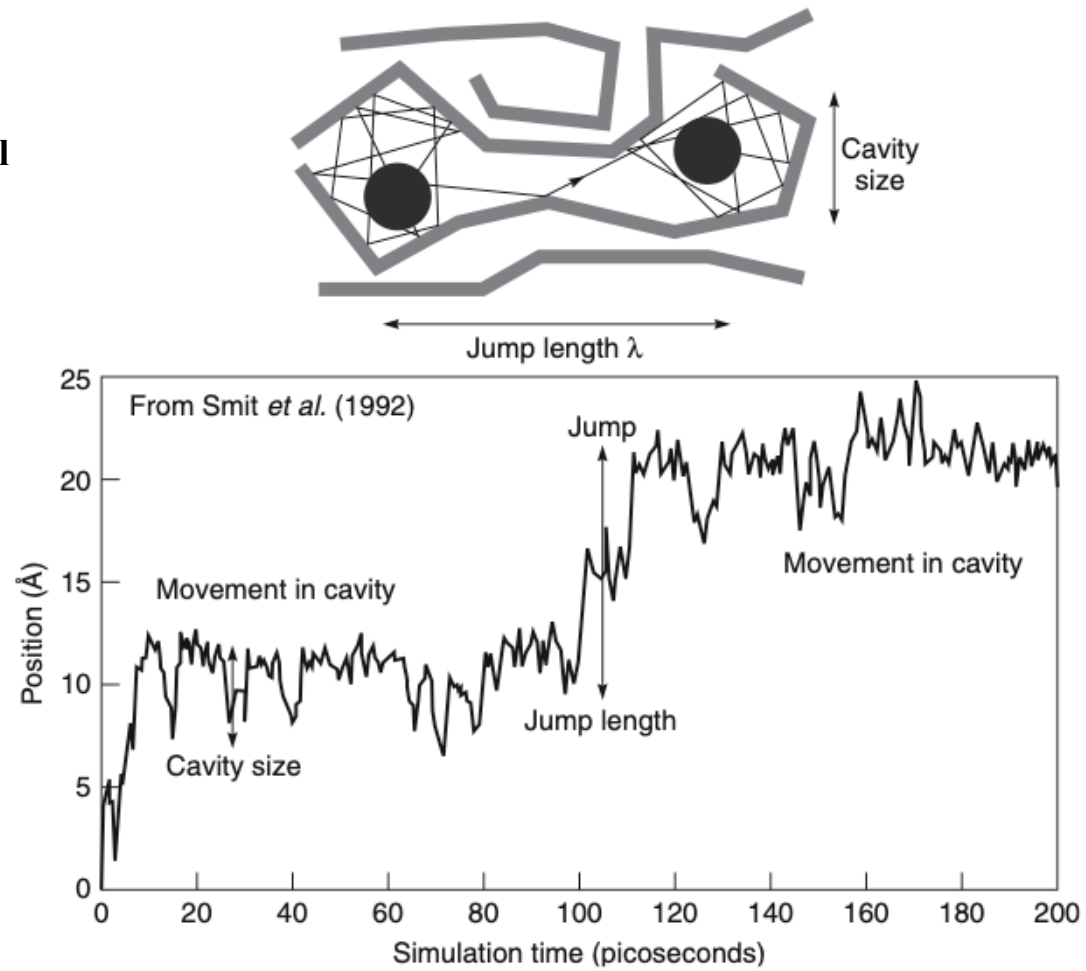


Figure 2.3 Motion of a carbon dioxide molecule in a 6FDA-4PDA polymer matrix. Reprinted with permission from [11]. Copyright (1992) Elsevier.

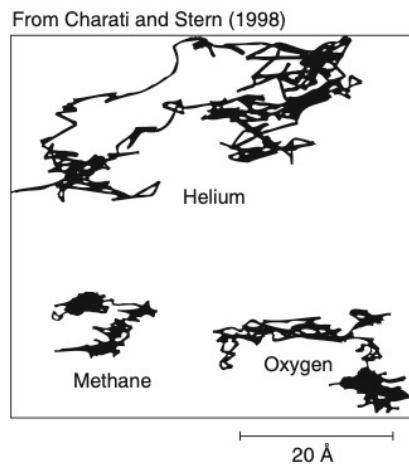


Figure 2.4 Simulated trajectories of helium, oxygen, and methane molecules during a 200-ps time period in a poly(dimethylsiloxane) matrix. Reprinted with permission from [12] Copyright (1998) American Chemical Society.

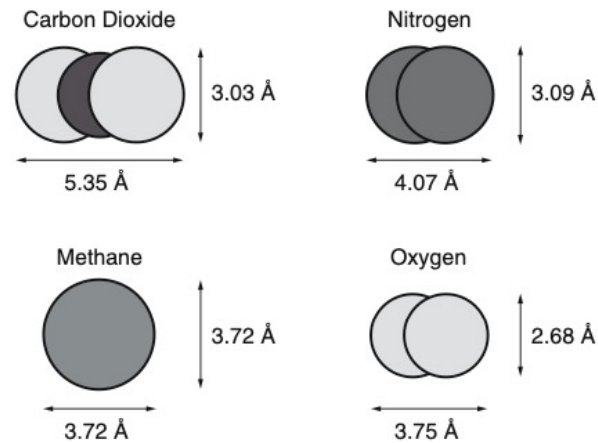


Figure 2.5 Illustration showing the approximate molecular dimensions of CO_2 , CH_4 , N_2 , and O_2 . Shape and size both influence permeant diffusion

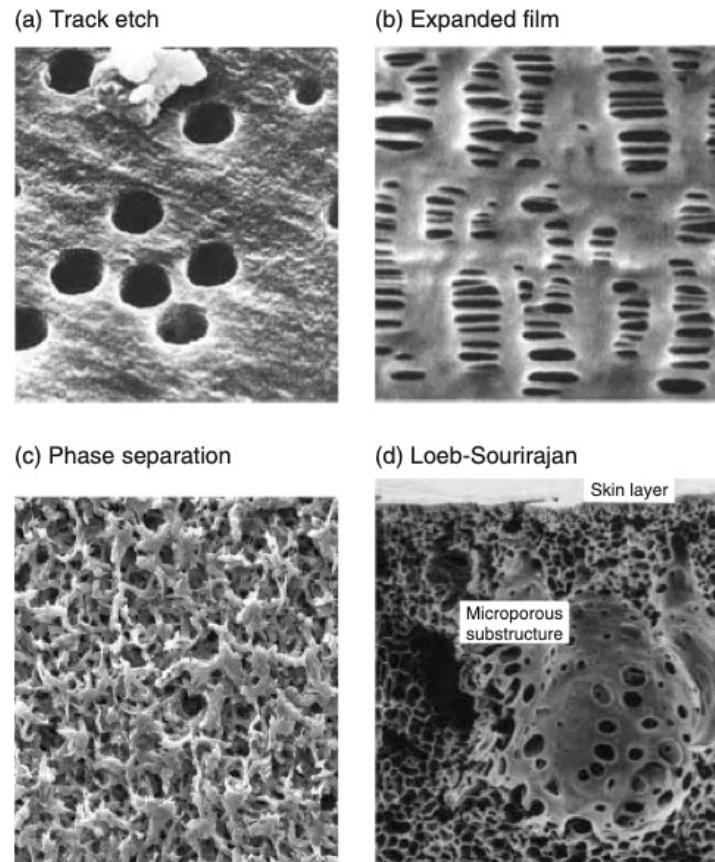


Figure 2.31 Scanning electron micrographs at approximately the same magnification of four microporous membranes having approximately the same particle retention. (a) Nuclepore (polycarbonate) nucleation track membrane. (b) Celgard® (polyethylene) expanded film membrane. (c) Millipore cellulose acetate/cellulose nitrate phase separation membrane made by water vapor imbibition. (d) Anisotropic symmetric polysulfone membrane made by the Loeb-Sourirajan phase separation process. Reprinted with permission of Millipore Corporation, Billerica, MA

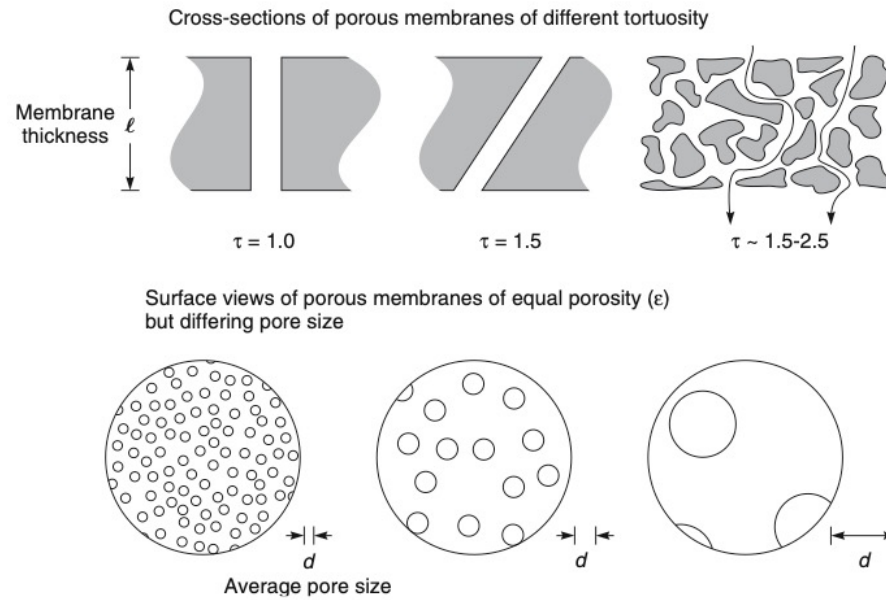


Figure 2.32 Microporous membranes are characterized by their tortuosity (τ), their porosity (ϵ), and their average pore diameter (d)

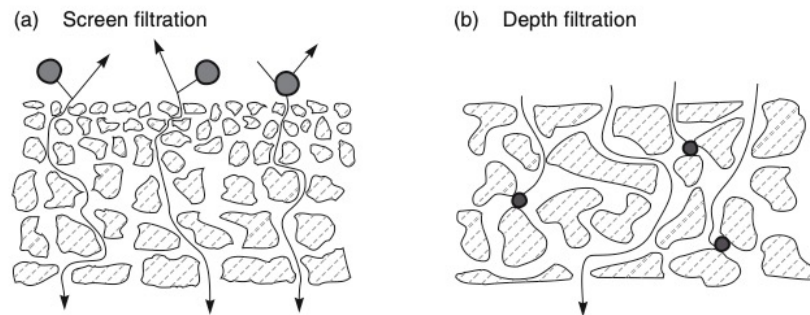


Figure 2.33 Separation of particulates can take place (a) at the membrane surface according to a screen filtration mechanism or (b) in the interior of the membrane by a capture mechanism as in depth filtration

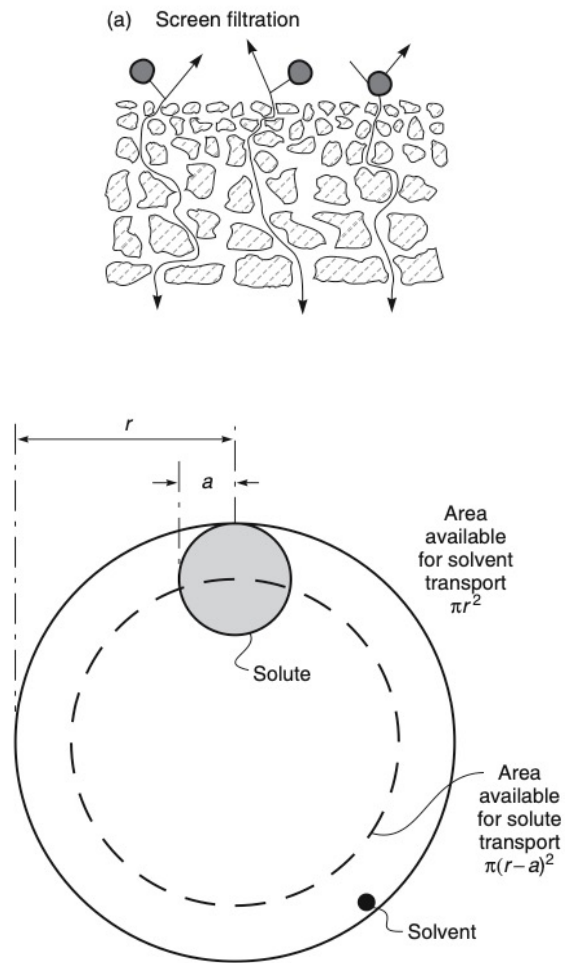


Figure 2.34 Illustration of the Ferry mechanical exclusion model of solute transport in small pores

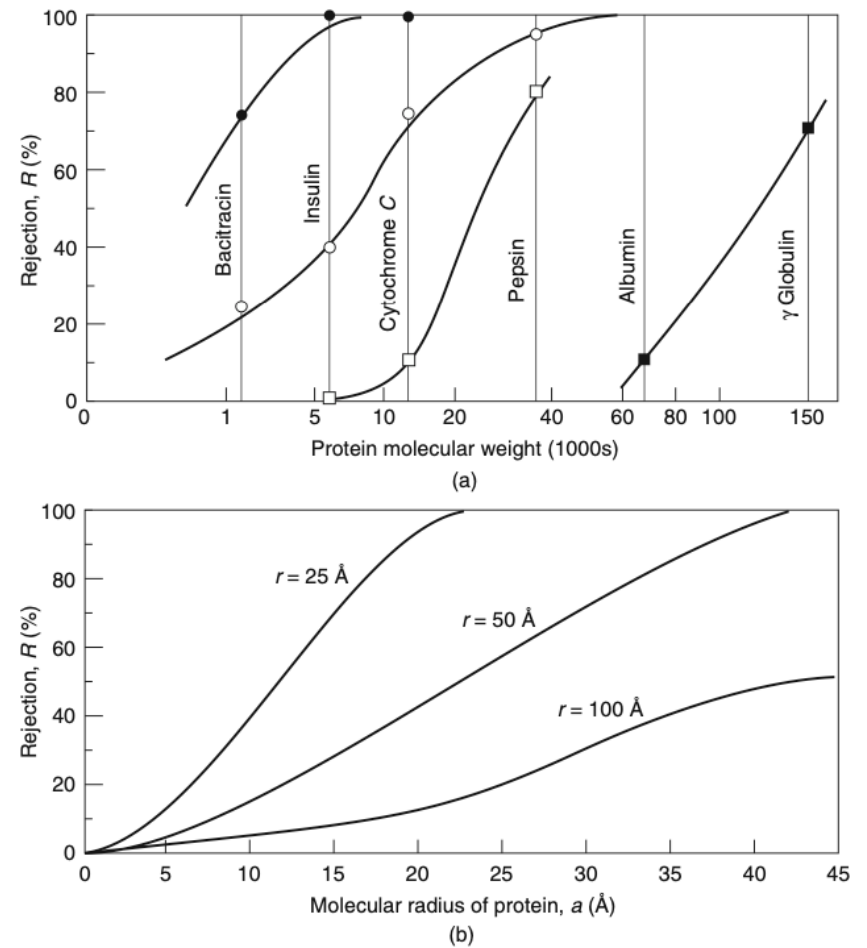


Figure 2.35 (a) Rejection of globular proteins by ultrafiltration membranes of increasing pore size and (b) calculated rejection curves from the Ferry-Renkin Equation 2.120 plotted on the same scale [62]

(b) Depth filtration

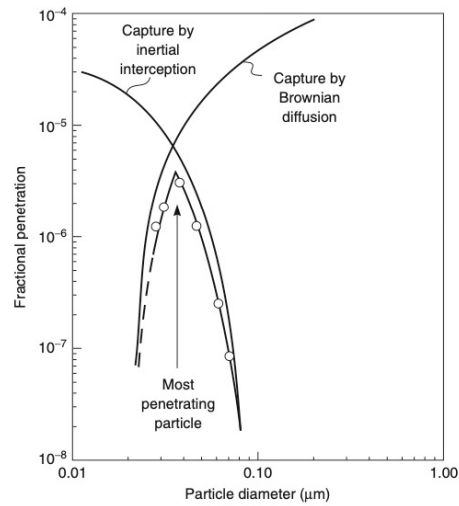
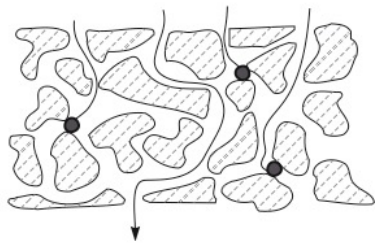


Figure 2.37 Gas-borne particle penetration through an ultrathin PVDF (poly(vinylidene fluoride)) membrane [65, 66]

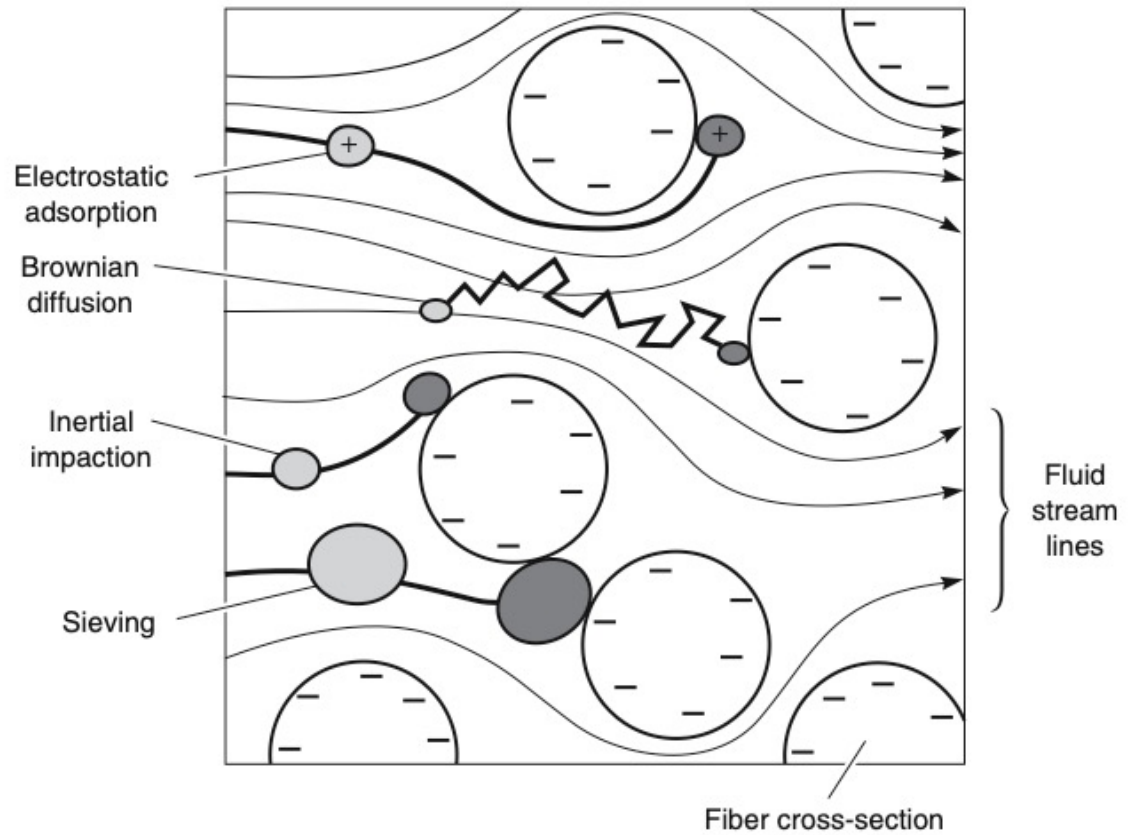


Figure 2.36 Particle capture mechanism in filtration of liquid solutions by depth microfilters. Four capture mechanisms are shown: simple sieving; electrostatic adsorption; inertial impaction; and Brownian diffusion

Gas separation membranes

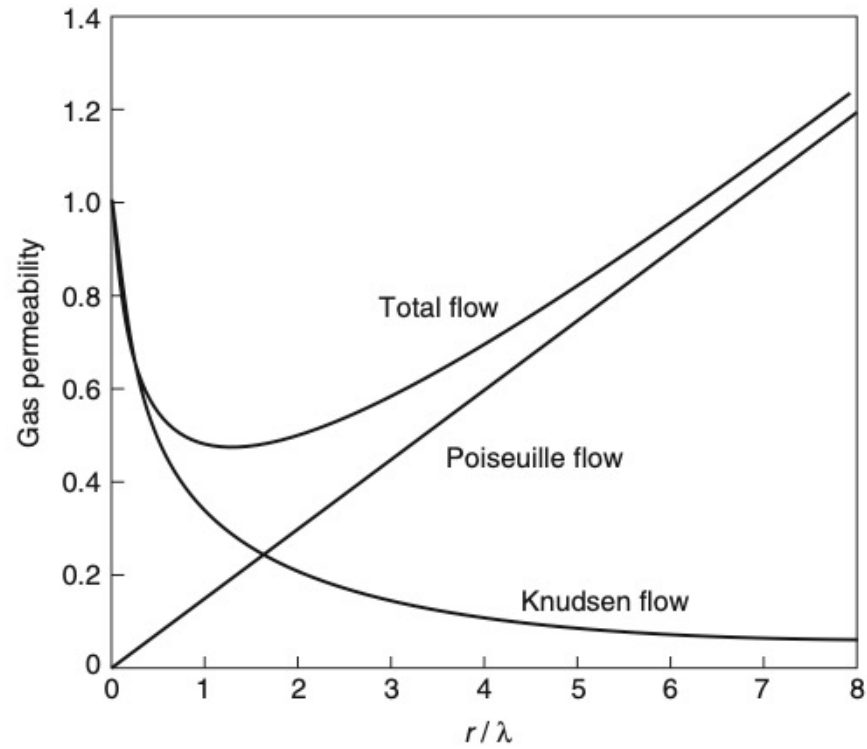


Figure 2.38 Illustration of the properties of Knudsen to Poiseuille flow in a finely microporous membrane as a function of the pore radius (r) divided by the mean pore path (λ) of the gas (after Barrer) [67]

Gas separation membranes

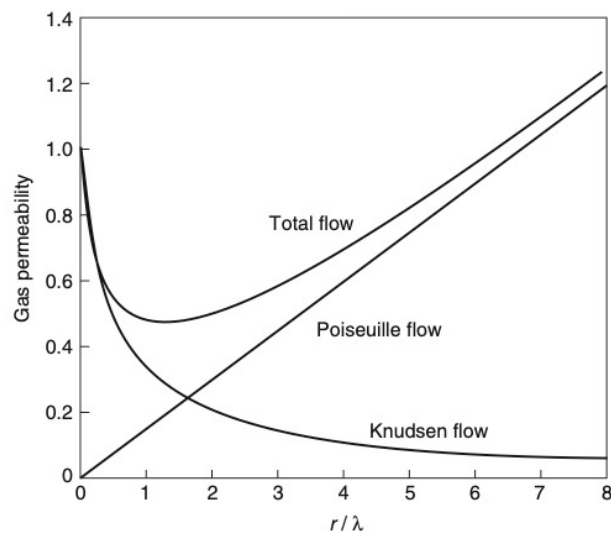
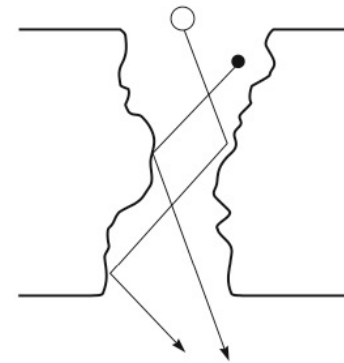
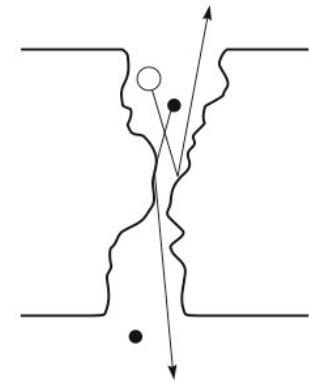


Figure 2.38 Illustration of the properties of Knudsen to Poiseuille flow in a finely microporous membrane as a function of the pore radius (r) divided by the mean pore path (λ) of the gas (after Barrer) [67]

Mixtures of noncondensable gases

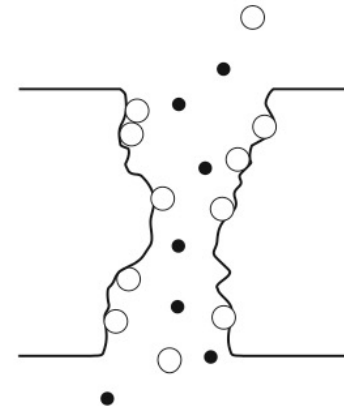


(a) Knudsen diffusion

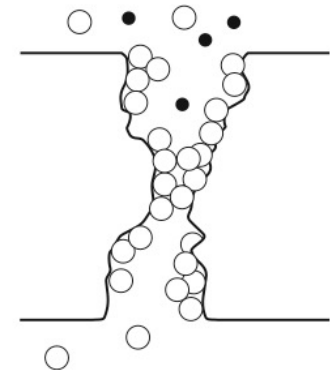


(b) Molecular sieving

Mixtures of condensable and noncondensable gases



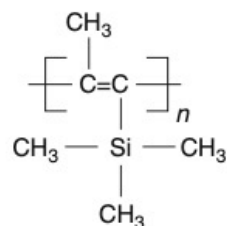
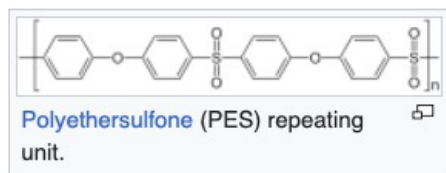
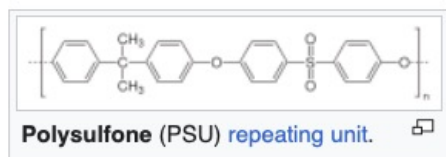
(c) Knudsen diffusion and surface diffusion



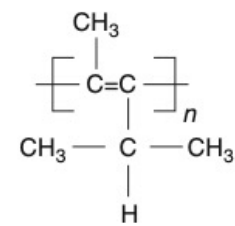
(d) Surface diffusion and capillary condensation

Figure 2.41 Permeation of noncondensable and condensable gas mixtures through finely microporous membranes. With noncondensable gases, molecular sieving occurs when the pore wall reaches the 5- to 10-Å diameter range. With gas mixtures containing condensable gases, surface diffusion increases as the pore diameter decreases and the temperature decreases (increasing adsorption)

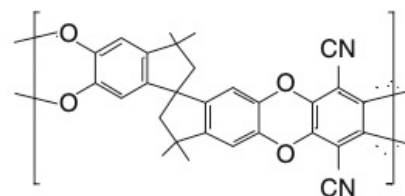
Gas separation membranes



Poly(1-trimethylsilyl-1-propyne)
[PTMSP]



Poly(4-methyl-2-pentyne)
[PMP]



Polybenzodioxane (PIM-1)

Figure 2.44 Structure of three exceptionally high free volume polymers. Extremely stiff-backed, rigid polymer chains pack poorly, leading to high fractional free volumes

Table 2.9 A comparison of the properties of two polymers with intrinsic microporosity (PTMSP and PIM-1) with a high free volume conventional glassy polymer (polysulfone) [77–79]

Polymer	Free volume (%)	BET surface area (m ² /g)	N ₂ permeability (Barrer)	Selectivity O ₂ /N ₂
PTMSP	29	550	6300	1.5
PIM-1	25	830	340	3.8
Polysulfone	18	<1	0.25	5.6

Important and challenging topics for gas separation membrane production

Solvent evaporation from homopolymer mixtures,
Solvent annealing of copolymer films,
Directing the orientation of membrane pores by electric fields,
Polymerization-induced phase-separation (PIPS),
 or polymerization-induced self-assembly (PISA)
Functionalization of membrane pores and
Molecular transport on the atomic scale in the membranes

Block Co-polymer Membranes

cylindrical, gyroidal, or lamellar pore

Cast a block copolymer solution onto a substrate and evaporate the solvent sufficiently fast to achieve alignment of the microdomains in the perpendicular direction.

An electric field can be applied to align, e.g., cylindrical domains.

The pore-forming block is etched away to obtain open pores, the film is transferred from the solid substrate onto a porous support

Isoporous top layer on a more open porous sublayer of the same material.

These membranes can be prepared directly on a porous nonwoven support

Early on, it has been recognized that two distinct sets of factors dictate the membrane structure:

- (i) the equilibrium thermodynamics of the multicomponent system and
- (ii) the processing conditions as quantified, e.g., by the magnitude of the overall material transfer between film and bath during coagulation

$$\frac{\Delta F(\phi_P)}{\rho V k_B T} = \frac{\phi_P \ln \phi_P}{N} + \phi_N \ln \phi_N + \chi_{PN} \phi_P \phi_N$$

with $\phi_P + \phi_N = 1$

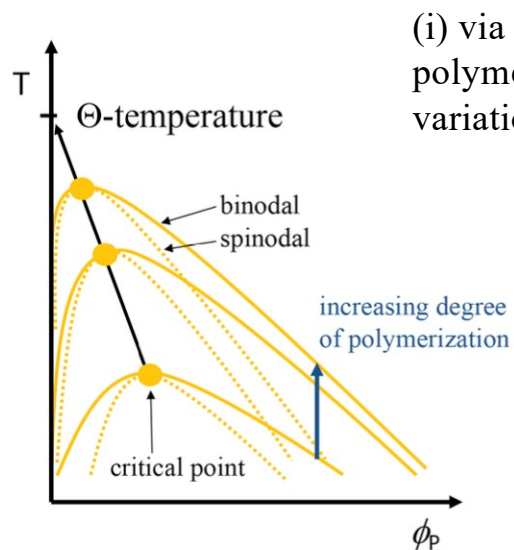


Figure 1. Sketch of the phase diagram of a polymer–solvent mixture with an upper critical solution temperature (UCST), for different degrees of polymerization, N . Binodals (solid lines) denote the densities of the coexisting, polymer-rich, and solvent-rich phases, whereas (mean-field) spinodals (dotted lines) indicate the stability limits of the homogeneous polymer-rich and solvent-rich domains.

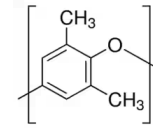
(i) via a change of temperature (or effective polymer interaction, $\chi < 0$) or (ii) by a variation of the polymer density, ϕ_P

$$\chi_{PN}^c = \frac{1}{2} (1 + 1/\sqrt{N})^2$$

$$\phi_P^c = 1/(1 + \sqrt{N})$$

Case (i) corresponds to thermally induced phase separation (TIPS). This method is mainly used to produce membranes from polymers that are difficult to dissolve and soluble only at elevated temperatures, like polyolefins such as, e.g., polypropylene, polyethylene, or poly(vinylidene fluoride) (PVDF). The phase separation upon cooling is coupled with crystallization in the case of these polymers.

TIPS can also be applied to other polymers such as polystyrene and poly(2,5-dimethyl-1,4-phenylene ether), when dissolved in cyclohexanol.



A special type of TIPS was observed for a solution of PVDF with cellulose acetate in a mixture of a good solvent (dimethylformamide) and a nonsolvent (nonane).

The solvent–nonsolvent mixture itself shows an upper critical solution temperature below the temperature of the initial polymer solution.

Therefore, the solution phase separates upon cooling, resulting in a highly surface-porous polymer film, where the pore size is dictated by the length scale of spinodal decomposition.

The subsequent phase separation, which leads to an increase of the pore size with time, is then stopped by quenching the whole system in a cold coagulant.

Early on, it has been recognized that two distinct sets of factors dictate the membrane structure:

- (i) the equilibrium thermodynamics of the multicomponent system and
- (ii) the processing conditions as quantified, e.g., by the magnitude of the overall material transfer between film and bath during coagulation

(ii) corresponds, e.g., to the (slow) evaporation of a moderately poor solvent from an initially very dilute solution of collapsed coils. Then, upon decreasing the solvent density, the polymer precipitates when the binodal is crossed via the nucleation and growth of individual droplets of the polymer-rich phase.

Ternary Mixtures of Polymer, Solvent, and Nonsolvent. The phase diagram of an incompressible three-component system polymer, solvent, and nonsolvent or, equivalently, of a compressible, two-component system can already be complex. In fact, such a system may exhibit six qualitatively different types of phase diagrams according to the classification of van Konynenburg and Scott.

typical case

where one solvent is compatible with the polymer, whereas the Other nonsolvent is a poor solvent for the polymer; the two solvents, however, remain miscible in the range of thermodynamic conditions of interest.

An incompressible system is described by two thermodynamically independent order parameters, e.g., the normalized density, ϕ_p , of the polymer and the normalized density, ϕ_s , of the solvent because the densities of polymer, solvent, and nonsolvent add up to unity, $\phi_p + \phi_s + \phi_n = 1$

χ_{PN} or χ_{AB}

Insoluble

$$\chi_{\text{eff}} \sim (1 - \phi_S)$$

Soluble

$$\chi_{\text{PN}}(\phi_S) \sim (1 - \phi_S)^{(1 + \nu_{\text{SAW}}\omega_{12}) / (3\nu_{\text{SAW}} - 1)} \approx (1 - \phi_S)^{0.616}$$

where $\nu_{\text{SAW}} = 0.588$ is the scaling exponent of the extension of a self-avoiding random walk and $\omega_{12} \approx 0.4$ denotes the correction-to-scaling exponent that characterizes the contacts of two mutually interdigitating self-avoiding walks. Within this effective

$$\begin{aligned} \frac{\Delta F(\phi_P, \phi_S, \phi_N)}{\rho V k_B T} &= \frac{\phi_P \ln \phi_P}{N} + \phi_S \ln \phi_S + \phi_N \ln \phi_N \\ &+ \chi_{\text{PN}} \phi_P \phi_N + \chi_{\text{PS}} \phi_P \phi_S + \chi_{\text{NS}} \phi_N \phi_S \end{aligned}$$

$$\text{with } \phi_P + \phi_S + \phi_N = 1$$

parameter. In order to describe NIPS, polymer and nonsolvent are incompatible, $\chi_{\text{PN}} > 1/2$, whereas polymer and solvent as well as solvent and nonsolvent are miscible; i.e., $\chi_{\text{PS}} < 1/2$ and $\chi_{\text{NS}} < 2$. Note that this simple form ignores contact correlations

An alternative to the Flory–Huggins free energy can be obtained by employing a third-order virial expansion, i.e.,

$$\begin{aligned} \frac{\Delta F(\phi_P, \phi_N)}{\rho V k_B T} = & \frac{\phi_P \ln \phi_P}{N} + \phi_S \ln \phi_S + \phi_N \ln \phi_N \\ & + \sum_{\alpha\beta} \frac{v_{\alpha\beta}}{2} \phi_\alpha \phi_\beta + \sum_{\alpha\beta\gamma} \frac{w_{\alpha\beta\gamma}}{3} \phi_\alpha \phi_\beta \phi_\gamma \end{aligned} \quad (6)$$

where the Greek indices run over all components of the system—polymer, solvent, and nonsolvent. Again, in the case of incompressibility, $\phi_P + \phi_S + \phi_N = 1$, the system is characterized by only two independent densities. In this case, the free-energy function requires three second-order virial coefficients and four third-order coefficients.

Typically, polymer and solvent as well as solvent and nonsolvent are miscible at the thermodynamic states of interest. Macroscopic phase separation occurs between a polymer-rich and a polymer-lean phase. The latter phase predominantly consists of nonsolvent.

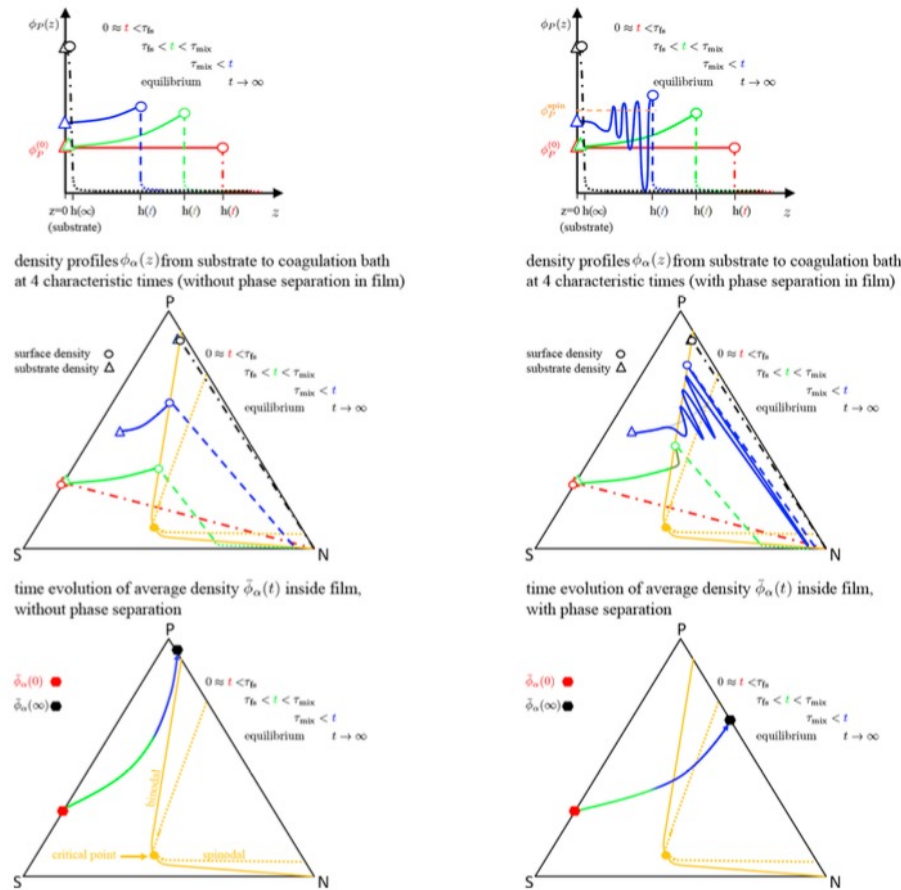


Figure 6. Schematic representation of NIPS. Top-row panels show the time evolution of the density profile, $\phi_p(z)$, across the system. The left column refers to a process where the film surface recedes upon solvent–nonsolvent exchange, but no phase separation occurs inside the film, whereas right panels illustrate a NIPS process with surface-directed spinodal decomposition. The red color corresponds to the initial contact between polymer film and coagulation bath, $0 \approx t < \tau_{fb}$, whereas the black color corresponds to the equilibrium, assuming that the polymer wets the substrate. The green color illustrates profiles in the mixing regime, $\tau_{fb} < t < \tau_{mix}$, while the blue color shows profiles for $t > \tau_{mix}$. Solid green and blue lines represent the profile inside the polymer film (process path), dashed lines represent the density variation across the film surface, and dotted lines illustrate the density profile in the coagulation bath. Triangles denote the densities at the substrate, whereas open circles mark the densities at the film surface. Lower panels depict NIPS on the phase triangle. Yellow solid lines indicate binodals, whereas yellow dashed lines represent spinodals. The yellow, solid circle denotes the critical point or plait point. Panels in the middle row depict the density profiles, $\phi_p(z)$, across the entire system. Different colors correspond to distinct times. The distance, z , is a parameter along the curves and varies from $z=0$ left to $z=L$ right, bottom. Bottom panels present the film-averaged densities, $\bar{\phi}_\alpha^{film}$, in the course of NIPS. Time, t , is a parameter along the curves and varies from $t=0$ (left, red hexagon, $\bar{\phi}_\alpha^{(0)}$), to the equilibrium (right, black hexagon). The color shading along the line indicates the mixing region (green) and later times (blue), $t > \tau_{mix}$.

Phase Triangle

Additionally, other properties that are relevant for the processing² in particular, the dynamic arrest of structure formation, such as vitrification or crystallization² are often indicated in the phase triangle.

A more quantitative description has to account for at least three additional aspects: (i) the spatial inhomogeneity of the system, (ii) the change of densities in the polymer film, as the solvent evaporates and the film thickness shrinks, as well as (iii) viscoelastic effects on the kinetics of phase separation.

Self-Assembly of Block Copolymer in Solutions and Melts

local microphase separation

spherical, worm-like cylindrical, or lamellar vesicles.

A way to form such self-assembled structures in solution is to slowly replace a good solvent for the different blocks by a very selective solvent, which is even a nonsolvent for one of the blocks. This can be achieved by dialysis of a block copolymer in a good solvent against a nonsolvent.

$\phi = \phi_A / \phi_P$ with ϕ_A

and $\phi = \phi_A + \phi_B$ denoting the density of polymer block A and ϕ_P the total polymer density

decoupling the fast microphase separation and the slow macrophase separation

self-assembly or microphase separation can be induced by temperature jumps, solvent evaporation, or solvent–nonsolvent exchange.

or a pure, symmetric diblock copolymer, the mean-field prediction of the order–disorder transition (ODT) is $\chi N = 10.5$

4. HOMOPOLYMER MEMBRANES 4.1. Phase-Inversion Membranes

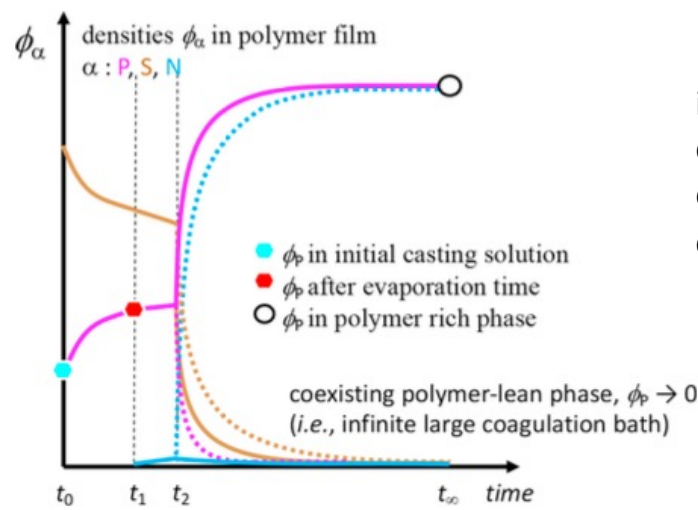
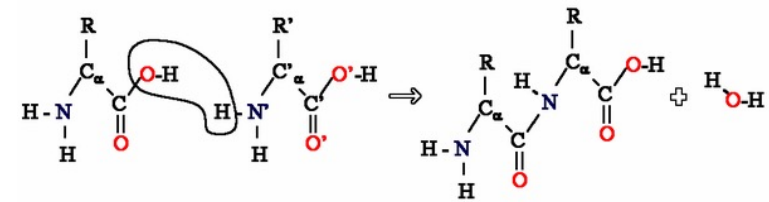


Figure 2. Sketch of the time evolution of the averaged densities, ϕ_α in an incompressible ternary system, composed of polymer P, solvent S, and nonsolvent N. The density of the polymer in the initially cast, solvent-swollen polymer film at t_0 is marked with a cyan hexagon. Until t_1 , the solvent evaporates, and the polymer density increases. At t_1 , the solution is immersed into an infinitely large nonsolvent (coagulant) bath, and phase separation into a polymer-rich and a polymer-lean phase occurs within the film after sufficient penetration of nonsolvent into the film at t_2 . If the polymer-rich phase was not kinetically trapped, phase separation would proceed until equilibrium, t_∞ .

integral-asymmetric membrane. It was a cellulose acetate membrane for reverse osmosis that displayed a good salt rejection combined with high flux

These membranes display a rather dense (and thus selective) surface layer on top of a more open, porous (and thus less resistive) substructure. The substructure can be spongy or display finger-like macrovoids.



Strathmann et al. presented experimental data on polyamide membranes, which were prepared by casting a polyamide solution film into a mixture of the solvent with water (nonsolvent).¹⁴⁰ In this way, the effective incompatibility between polymer and precipitant was varied, and the resulting membranes showed macrovoids when precipitated in pure water and a sponge structure in water mixed with 75% of solvent. The formation of macrovoids was explained by the fast precipitation of a polymer-rich skin layer at the film surface in case of a strongly incompatible precipitant (in this case, pure water) and the concomitant mechanical stresses in this top layer, which lead to defects at the surface. Across these defects, a fast penetration of precipitant into the polymer film occurs, resulting in finger- like macrovoids. In the case of a weak precipitant, in contrast, phase separation occurs slower; i.e., the phase-separation front slowly moves across the polymer film, resulting in a cocontinuous sponge structure.

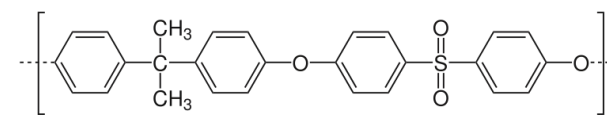
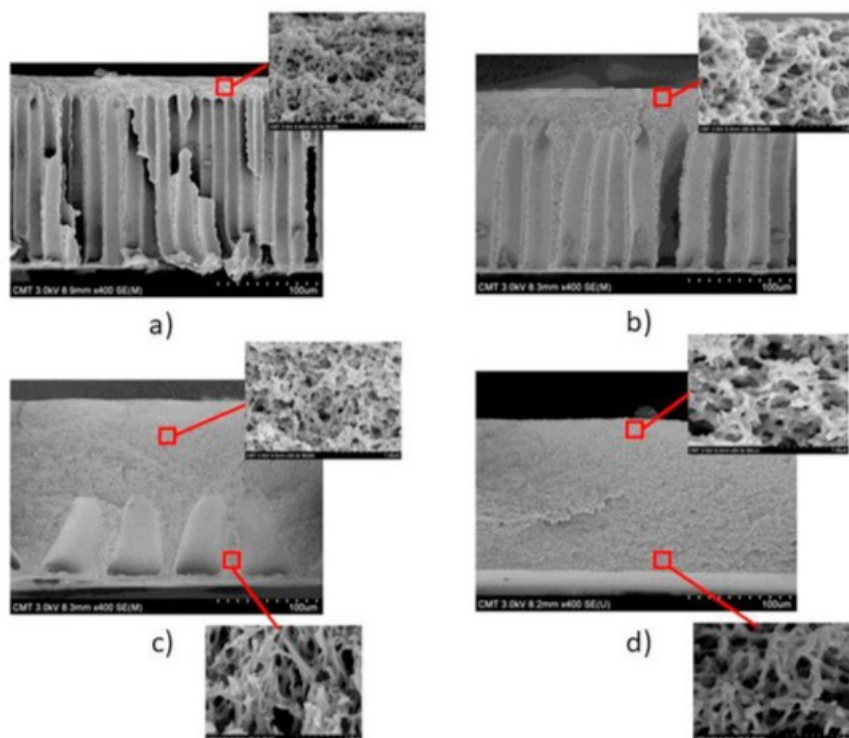


Figure 3. Cross-sections of membranes cast from solutions of polysulfone and precipitated in water. The polymer densities are 12% (a, c) and 18% (b, d). The solvent is 2-methylpyrrolidinone (a, c) and 2-methylpyrrolidinone with 0.5 wt % water (b, d). Comparison of (a) with (c) and (b) with (d) shows the influence of polymer density, while comparison of (a) with (b) and (c) with (d) illustrates the influence of the solvent quality, as the addition of water decreases the solubility of the polymer. Increasing the polymer density leads to an increase of the distance, L , between membrane surface and onset of macrovoids. Adapted with permission from ref 83. Copyright 2016 Elsevier.

This work also suggested two master curves: The observed distance, ΔL , between the membrane surface and the onset of macrovoids is related to polymer density or viscosity via

$$\frac{\Delta L^2}{D_e} \approx 0.2s \left(\frac{\phi}{\phi_e} \right)^{6.8} \quad \text{or} \quad \frac{\Delta L^2}{D_e} \approx 0.5s \frac{\eta}{\eta_e} \quad (10)$$

where D_e denotes the collective diffusivity of coagulant transport, and ϕ and ϕ_e stand for the polymer density in the casting solution and the entanglement density, respectively (see Figure 4). Moreover, the experimental data also correlate linearly with the viscosity, η , of the casting solution, when normalized by the viscosity, η_e , at which the influence of entanglements starts to become visible.

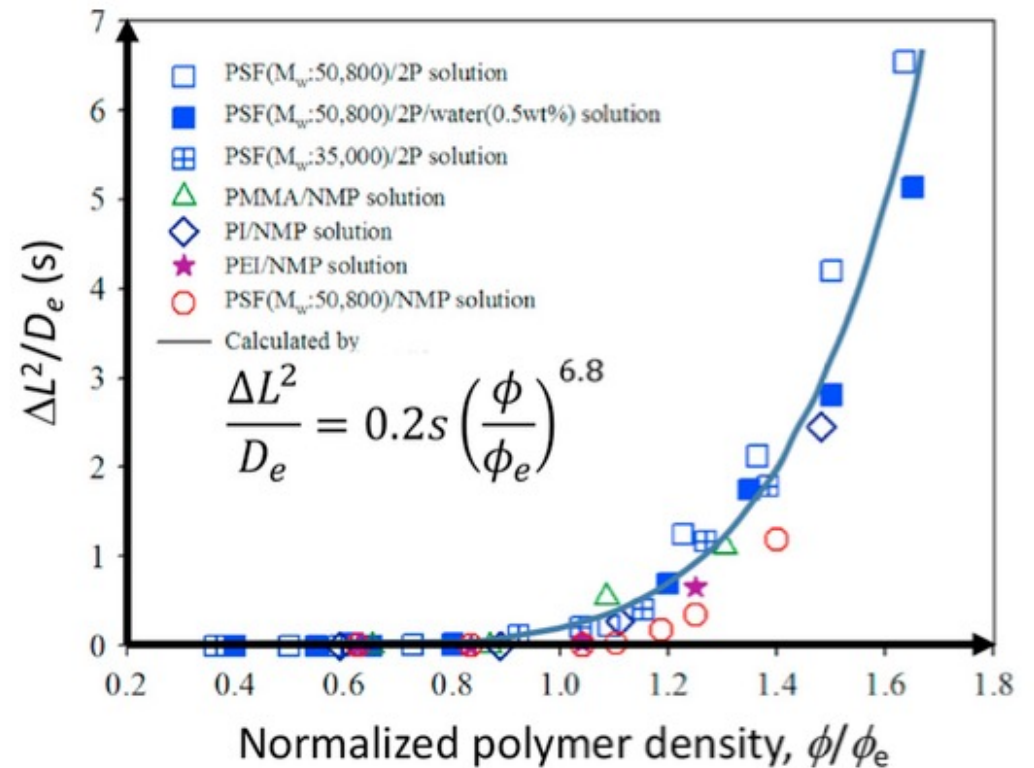


Figure 4. Master plot of the ratio between the squared distance, ΔL^2 , and the effective diffusivity, D_e , of the transport of coagulant, as a function of the polymer density, ϕ , in the casting solution normalized by the entanglement density, ϕ_e . Adapted with permission from ref 83. Copyright 2016 Elsevier.

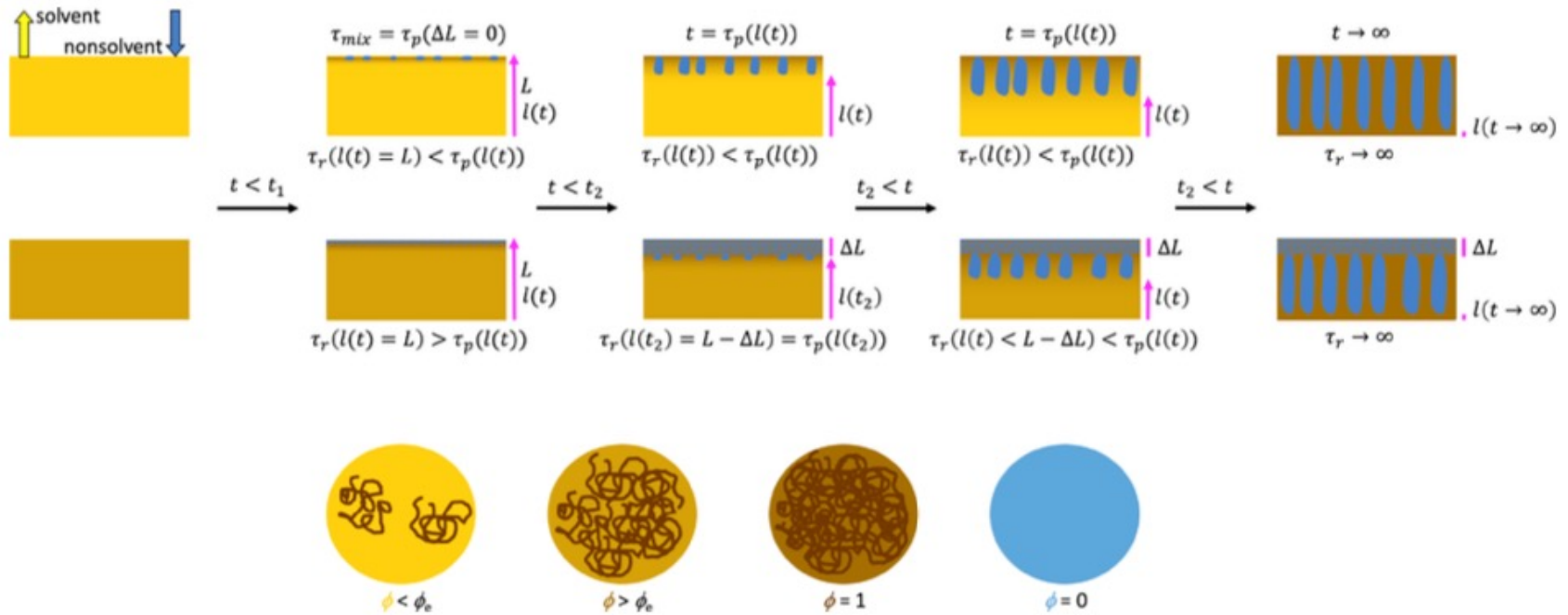


Figure 5. Illustration of the formation of macrovoids in the course of NIPS as a function of the polymer density, ϕ , in the polymer solution. When coagulating a polymer solution with a density below ϕ_e (top row), the chains with relaxation time, τ_p , are fully relaxed when phase separation starts at τ_p , and macrovoids form at the top of the film at a time, t_1 . If the polymer density is above ϕ_e (bottom row), however, phase separation starts before the chains are relaxed (disentangled). Thus, no macrovoids are initially formed, but a rather dense network structure is built up by spinodal decomposition. The distance, ΔL , between film surface and macrovoid formation increases with a higher polymer density and a with higher collective diffusivity of the coagulant, D_e . The scaling relation, eq 10, is applicable to a variety of polymer–solvent–nonsolvent systems. Inspired by a similar drawing in ref 83.

In addition to the bulk equilibrium thermodynamics, the different modeling approaches address

- (i) the role of spatial inhomogeneities such as the surface of the solvent- swollen polymer film in contact with a nonsolvent and
- (ii) the kinetics of phase separation, as well as
- (iii) the arrest of the structure formation by vitrification, crystallization, or gelation.

- Solvent evaporation (dry-casting) or evaporation-induced self-assembly (EISA)—a solvent evaporates from a solvent-swollen polymer or copolymer film into air (nonsolvent), and the film thickness, h , decreases in turn. As the solvent evaporates into the vapor phase, the local polymer density increases and potentially gives rise to the formation of a dense polymer layer (skin) at the film surface,^{143–147} resulting in a density gradient across the film. Additionally, because of the local change in composition, the polymer–solvent mixture may enter the miscibility gap and phase separate. In the case of a copolymer film, the copolymer may form micelles in the solvent-rich interior of the film or microphase separate in the regions of high polymer density.
- Nonsolvent-induced phase separation (NIPS)—a mixed film of polymer and solvent is brought into contact with a nonsolvent bath (coagulation bath). Solvent and nonsolvent are exchanged across the surface between polymer film and coagulation bath. Typically, the solvent leaves the film faster than the nonsolvent enters the film in turn. Thus, the film thickness, h , shrinks. The interplay between the thermodynamics of the ternary mixtures, the dynamic asymmetry of the constituents, and the kinetics of solvent and nonsolvent transport across the film surface may, however, give rise to a complex time evolution of the film thickness, $h(t)$.¹⁴⁸ As the nonsolvent enters the film via the film surface, the ternary mixture inside the film becomes unstable, and macrophase separation commences. If the polymer is a copolymer, additionally, microphase separation will occur inside the polymer-rich domains.

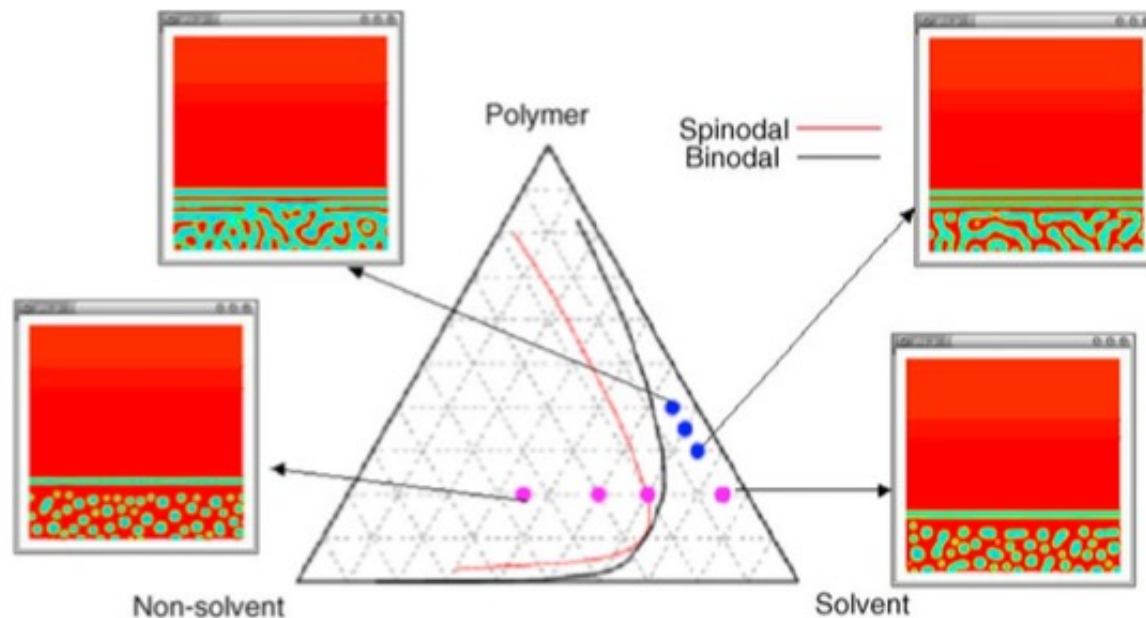


Figure 7. 2D Cahn–Hilliard study of the morphologies that are formed by bringing a polymer–solvent–nonsolvent mixture in contact with a nonsolvent-rich coagulation bath. The initial densities of the polymer film are indicated in the phase triangle by circles, and the two-dimensional plot depicts the polymer density. Red indicates vanishingly small polymer density, $\phi_p \approx 0$, while blue marks regions of high ϕ_p . Reprinted with permission from ref 274. Copyright 2006 Elsevier.

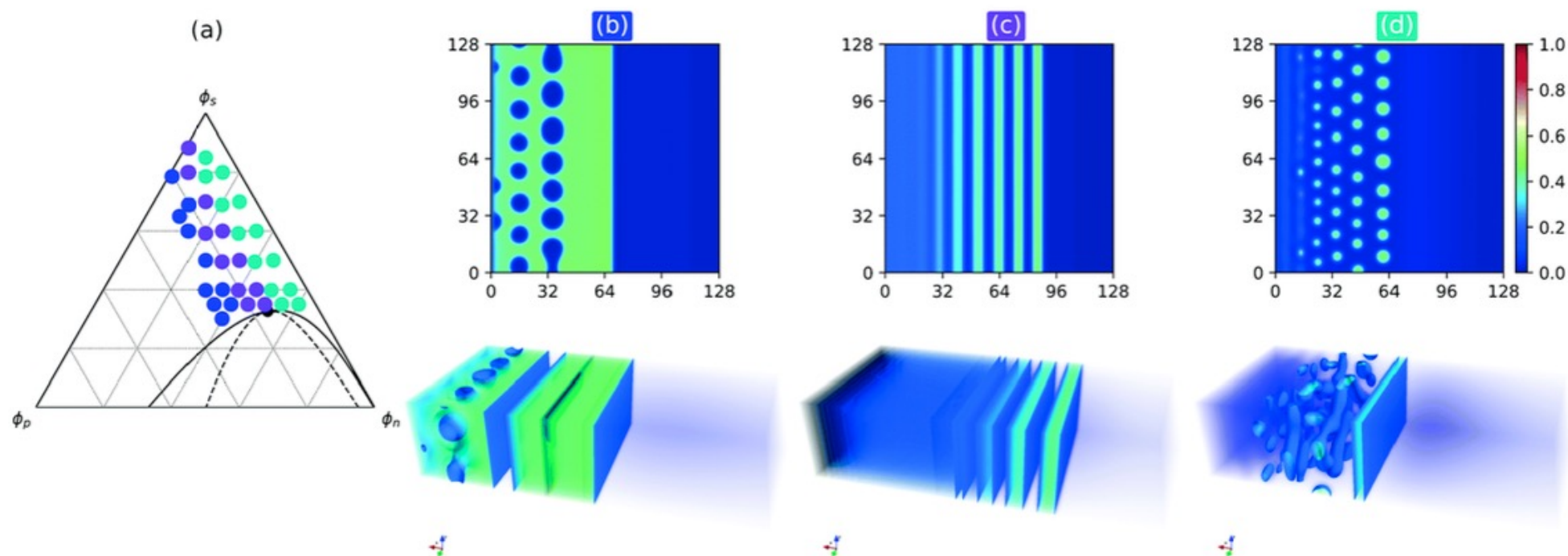


Figure 8. Surface-directed spinodal decomposition in two and three dimensions as a function of the initial polymer density, indicated in the phase triangle in panel a. Panels b–d present the polymer density at long times according to the color bar on the right. Upon decreasing the initial polymer density, $\phi_p^{(0)}$, from panel b to d, Tree and co-workers observed a transition from nonsolvent droplets, via alternating layers of nonsolvent and polymer, to polymer droplets. Republished with permission of the Royal Society of Chemistry (Great Britain), from ref 169. Permission conveyed through Copyright Clearance Center. Inc.

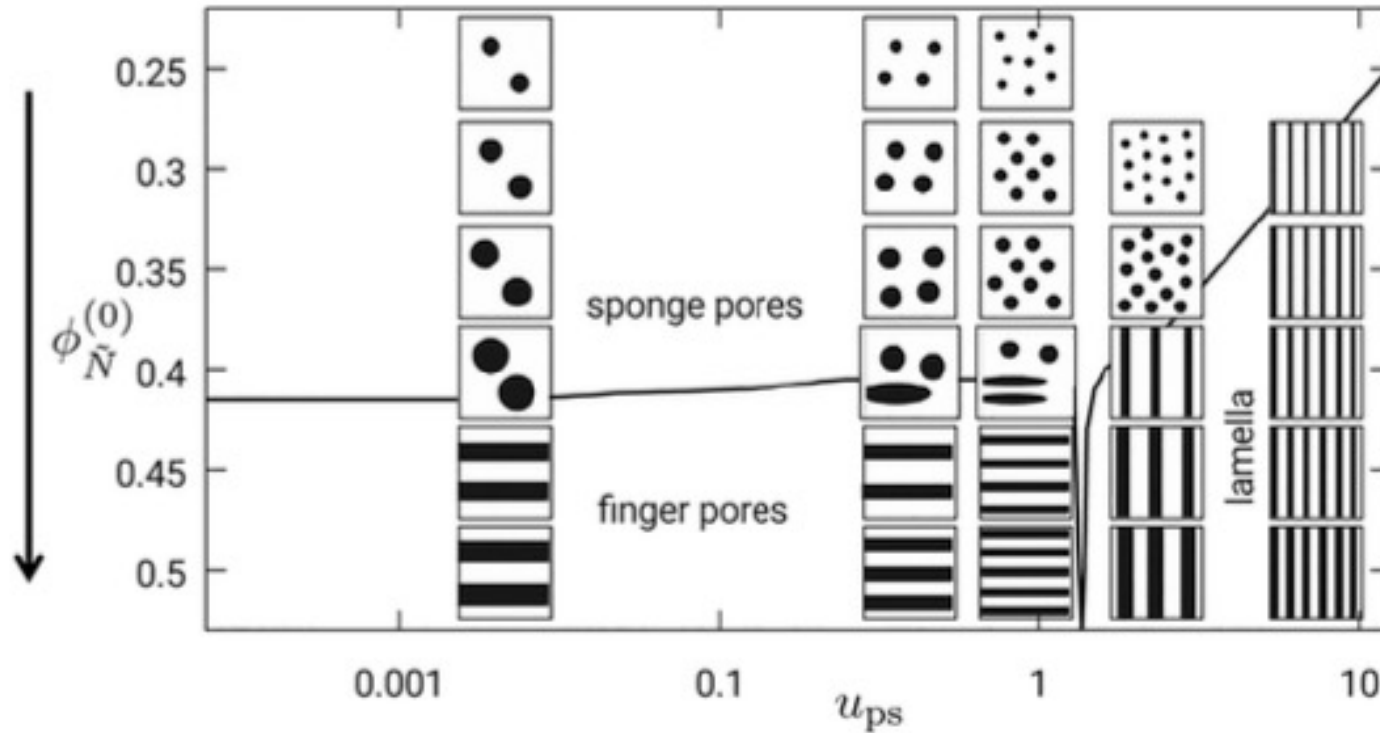


Figure 9. Diagram of morphologies as a function of the speed, u_{ps} , of the phase-separation front and the initial composition, $\phi_{\tilde{N}}^{(0)} = \phi_N^{(0)} + \phi_S^{(0)}/2$, of the homogeneous polymer film. Black domains stand for nonsolvent-rich pores, whereas white domains represent the polymer-rich phase. Adapted with permission from ref 182. Copyright 2018 Elsevier.

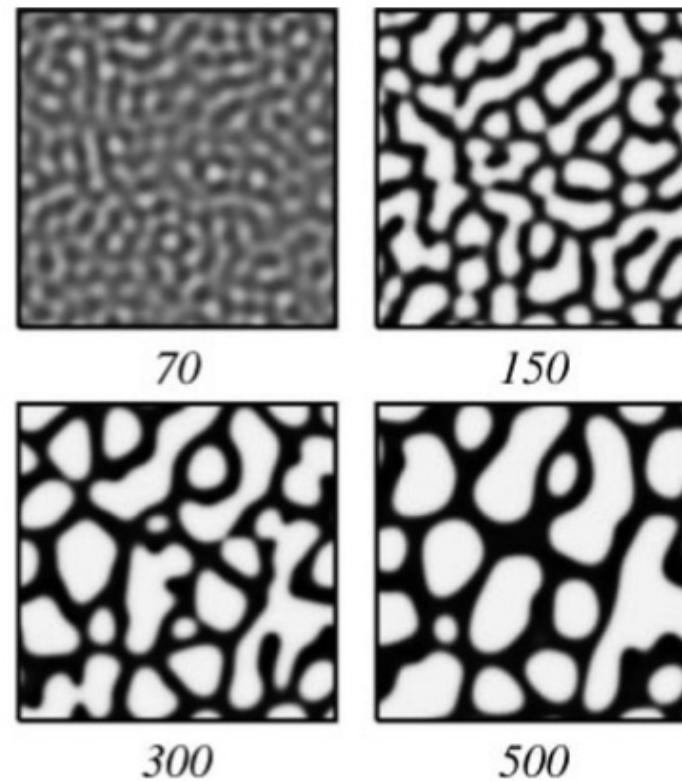


Figure 10. Gel-like morphologies in the course of viscoelastic phase separation in a binary polymer–solvent mixture. The average volume fraction of the polymer exceeds the polymer fraction at the critical point by a factor 2.5. Polymer domains are colored dark, whereas solvent-rich domains are depicted in white. The numbers denote the time after the quench into the miscibility gap. Reprinted figure with permission from ref 195. Copyright 1996 by the American Physical Society.

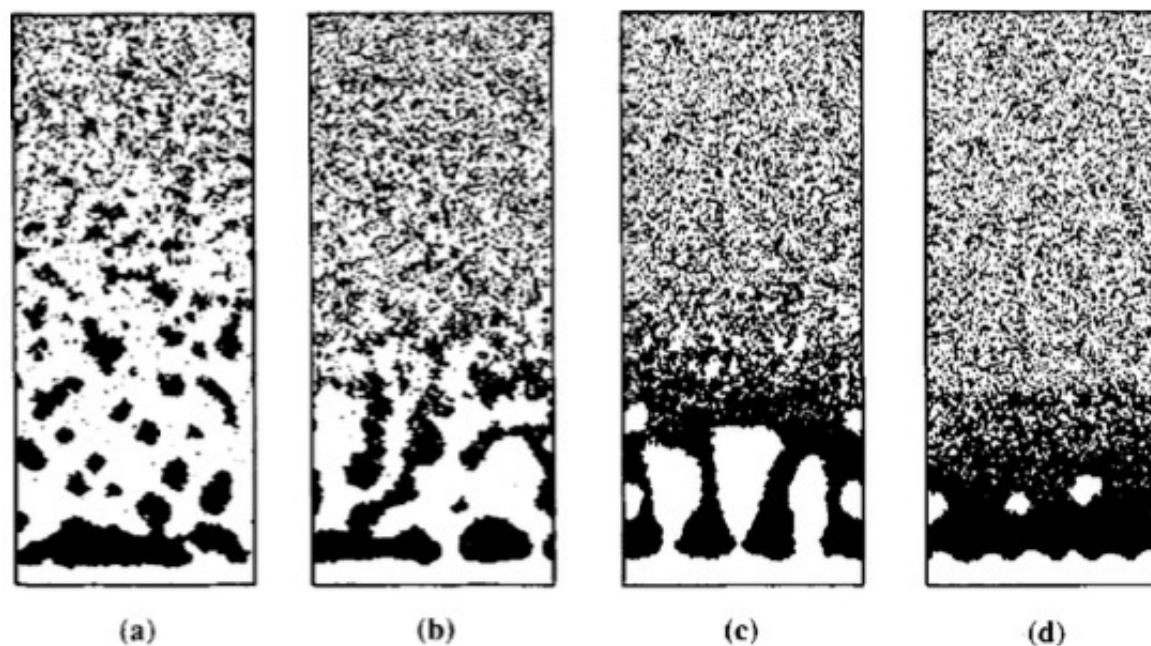


Figure 11. (a–d) Effect of solvent–nonsolvent incompatibility, χ_{SN} , on the morphology obtained by lattice simulation of NIPS. As χ_{SN} increases from left to right, the morphology changes from droplet-like polymer precipitates to finger-like pores to sponge-like structures. Reprinted from ref 289 with permission of John Wiley and Sons.

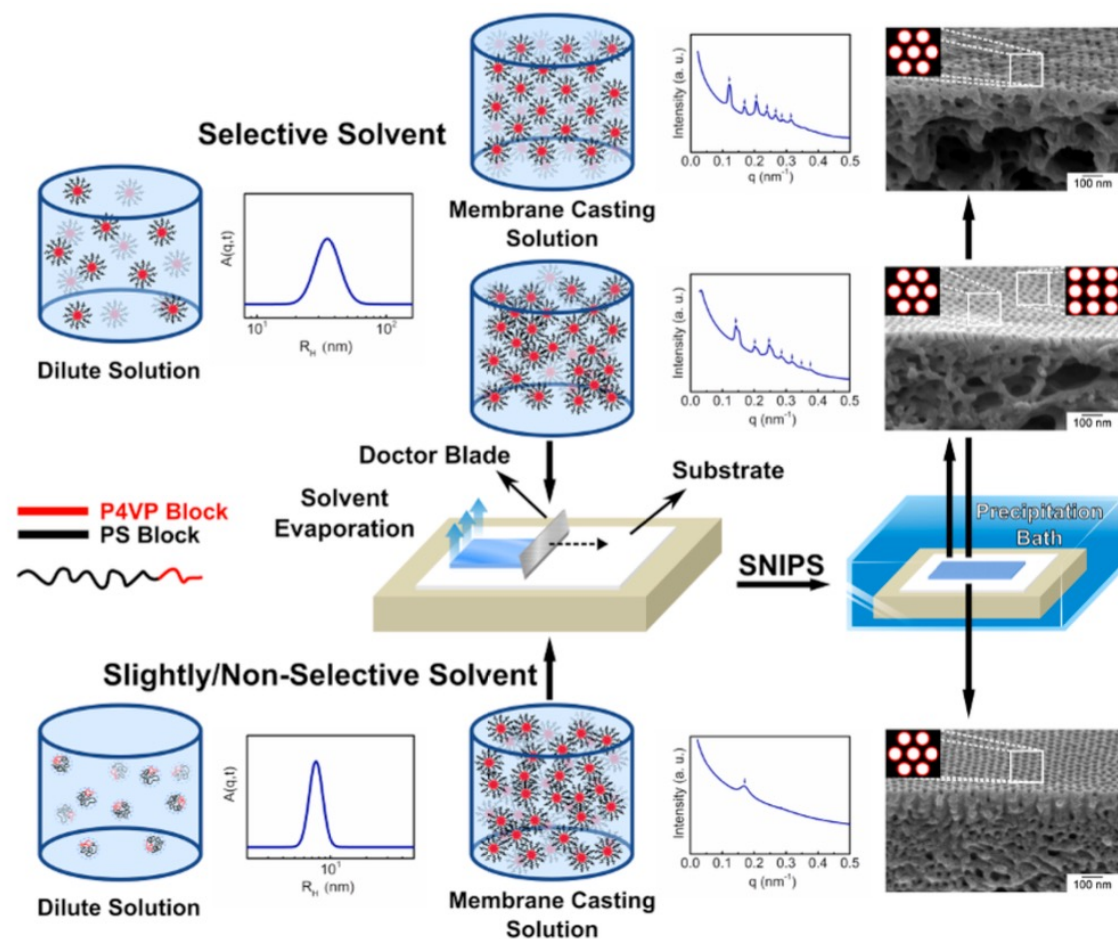


Figure 12. Schematics of the structure formation of a polystyrene-*block*-poly(4-vinylpyridine) block copolymer in a selective (top) or less/nonselective solvent (bottom). In dilute solution, the block copolymer dissolves as micelles (top) or unimers (bottom), as indicated by dynamic light scattering measurements, measuring the hydrodynamic radius. At higher density, these micelles order into a superlattice in the case of a selective solvent (top) or weakly ordered micelles (bottom), as shown by SAXS measurements. After precipitation, integral-asymmetric membranes are obtained with an isoporous surface but different cross-sectional structures. Reprinted with permission from ref 84. Copyright 2017 American Chemical Society.

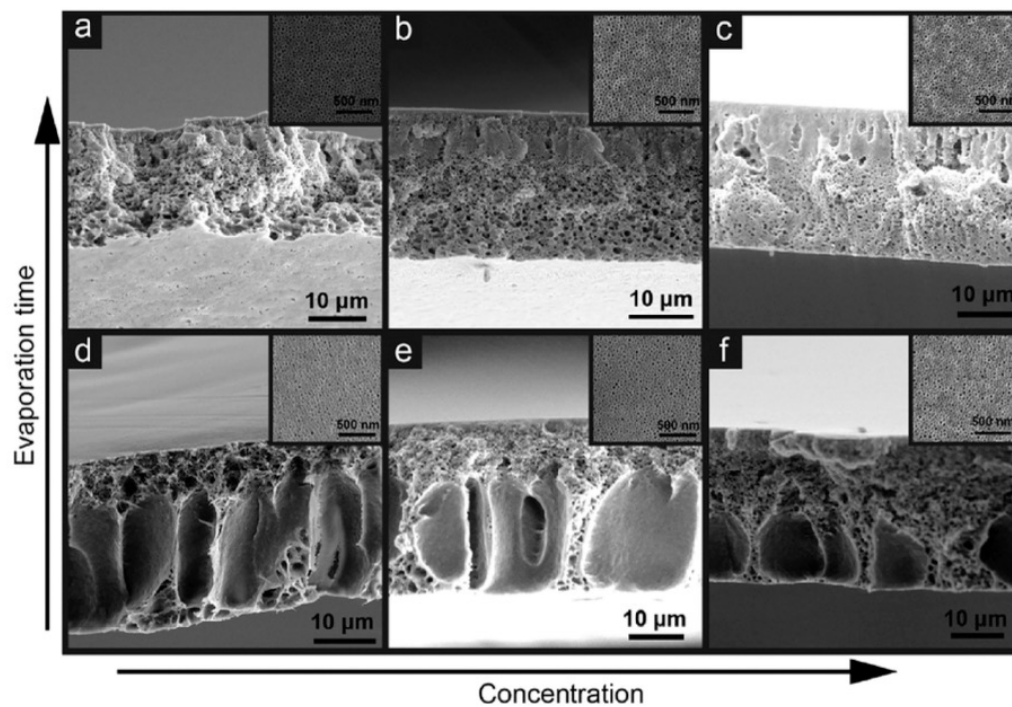


Figure 13. SEM images of cross-sections and top surfaces (inset images) of polyisoprene-*block*-polystyrene-*block*-poly(4-vinylpyridine) membranes cast from a solution in DOX/THF (5/5). (a, d) 9 wt %, (b, e) 10 wt %, and (c, f) 11 wt %. Evaporation times of (a–c) are 60 s and of (d–f) are 45 s, before immersion into water. Short evaporation times lead to macrovoid formation, and higher densities hinder the formation of macrovoids. As the block copolymer has a molecular weight above the entanglement molecular weight of the matrix-forming blocks (polyisoprene-*block*-polystyrene), macrovoid formation is hindered above a certain density, as discussed before for homopolymers (compare with Figure 3). The longer evaporation time gives rise to an increase of polymer density, leading also to the suppression of macrovoids. Reprinted with permission from ref 309. Copyright 2016 Elsevier.

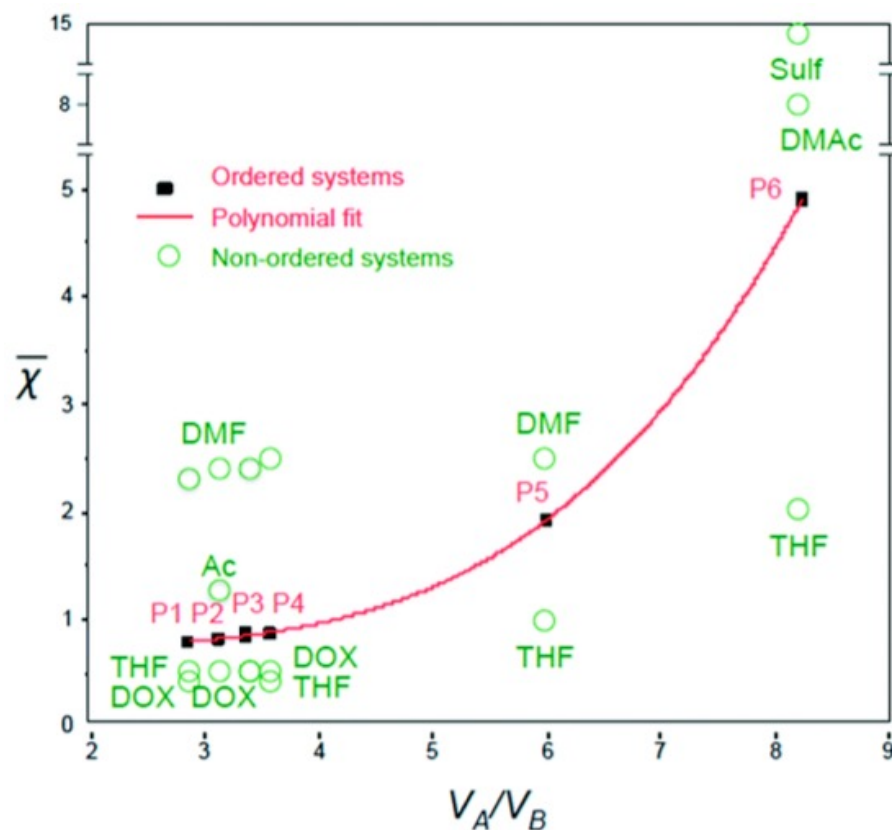


Figure 14. Trend line (following a third-order polynomial) showing a normalized segmental interaction contrast, $\bar{\chi} \equiv \frac{\chi_{AS}N_A - \chi_{BS}N_B}{\chi_{AB}N}$, between the A and B blocks of a diblock copolymer and the solvent as a function of the ratio of the volumes of the less soluble block A to the more soluble block B. Republished with permission of the Royal Society of Chemistry (Great Britain), from ref 310. Permission conveyed through Copyright Clearance Center, Inc.

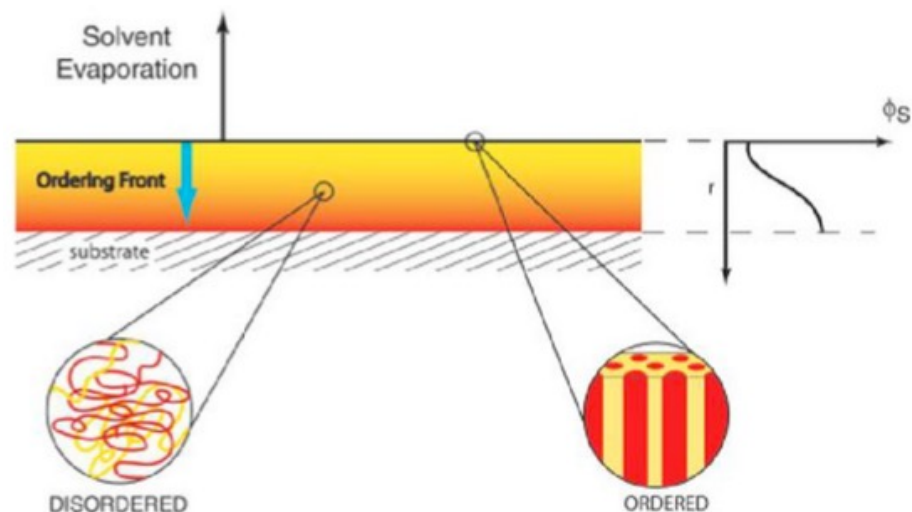


Figure 15. Schematic diagram of solvent evaporation from a thin block copolymer film. At the surface, the solvent density is lowest, and the copolymer undergoes microphase separation. A gradient in the solvent density, as a function of depth, r , is established normal to the film surface with the solvent density increasing with depth. This increase in solvent density leaves the copolymer disordered in the interior of the film. As the solvent evaporates, an ordering front propagates through the film, akin to zone refinement, producing a highly ordered and oriented array of cylindrical microdomains in the film. Reprinted from ref 92 with permission by John Wiley and Sons.

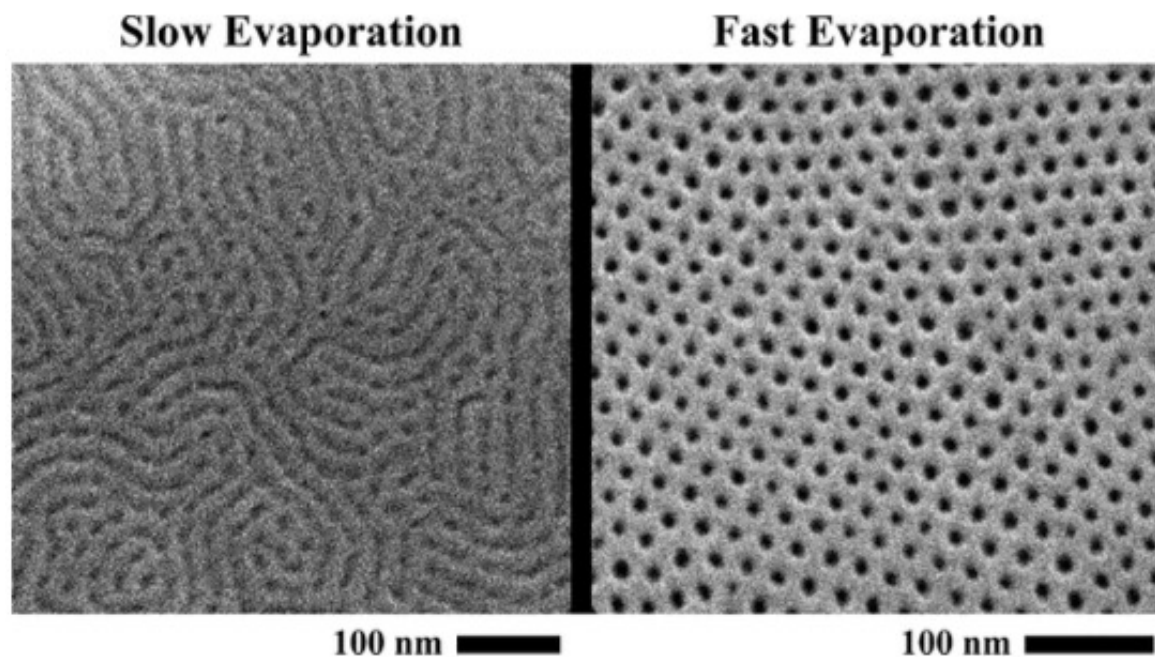


Figure 16. SEM micrographs of the top surface of polystyrene-*block*-poly(lactide) thin films obtained by casting an 8 wt % solution on a porous support and letting it dry slowly (2 h), leading to parallel alignment of the PLA cylinders, or fast (5 min), resulting in perpendicularly aligned cylinders. The final membrane thickness of the block copolymer layer is 4 μm . Reprinted with permission from ref 88. Copyright 2010 American Chemical Society.

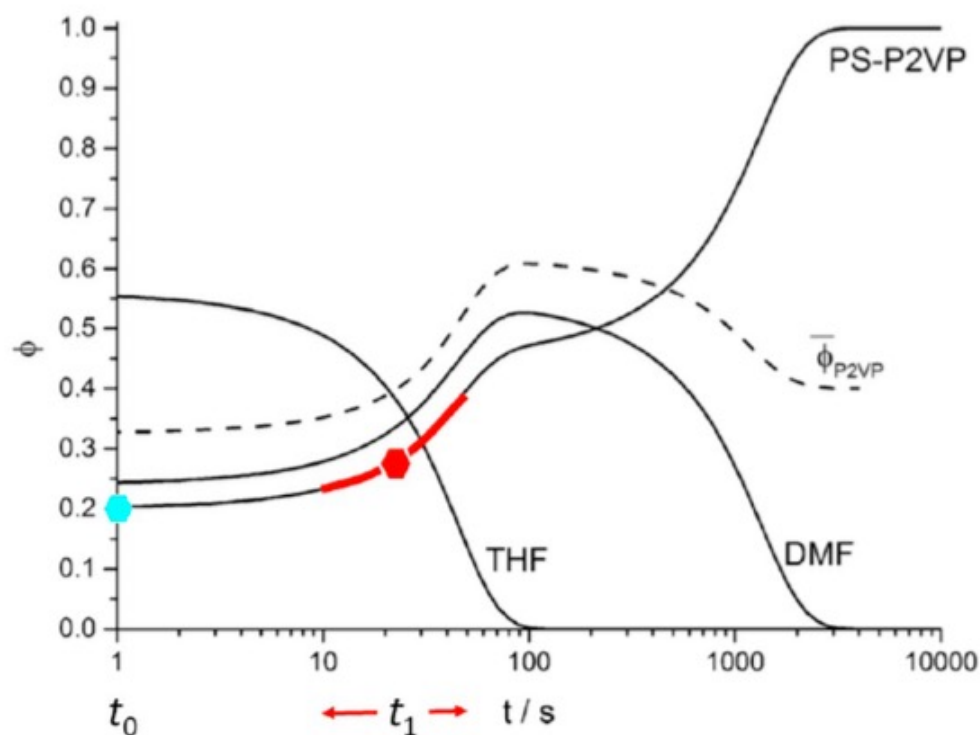


Figure 17. Time evolution of a polystyrene-*block*-poly(2-vinylpyridine) diblock copolymer and solvent densities during the evaporation. The cyan hexagon indicates the block copolymer density in the initial casting solution, and the red hexagon indicates the composition at the time, t_1 , when the cast film should be brought in contact with the coagulant to achieve the desired membrane structure with an isoporous surface. The red line and arrow indicate the suitable range of block copolymer density and evaporation time. Adapted with permission from ref 265. Copyright 2014 American Chemical Society.

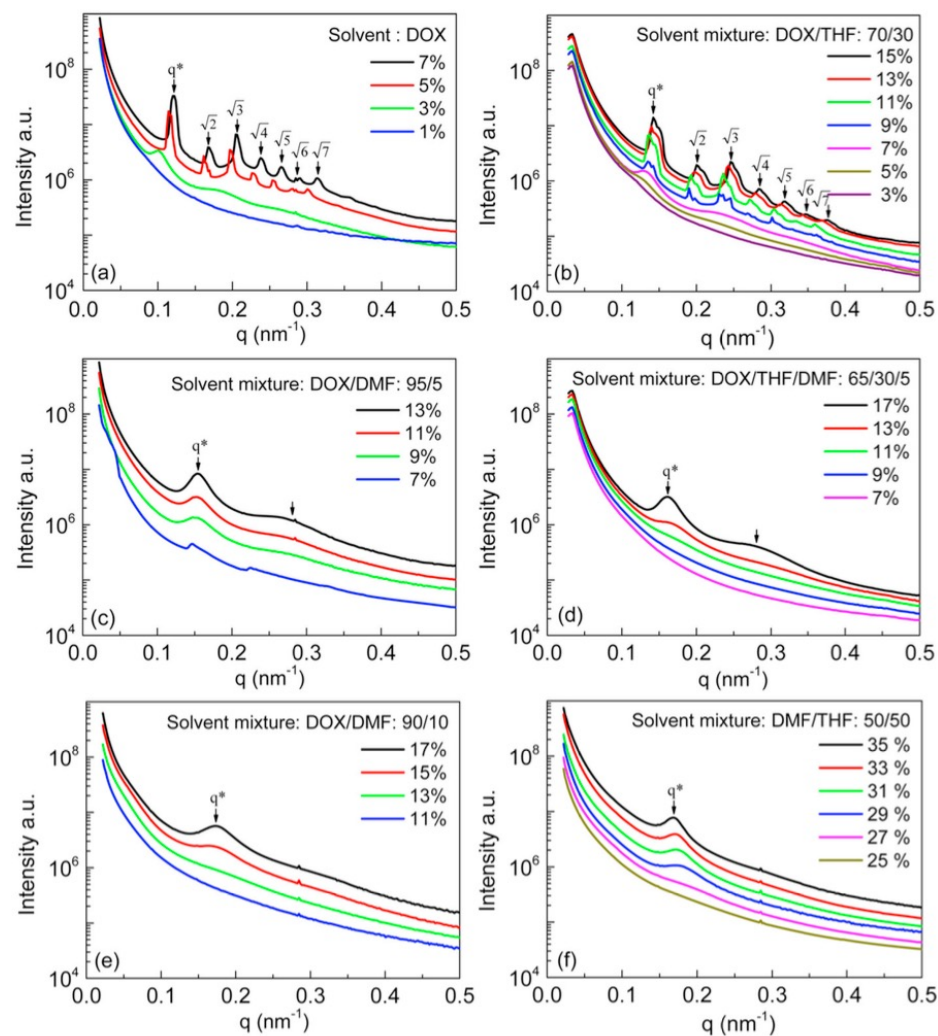


Figure 18. SAXS patterns of polystyrene-*block*-poly(4-vinylpyridine) solutions at varying concentrations in (a) DOX, (b) DOX/THF: 70/30 (w/w), (c) DOX/DMF: 95/5 (w/w), (d) DOX/THF/DMF: 65/30/5 (w/w/w), (e) DOX/DMF: 90/10 (w/w), and (f) DMF/THF: 50/50 (w/w). The intensity curves are vertically shifted to avoid overlapping. The arrows correspond to the peak positions (q/q^*)² = 1, 2, 3, 4, 5, 6, and 7 present a BCC lattice. Reprinted with permission from ref 84. Copyright 2017 American Chemical Society.

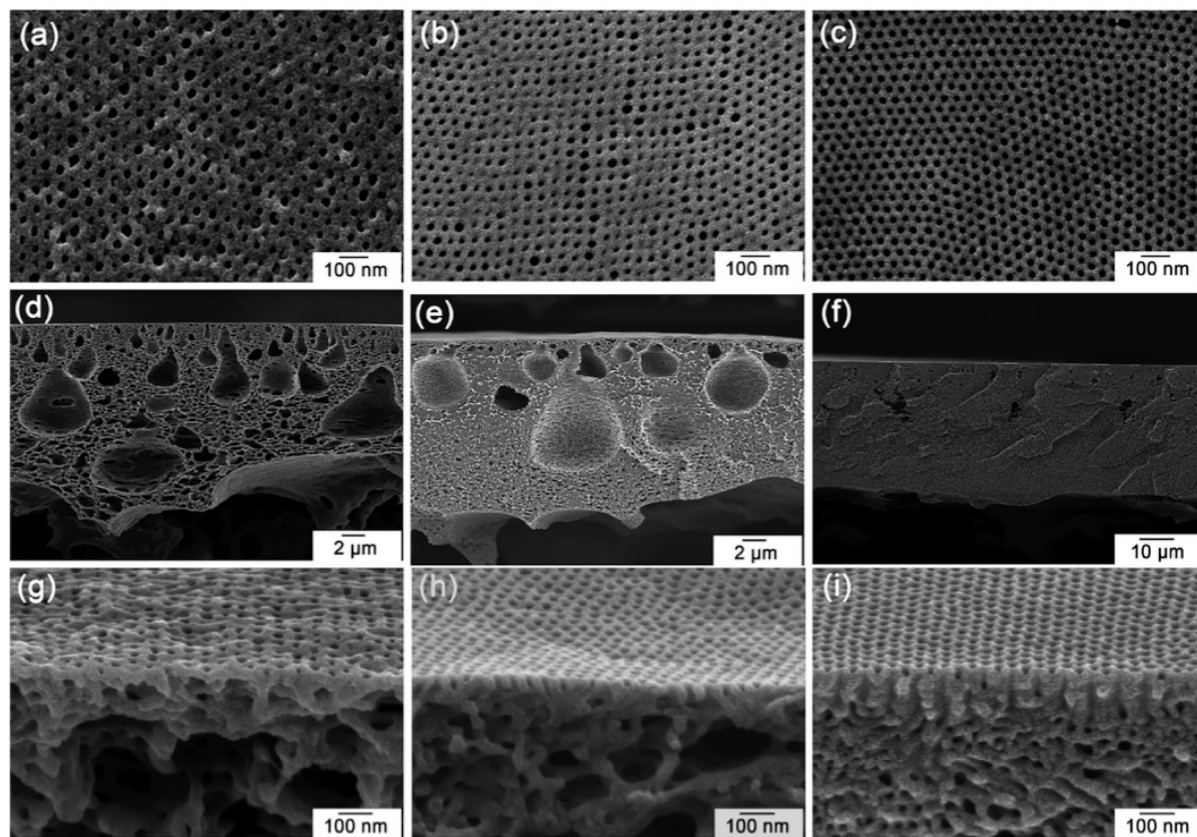


Figure 19. SEM micrographs of the top surface (top row), cross-section (middle row), and cross-section close to the top surface (bottom row) of polystyrene-*block*-poly(4-vinylpyridine) membranes cast from different solutions at different evaporation times; (a, d, g) 9 wt % in DOX 40 s, (b, e, h) 15 wt % in DOX/THF: 70/30 (w/w) 10 s, and (c, f, i) 33 wt % in DMF/THF: 50/50 (w/w) 5 s. Reprinted with permission from ref 84. Copyright 2017 American Chemical Society.

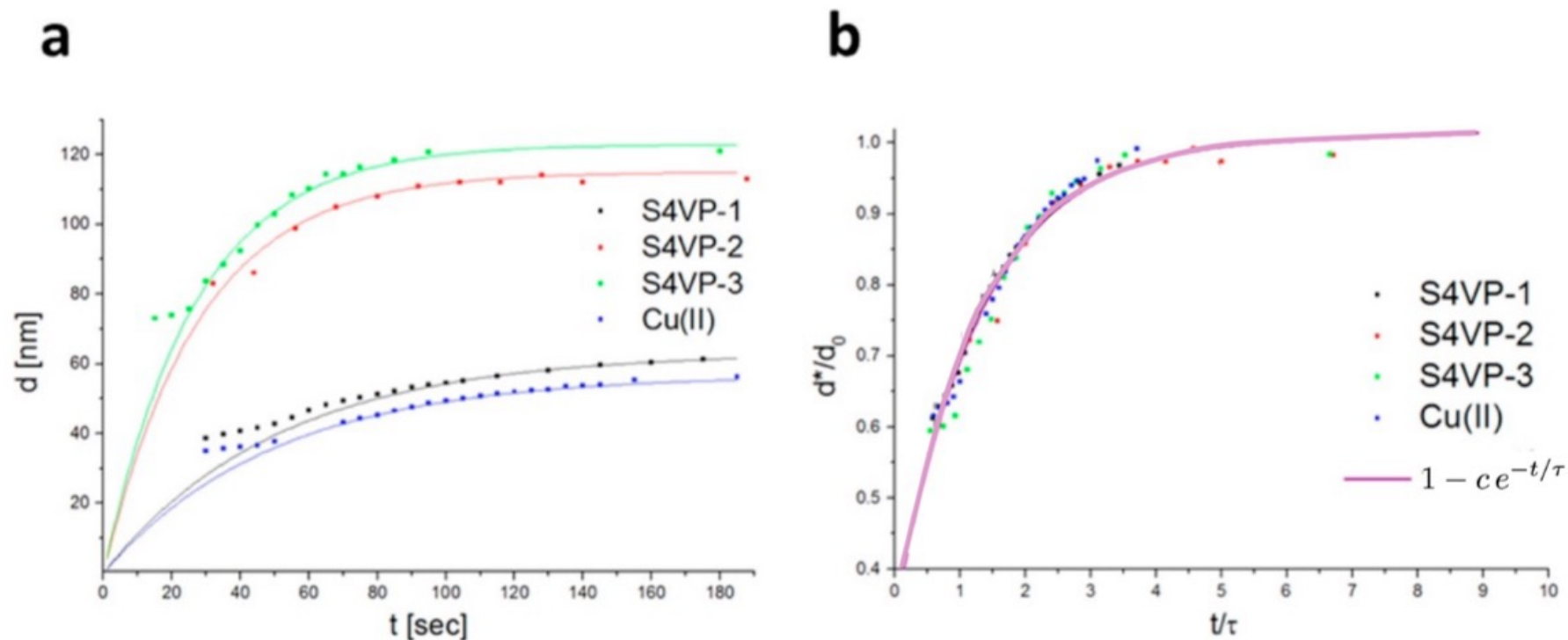


Figure 20. (a) Characteristic length scales during evaporation as a function of time for the three polystyrene-*block*-poly(4-vinylpyridine) block copolymers S4VP-1, S4VP-2, S4VP-3, and a block copolymer/salt-system S4VP-1/Cu(II). Solid lines indicate fits to a simple exponential saturation curve, (b) the same data, rescaled to a reduced time and a reduced length scale showing the common behavior of all investigated block copolymer systems. Adapted with permission from ref 321. Copyright 2015 American Chemical Society.

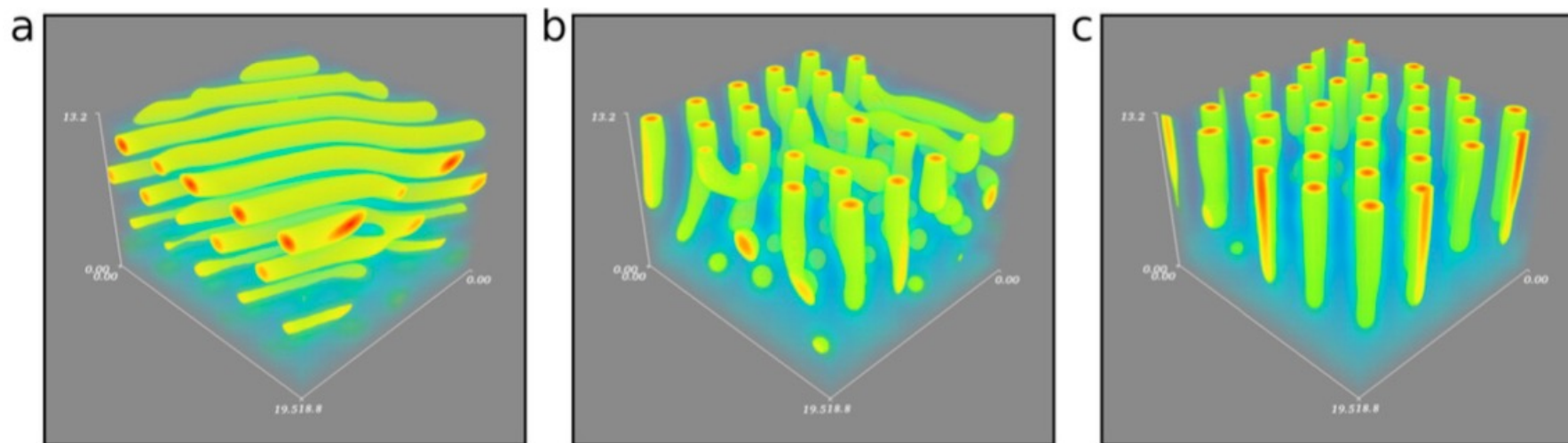


Figure 21. (a–c) D-SCFT of solvent evaporation from a solvent-swollen asymmetric diblock copolymer film, $f = 0.3$. The initial solvent fraction is $\phi_s^{(0)} = 0.9$. The solvent quality for the majority block B increases from left to right, $\Delta\chi_s N = \chi_{AS} N - \chi_{BS} N = -7, 0$, and 7 , and results in a transition from parallel to perpendicular cylinders. Reprinted from ref 262. Copyright 2014 American Chemical Society.

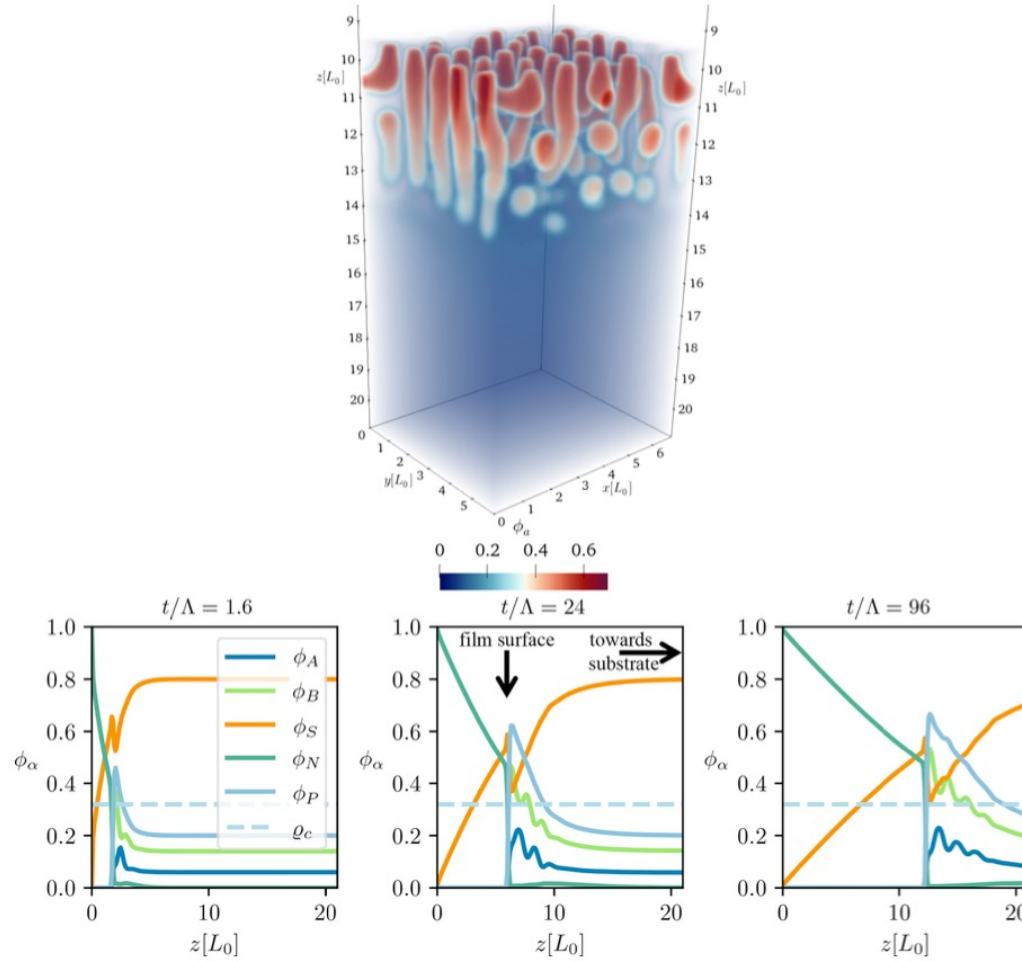


Figure 22. Evaporation from a solvent-swollen diblock copolymer film obtained by model B dynamics of a continuum model.¹³⁸ The top panel depicts the density, $\phi_A(\mathbf{r})$ of the minority component, $f = 0.3$, of the diblock copolymer, according to the color bar at the bottom. $N = 16$, $N_S = N_N = 1$. Initially, the composition of the film was $\phi_P(z) = 0.2$, $\phi_S(z) = 0.8$, and $\phi_N = 0$, and small fluctuations were added. $\chi_{AB}N = 46$, and the air is selective for the majority component, $\chi_{AN}N = 160 > \chi_{BN}N = 80$. The bottom panels present the transversally averaged density profiles of the components at three different times. Length scales are measured in units of the cylinder spacing, L_0 . From ref 323.

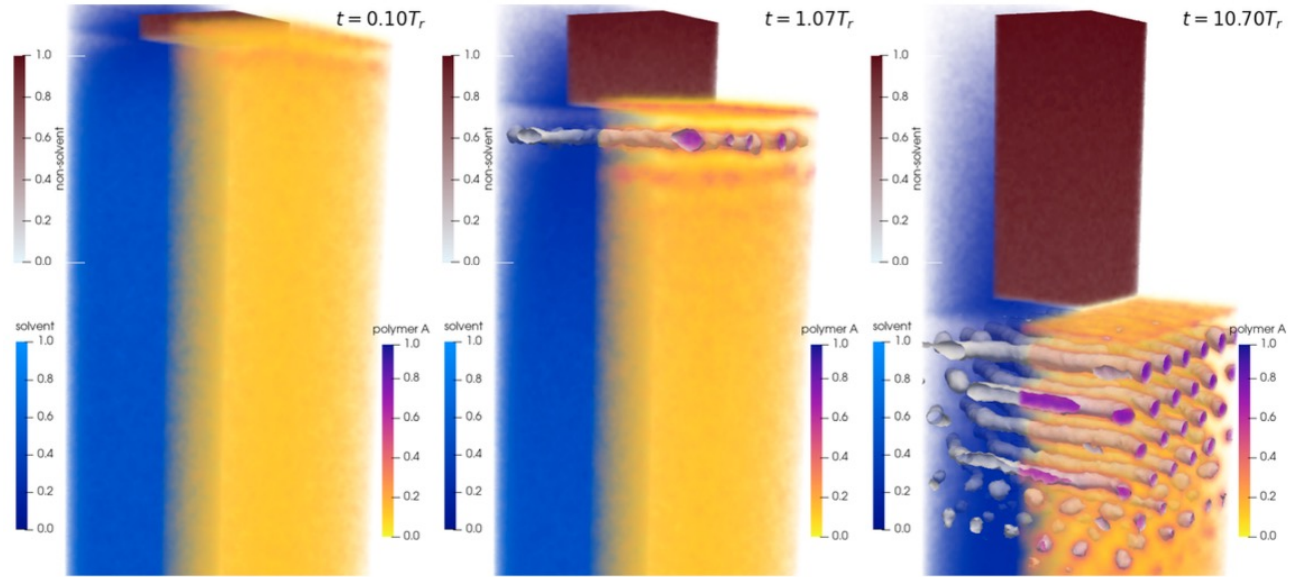


Figure 23. Particle simulation of evaporation from a solvent-swollen copolymer film with SOMA.²⁵⁵ The system geometry is $10 \times 10 \times 40 R_c^3$. The left half of the simulation box shows the density of solvent, ϕ_S (blue) and nonsolvent, ϕ_N (brown). On the right, the density, ϕ_A , of the minority block of the asymmetric diblock, $f = 1/4$, is presented, highlighted with contour surface (full box) after microphase separation sets in. The panels present different snapshots; time increases from left to right. $\chi_{AB}N = 30$, $\chi_{AS}N = \chi_{BS}N = 0$, and $\chi_{AN}N = \chi_{BN}N = 64$, and $\chi_{SN} = 0$.

